Analytical Methods for Quantification of Light-Matter Interactions in Subwavelength Metal Nanostructures

by

Amrita Pati

B. Tech., Odisha University of Technology and Research, 2018

A thesis submitted in partial fulfillment of the requirements

for the degree of

MASTER OF APPLIED SCIENCE

in the

Department of Electrical and Computer Engineering

We acknowledge with respect the lək̓ʷəŋən peoples on whose traditional territory the university stands and the Songhees, Esquimalt and W̱SÁNEĆ peoples whose historical relationships with the land continue to this day.

Supervisory Committee

Analytical Methods for Quantification of Light-Matter Interactions in Subwavelength Metal Nanostructures

by

Amrita PATI

B. Tech., Odisha University of Technology and Research, 2018

Supervisory Committee

Dr. Reuven GORDON, **Supervisor**

Department of Electrical and Computer Engineering

Dr. Poman P. M. SO, **Committee Member**

Department of Electrical and Computer Engineering

Abstract

The thesis presents analytical techniques to determine mode propagation characteristics in subwavelength metallic slits and plasmonic slot waveguides. These metal-insulator-metal geometries have been successfully applied in wide-ranging applications having demonstrated unprecedented performance in high-speed electrooptic modulation and rf-to-fiber conversion. But most of the theoretical studies focused on them rely on numerical methods, which are resource-intensive and lack physical insights. The proposed models address these challenges by calculating the properties in terms of other physical parameters, thereby providing the desired intuition.

In both frameworks, analytic expressions for reflection coefficients at the structure's interface with surrounding dielectric media were derived. This was achieved by employing the single-mode matching to continuum technique under the perfect electric conductor approximation. Dielectric loading was introduced to account for the finite permittivity of real metals. In the case of the slit, the reflection coefficient values for different source and waveguide parameters were used in the Fabry-Pérot transmission model to calculate field enhancement, power, scattering, and absorption cross-sections. It was shown that the power in the slit was maximum if the scattering and absorption cross-sections matched at the resonance condition of a given slit configuration, a manifestation of the maximum power transfer theorem. This also implied that the power in the slit, unlike the field enhancement, was maximum for slit widths typically larger than the narrowest slit under consideration and can be treated as a key parameter to balance mode confinement and propagation lengths.

The analysis of the plasmonic slot waveguides was based on a geometric optics approach. The reflection phase values obtained in the first stage were used in the

waveguide transverse resonance condition to obtain values of propagation angles that allowed the existence of modes in the structure. These angular solutions were then used to compute modal properties such as mode effective index and propagation lengths. Both the analytical frameworks were significantly faster (at least two orders of magnitude) than numerical simulations and demonstrated close agreement to within 3% of the numerical simulation results. These analytical models present an efficient way to design and optimize subwavelength slit and plasmonic slot waveguides for different applications and may be extended to analyze other plasmonic geometries for wider implementation.

Table of Contents

List of Figures

List of Symbols

Symbol	Name	Unit
α	polarizability	$\mathrm{C\,m^2\,V^{-1}}$
β / k_z	propagation constant	$\mathrm{rad\,m^{-1}}$
ϵ_0	vacuum permittivity	$\mathrm{F\,m^{-1}}$
ϵ_m	relative permittivity of metal	(1)
ϵ_d	relative permittivity of dielectric	(1)
θ	propagation angle	rad
λ	wavelength	m
μ_0	vacuum permeability	$\mathrm{H\,m^{-1}}$
σ_s	scattering cross-section	m
σ_a	absorption cross-section	m
ω	angular frequency	$\mathrm{rad\,s^{-1}}$
k	wavenumber	$\mathrm{m^{-1}}$
n	refractive index	(1)
P	power	$\mathrm{W\ (J\,s^{-1})}$
t	time	s
T	transmission	(1)
r	reflection coefficient	(1)
$\mathbf{E}$	electric field vector	$\mathrm{V\,m^{-1}}$
$\mathbf{H}$	magnetic field strength	$\mathrm{A\,m^{-1}}$
$\mathbf{p}$	dipole moment vector	$\mathrm{C\,m}$
$\mathbf{r}$	position vector	m
∇	vector differential operator	–

Glossary

AR	**A**spect **R**atio
ATR	**A**ttenuated **T**otal Internal **R**eflection
CMOS	**C**omplementary **M**etal-**O**xide **S**emiconductor
DNA	**D**eoxyribo**n**ucleic **A**cid
DNH	**D**ouble **N**ano**h**ole
EM	**E**lectro**m**agnetic
ENZ	**E**psilon-**N**ear-**Z**ero
FDTD	**F**inite-**D**ifference **T**ime-**D**omain
IMI	**I**nsulator-**M**etal-**I**nsulator
IR	**I**nfra**r**ed
LDOS	**L**ocal **D**ensity of **O**ptical **S**tates
LED	**L**ight **E**mitting **D**iode
LRSPP	**L**ong-**R**ange **S**urface **P**lasmon **P**olariton
LSPR	**L**ocalized **S**urface **P**lasmon **R**esonance
LSP	**L**ocalized **S**urface **P**lasmon
MIM	**M**etal-**I**nsulator-**M**etal
NIR	**N**ear-**I**nfra**r**ed
PEC	**P**erfect **E**lectric **C**onductor
PML	**P**erfectly **M**atched **L**ayer
PSPP	**P**ropagating **S**urface **P**lasmon **P**olariton
RIU	**R**efractive **I**ndex **U**nit
SIBA	**S**elf-**I**nduced **B**ack **A**ction
SMM	**S**ingle-**M**ode **M**acthing
SP	**S**urface **P**lasmon
SPP	**S**urface **P**lasmon **P**olariton
SPR	**S**urface **P**lasmon **R**esonance
SRSPP	**S**hort-**R**ange **S**urface **P**lasmon **P**olariton
TE	**T**ransverse **E**lectric
TEM	**T**ransverse **E**lectro**m**agnetic
TFSF	**T**otal-**F**ield **S**cattered-**F**ield
TM	**T**ransverse **M**agnetic
TMM	**T**ransfer **M**atrix **M**ethod

Acknowledgements

I would first like to thank my supervisor, **Dr. Reuven Gordon**, for his support, patience, guidance, and insights throughout the program. I would also like to thank him for his constant encouragement to explore new ideas and opportunities that would have otherwise remained untapped.

I am extremely grateful to my current and former colleagues at the Nanoplasmonic Research Lab for their continued support, advice, and kindness that I will cherish for the rest of my life. **Dr. Ghazal Hajisalem**, **Dr. Demelza Wright**, **Dr. Mirali Shariatdoust**, **Dr. Veerpal Kaur**, **Elham Babaei**, **Samuel Mathew**, **Behnam Khosravi**, **Elham Hosseini**, **Parinaz Moazzezi**, **Hao Zhang**, and **Matthew Peters**.

I am thankful to the NSERC CREATE in Quantum Computing program for providing me with several opportunities to learn and work with diverse groups of people in quantum computing.

I would like to thank my new family in Canada for their love and encouragement, Valerie Tipler and Snoopy. Finally, I would like to thank my family back home, for their meaningful role in my love for scientific thinking, for their unwavering faith in me and my choices, and for their many sacrifices. None of this would have been possible without them.

"We are all in the depths of a cave, chained by our ignorance, by our prejudices, and our weak senses reveal to us only shadows. If we try to see further, we are confused; we are unaccustomed. But we try. This is Science."

- Carlo Rovelli

To all the researchers who try, despite being constantly faced with their own ignorance.

Chapter 1

Introduction

The thesis presents analytical methods for understanding the propagation of electromagnetic waves in nano-scale plasmonic structures including slits in metals and plasmonic slot waveguides. These theoretical frameworks serve as tools to rapidly analyze, design and optimize plasmonic geometries for different applications. They provide physical insights into how light interacts with these structures as the desired properties are determined in terms of other physical parameters. Analytical methods such as these will be potentially vital in scaling up the implementation of plasmonic structures as they offer simpler means to address the inherent challenges linked to plasmon-based devices, which will be discussed throughout the dissertation.

1.1 Motivation

The interactions of light with the collective electron oscillations in metals have attracted the interest of researchers from both fundamental and applied sciences. These interactions result in the spatial localization of electromagnetic fields well below the diffraction limit in conventional dielectric photonics [1], [2]. Consequently, they have been explored and implemented in numerous areas ranging from high-speed information processing [3]–[5] to single-molecule spectroscopy [6], [7].

A slit in metal is one of the simplest nanoaperture geometries that exhibit the desired properties of surface plasmons. Among many others, they include sub-wavelength mode confinement both on and off resonance, field enhancement up to several orders of magnitude [8], [9], and the provision for control and manipulation of light at the nanoscale [10]. Over the last two decades, slits have received widespread attention on both theoretical and experimental fronts as their simple geometries present a relatively easier route to understanding light-matter interactions [11]–[15].

Similarly, slots in metals offer two-dimensional localization of electromagnetic energy over a wide range of frequencies [16]. This is an advantage over other nanostructures that offer mode confinement only near the surface plasmon frequency [17]. Plasmonic slots are employed in waveguiding applications due to their ability to sustain modes with high propagation lengths and group velocities at the optical communication wavelengths [16], [18]. They also have lower scattering losses at bends compared to their dielectric counterparts [19]. In addition, the two metal layers allow the passage of electrical and optical signals in the same circuitry, opening up the possibility of the integration of CMOS electronics with conventional photonics [20]. It enables the simultaneous utilization of the subwavelength operation of the first and the large bandwidth operation of the latter [3], [4], [21]–[25].

Despite the several benefits, devices based on surface plasmons inadvertently suffer from losses that limit their implementation in some scenarios and prevent their widespread adoption in others [26]. Another caveat linked to the absorption losses is that they scale up with mode confinement, which means that tighter mode confinement leads to larger amounts of losses. This trade-off necessitates the careful optimization of their geometry for finding a balance between mode localization and propagation length. Other application-specific challenges include achieving

high sensitivity in sensing applications and optimizing electronic response times (i.e., managing capacitance) in optoelectronic applications [27].

The most common approach in plasmonic design involves the use of numerical methods. Numerical methods have been shown to be accurate in most cases, however, due to their computational complexity, they have to rely on high computing power to achieve the desired level of accuracy. In addition, any change in a source parameter such as the wavelength or polarization angle, or structural parameter such as the gap width in a slit requires a new simulation. Therefore, they do not provide any physical insights into the actual interactions of light in the plasmonic geometry. 2D simulations, which are useful for slit geometry are significantly faster than 3D simulations. However, for cases involving long wavelengths and narrow gaps, very fine spatial meshing is required to be able to capture the decaying fields accurately. This reduces the upper bound on the temporal mesh size for the Courant stability condition to be satisfied, ultimately making numerical simulations considerably more time and memory-intensive [28].

The above challenges can be addressed by analytical models that express desired properties in terms of their dependence on other physical parameters and rapidly evaluate these properties for the required configurations. We developed two analytical frameworks for this purpose. The first analysis was focused on metallic slits, where we used power as a figure of merit as opposed to field enhancement, to optimize slit geometry. We also established how the relationship between the scattering and the absorption cross-section of the slit has a strong impact on this power [28]. The second model centered on reflection and propagation in plasmonic slot waveguides. Using the model we were able to accurately determine the properties of modes sustained by the waveguide such as the mode effective index and the propagation length. These analytical methods were found to be

at least two orders of magnitude faster than numerical simulations [27]. The analysis can be used to design and optimize metallic slits and plasmonic slot waveguides for various applications and can also be extended to other plasmonic geometries.

1.2 Thesis Contributions

This dissertation focuses on analytical frameworks developed to investigate the reflection and propagation of electromagnetic waves in metallic slits and plasmonic slot waveguides. The main contributions of the author include:

1. Derivation of a purely analytic equation for reflection coefficient at the interface of a subwavelength metallic slit with its surrounding dielectric.

2. Derivation of expressions for scattering and absorption cross-sections in a slit using the Fabry-Pérot transmission model.

3. Determination of the condition for maximum power transfer in the slit.

4. Derivation of an analytic expression for reflection coefficient at the slot's interface with surrounding dielectric using perfect electric conductor approximation and dielectric loading.

5. Evaluation of modal properties such as mode effective index and propagation length in a plasmonic slot waveguide using a geometric optics approach.

The author has contributed to two journal articles (one accepted and one under review) that are the basis of this thesis. A brief overview of each article and the contributions of individual authors are listed in the following section.

1.2.1 Maximum power transfer in a real metal slit: an analytic approach [28]

This work presented an analytical framework to calculate the reflection in a metallic slit without having to resort to any numerical methods including numerical integration. This was achieved by using single-mode matching to continuum in combination with perfect electric conductor approximation and dielectric loading. Expressions for scattering and absorption cross-sections, field enhancement, and power in the slit were derived. It was shown that the total power through the slit peaks when the scattering cross-section equals the absorption cross-section, which is a manifestation of the maximum power transfer theorem.

Amrita Pati derived the equations, performed the numerical simulations, and wrote the manuscript. Reuven Gordon conceived the idea, formulated the theory, and wrote the manuscript.

1.2.2 Plasmonic Slot Waveguide Propagation Analysis [27]

In this work, our analysis of slit was extended to plasmonic slot waveguides that are used in diverse applications, yet the majority of the theoretical works exploring this geometry rely on numerical simulations. Numerical methods determine propagation properties accurately however, they do not provide any insights into the physics of mode propagation. In contrast, the analytical approach proposed in this article, determines modal properties in terms of other physical parameters, providing a way to understand light-matter interactions at the nano-scale and optimize slot geometry for different applications.

Amrita Pati derived the equations, performed the numerical simulations, and wrote the manuscript. Reuven Gordon formulated the theory and wrote the manuscript.

1.3 Organization of the Thesis

This section provides an outline of the chapters included in this thesis and also a brief description of the contents of each chapter.

Chapter 1 provides an introduction to the thesis and the motivation behind the research presented in this dissertation.

Chapter 2 includes the theoretical background relevant to metallic slits and plasmonic slot waveguides, the two main areas of focus in the thesis.

Chapter 3 presents a purely analytical approach developed to understand light-matter interactions in a 2D metallic slit, the results of the analysis, and their comparison with existing works and numerical simulations.

Chapter 4 covers the analytical framework developed to determine the modal properties in plasmonic slot waveguide, presents the results and their comparison with numerical simulations.

Chapter 5 concludes the thesis and discusses the scope of analytical methods in plasmonics and related applications.

Chapter 2

Background

Plasmonics is the study of interactions of electromagnetic waves with conduction electrons at metal-dielectric interfaces. These interactions result in the confinement of electromagnetic energy into extremely small dimensions due to the excitation of surface modes [2]. An important feature of these modes is that they are not restrained by the classical diffraction limit [1], [2]. Metal-dielectric geometries sustaining them have been implemented in diverse applications ranging from spectroscopy [6], [7] and sensing [29] to lithography [30].

The surface modes are known as surface plasmon polaritons (SPPs) or simply surface plasmons (SPs). They exist at the interface between a dielectric and a conductor and arise due to the coupling of electromagnetic fields with longitudinal oscillations of conduction electrons or plasma in a metal. SPPs are also known as bound modes as they remain confined to the metal-dielectric interface and decay exponentially in the perpendicular direction.

On first look, most metals are opaque to electromagnetic radiation below the ultraviolet, which means most of the light incident is reflected, while the remaining is absorbed [23]. However, when certain conditions are met, the excitation of SPs brings enhanced light-matter interactions to the foreground. There are two types of SPPs: localized (or non-propagating) surface plasmon (LSP) and propagating surface plasmon polaritons (PSPP).

2.1 Localized Surface Plasmon

Localized surface plasmons also known as particle plasmons, are non-propagating surface modes confined to metallic nanoparticles of dimensions much smaller than the wavelength of incident radiation (λ). When the size of a particle is smaller than the skin depth of electromagnetic waves in metals, electromagnetic fields fully penetrate into the nanoparticle and cause charge separation. On the other hand, the attraction between the positive and negative charges acts as a restoring force as shown in Figure 2.1. The whole system can therefore be thought of as an electromechanical oscillator [2]. When the frequency of the external driving field matches the frequency of the SP oscillations (ω_{SP}), the system is said to be in resonance. Resonance is linked to enhanced light-matter interactions leading to field enhancements up to several orders of magnitude.

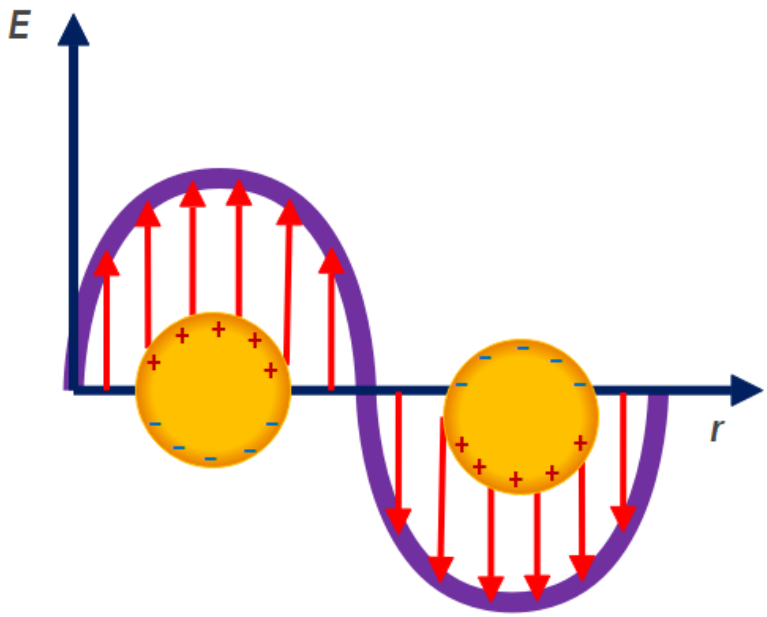

FIGURE 2.1: Localized surface plasmons as an oscillating system where the driving force is an external electric field (of wavelength much longer than the nanoparticle dimensions) that creates charge separation. Restoring force is provided by the electrostatic attraction between the opposite charges.

Different topologies of metal-dielectric nanoparticles sustaining LSPs such as spheres, ellipsoids, and nanodimers have been explored using the quasistatic approximation. The approximation applies to particles of dimension (a) much smaller than the wavelength. Considering the wave equation for scalar potential [31]:

$$(\nabla^2 + k^2)V(r) = -\frac{\rho(r)}{\epsilon} \tag{2.1}$$

For $a \ll \lambda$, $\nabla^2 V \gg k^2 V$ as $\nabla^2 \propto \frac{1}{a^2}$ and $k^2 \propto \frac{1}{\lambda^2}$

∇ is the gradient, k is the wave vector, $V(r)$ is the electric scalar potential, ϵ is the permittivity of the medium, and $\rho(r)$ is the charge density.

Therefore, in the quasistatic limit, the wave equation reduces to the Poisson equation of electrostatics [31]:

$$\nabla^2 V(r) = -\frac{\rho(r)}{\epsilon} \tag{2.2}$$

For a spherical nanoparticle of radius a and frequency-dependent permittivity $\epsilon_1(\omega)$ suspended in a medium of permittivity ϵ_2, the fields inside and outside the particle can be calculated by solving the Poisson's equation in spherical coordinates and applying the boundary conditions. The derived field equations are expressed as follows:

$$E(r < a) = \frac{3\epsilon_1}{\epsilon_2 + 2\epsilon_1(\omega)} E_0 \tag{2.3}$$

$$E(r > a) = E_0 + \frac{3\hat{n}(\hat{n}.p) - p}{4\pi\epsilon_0\epsilon_1(\omega)} \frac{1}{r^3} \tag{2.4}$$

E_0 is the external electric field, $\hat{n}$ is the unit vector along the direction of the electric field and p is the dipole moment of an optically excited sphere given as:

$$p = 4\pi\epsilon_1\epsilon_0 \left[\frac{\epsilon_2 - \epsilon_1(\omega)}{\epsilon_2 + 2\epsilon_1(\omega)}\right] a^3 E_0 \tag{2.5}$$

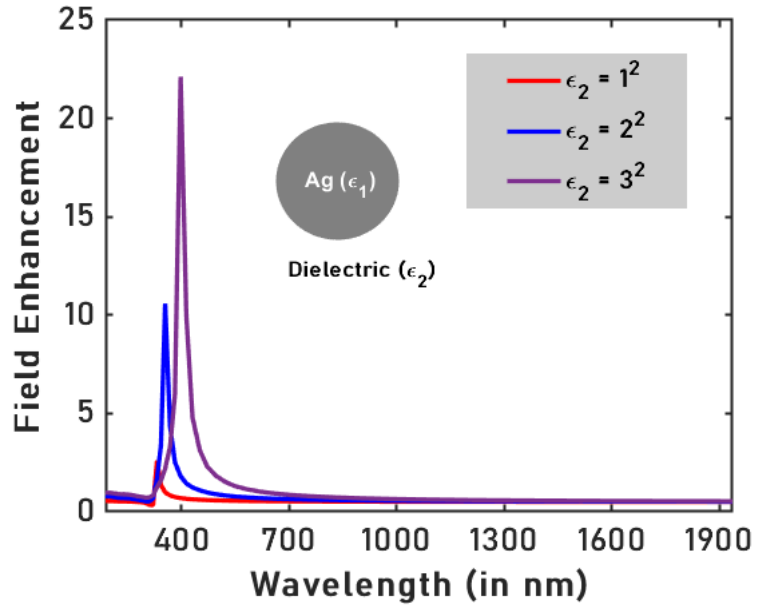

(A)

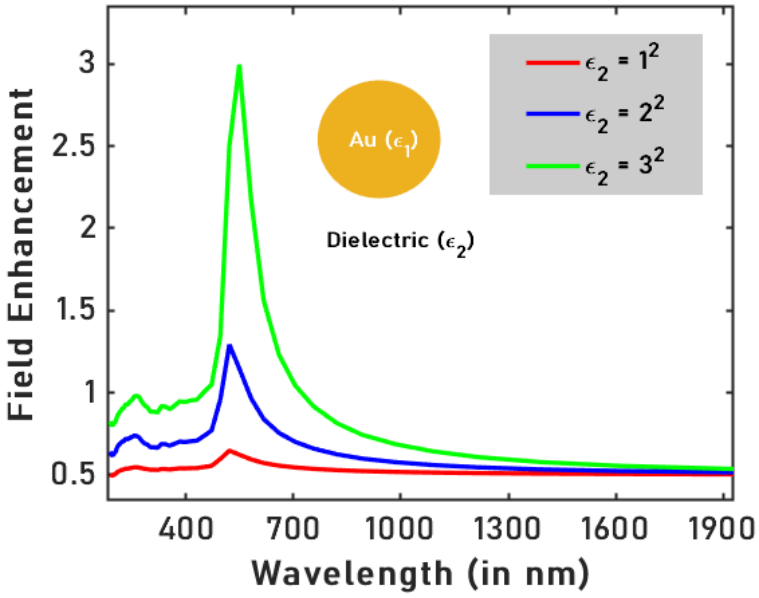

(B)

FIGURE 2.2: (A) Electric field enhancement in Ag (B) Au nanospheres for different values of permittivity of surrounding medium calculated from Eq. 2.3.

The field in the sphere will be maximum when $\epsilon_2 + 2\epsilon_1(\omega)$ has the smallest

possible magnitude, this condition is known as localized surface plasmon resonance (LSPR). The field enhancement in gold and silver nanospheres in different surrounding dielectric media are shown in Figure 2.2. The different values of plasmonic enhancement in Ag and Au are a result of the electronic transitions underlying their optical properties. The electrons in Au experience a large electrostatic attraction due to Au's high atomic number. This raises the energy of the $5d$ orbital and lowers the energy of the $6sp$ orbital, shifting the absorption associated with the $5d \rightarrow 6sp$ transition from the ultraviolet to the visible region. The increased absorption is manifested in the larger values of $\Im[\epsilon_1(\omega)]$ of Au compared to Ag. Due to higher losses in the visible region, Au has a lower plasmonic enhancement. The more negative values of $\Re[\epsilon_1(\omega)]$ of Ag in the visible region also contribute to the higher enhancement.

The SPR frequency is red-shifted with an increase in the permittivity of the surrounding medium. The shift in the frequency can be tracked in real-time to determine changes in surrounding media for sensing applications. For spherical gold nanoparticles, the sensitivity has a moderate value of 70 nm/RIU [32]. Tuning the shape of the nanoparticle has a strong impact on the sensitivity of the nanoparticle. For instance, significantly improved values are observed for spheroidal nanoparticles. As shown in Figure 2.3a the red-shift in SPR frequency with an increase in the permittivity of the dielectric medium is much higher than spherical Au nanoparticles and can be further improved by changing the aspect ratio of the spheroid as shown in Figure 2.3b. The curves show the field enhancement at the tip of the major axis of the spheroid when the electric field is along the same direction. Mathematically, it can be written as [33]:

$$E_{\text{tip}} = \frac{\epsilon_1(\omega)}{\epsilon_2 + L(\epsilon_1(\omega) - \epsilon_2)} E_0 \tag{2.6}$$

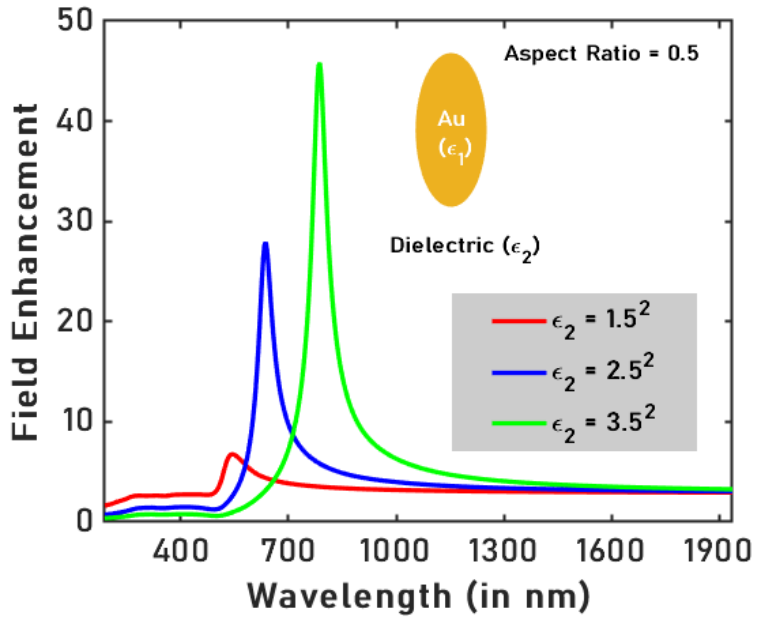

(A)

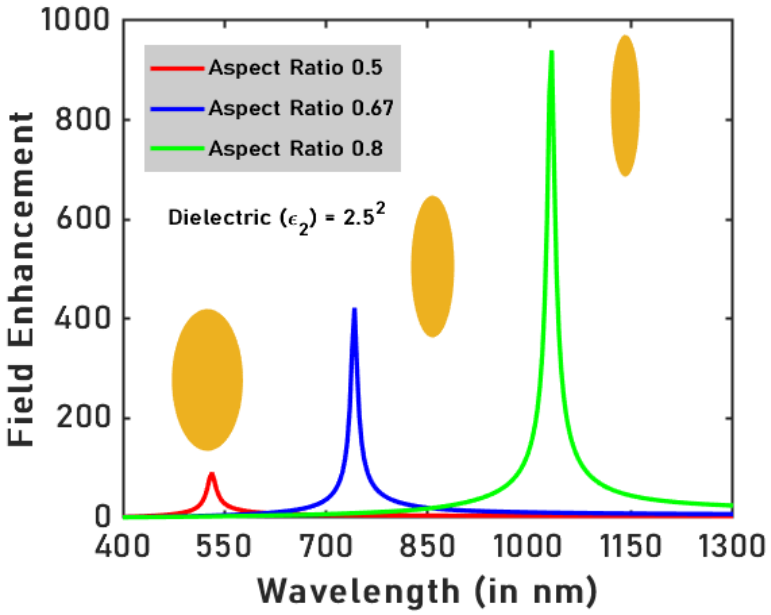

(B)

FIGURE 2.3: (A) Electric field enhancement at the tip of Au spheroidal nanoparticles of aspect ratio 0.5 in different dielectric media (B) Field enhancement at the tip of Au spheroidal nanoparticles in a dielectric medium of permittivity 6.25 for different aspect ratios calculated using Eq. 2.6.

$\epsilon_1(\omega)$ is the permittivity of the spheroid, ϵ_2 is the permittivity of the surrounding medium, E_0 is the incident electric field, and L is the depolarization factor along the long axis of the particle given as [33]:

$$L = \frac{1-e^2}{e^2}\left(-1 + \frac{1}{2e}\log\frac{1+e}{1-e}\right) \tag{2.7}$$

e is the eccentricity of the spheroid written as $\sqrt{1-\mathrm{AR}^2}$ and AR is the aspect ratio of the spheroid.

The detailed analysis of fields and optical cross-sections for spheroidal nanoparticles can be found in existing works [33]. Other shapes such as nanoprisms [34], nanorods, and core-shell nanoparticles have also demonstrated several folds higher sensitivity than spherical nanoparticles [32]. They have been successfully applied to investigate physiological processes such as antibody-antigen interactions and DNA interactions [35].

LSPR strongly enhances the scattering and the absorption cross-sections of the nanoparticle. Consequently, they are used for high-contrast imaging of biological systems [36]. Conjugated gold nanoparticles with emissions several orders of magnitude higher than conventional biological dyes are used for molecule-specific targeting and target-specific drug delivery, a crucial component of treating diseases like cancer where specificity is essential to avoid targeting healthy cells [37].

The sensitivity of LSPP to surroundings has been of great relevance in other areas such as electrochemistry, where metallic nanoparticles have been shown to improve the selectivity and catalytic activity of compounds [38]. LSPR is also utilized in optoelectronic applications such as solar cells and LEDs to obtain higher efficiencies from the enhanced absorption and emission strength of materials respectively [39], [40]. In the remainder of this dissertation, we will focus on propagating SPP which is the main theme of this work.

2.2 Propagating Surface Plasmons at a Metal-Insulator Interface

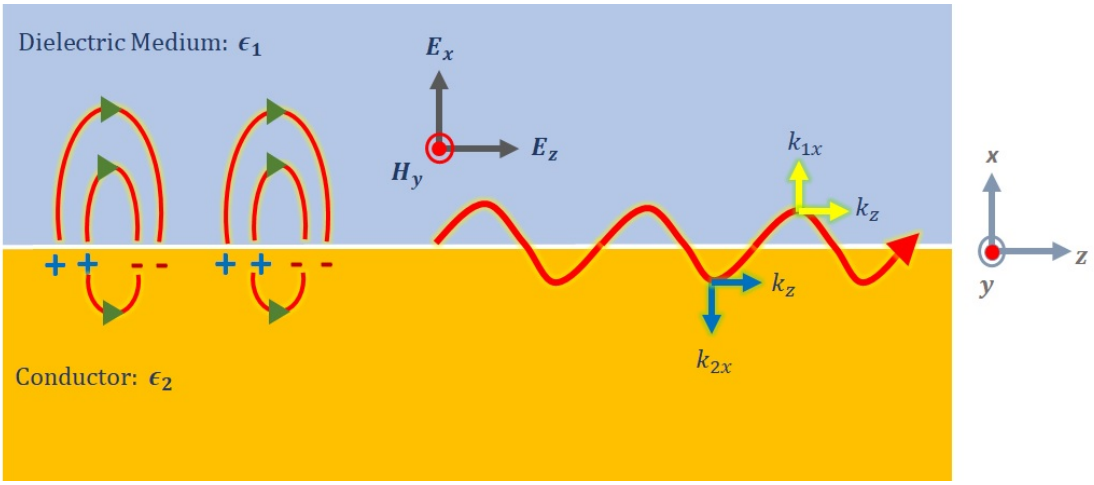

FIGURE 2.4: Propagating surface plasmon polaritons along a metal-dielectric interface, decaying exponentially into the neighboring media in the direction perpendicular to the interface.

The simplest geometry that allows the existence of propagating SPPs is a single, flat metal-insulator interface. Figure 2.4 shows the schematic of an interface where the upper half-plane in the x-direction is filled with a dielectric of permittivity ϵ_1 and the lower half-plane is a conductor with frequency-dependent permittivity $\epsilon_2(\omega)$. ϵ_0 and μ_0 are the absolute permittivities and permeability respectively. Assuming that the incoming electromagnetic field is TM-polarized, the electric field is oriented along the x (E_x) and the z (E_z) directions whereas the magnetic field (H_y) is oriented along the y-direction. The propagation constant in medium 1 is k_1 $(k_{1x}, 0, k_z)$ and in medium 2 is k_2 $(k_{2x}, 0, k_z)$.

The propagation constant of the SPP in the z-direction (k_z), being the tangential component is conserved across the boundary and can be calculated by the continuity of the fields. The SPPs decay exponentially in the direction perpendicular to the interface implying that k_{1x} can be replaced by $i\kappa_{1x}$ and k_{2x} can be replaced by $-i\kappa_{2x}$

to satisfy this condition. The electric and the magnetic fields in both the media can therefore be expressed as [41]:

For $(x > 0)$

$$H_{1y} = h_1 \exp(-\kappa_{1x} x) \exp(ik_z z) \tag{2.8}$$

Electric fields can be calculated by using Ampere's law:

$$E_{1z} = i\kappa_{1x} h_1 \frac{1}{\omega \epsilon_0 \epsilon_1} \exp(-\kappa_{1x} x) \exp(ik_z z) \tag{2.9}$$

$$E_{1x} = -k_z h_1 \frac{1}{\omega \epsilon_0 \epsilon_1} \exp(-\kappa_{1x} x) \exp(ik_z z) \tag{2.10}$$

Similarly, for $(x < 0)$

$$H_{2y} = h_2 \exp(\kappa_{2x} x) \exp(ik_z z) \tag{2.11}$$

$$E_{2z} = -i\kappa_{2x} h_2 \frac{1}{\omega \epsilon_0 \epsilon_2(\omega)} \exp(\kappa_{2x} x) \exp(ik_z z) \tag{2.12}$$

$$E_{2x} = -k_z h_2 \frac{1}{\omega \epsilon_0 \epsilon_2(\omega)} \exp(\kappa_{2x} x) \exp(ik_z z) \tag{2.13}$$

At the boundary $(x = 0)$, $H_{1y} = H_{2y} \implies h_1 = h_2$

$$E_{1z} = E_{2z} \implies \frac{\kappa_{1x}}{\kappa_{2x}} = -\frac{\epsilon_1}{\epsilon_2(\omega)} = \implies \frac{k_z^2 - \epsilon_1 k_0^2}{k_z^2 - \epsilon_2(\omega) k_0^2} = \frac{\epsilon_1^2}{\epsilon_2(\omega)^2} \tag{2.14}$$

The above equation can only be satisfied for real values of κ_{1x} and κ_{2x} when ϵ_1 and $\epsilon_2(\omega)$ are opposite in signs. This is one of the conditions required for the excitation of surface modes. Solving the above equation gives:

$$k_z = k_0 \sqrt{\frac{\epsilon_1 \epsilon_2(\omega)}{\epsilon_1 + \epsilon_2(\omega)}} \tag{2.15}$$

Assuming ϵ_1 to be positive and $\epsilon_2(\omega)$ to be negative, for k_z to be real $\epsilon_1 + \epsilon_2(\omega) > 0$, or $-\epsilon_2(\omega) > \epsilon_1$, which is another condition required to sustain SPPs at

the interface.

In the previous section, it has been mentioned that the surface modes can be excited by TM-polarized light. This is intuitively understood by the fact that the electron oscillations are longitudinal and for a TE-polarized source, there is no component of the electric field in the propagation plane. It can also be shown mathematically as follows [41]:

For $(x > 0)$

$$E_{1y} = e_1 \exp(-\kappa_{1x} x) \exp(ik_z z) \tag{2.16}$$

Magnetic fields are given as:

$$H_{1z} = i\kappa_{1x} e_1 \frac{1}{\omega\mu_0} \exp(-\kappa_{1x} x) \exp(ik_z z) \tag{2.17}$$

$$H_{1x} = -k_z e_1 \frac{1}{\omega\mu_0} \exp(-\kappa_{1x} x) \exp(ik_z z) \tag{2.18}$$

Similarly, for $(x < 0)$

$$E_{2y} = e_2 \exp(\kappa_{2x} x) \exp(ik_z z) \tag{2.19}$$

$$H_{2z} = -i\kappa_{2x} e_2 \frac{1}{\omega\mu_0} \exp(\kappa_{2x} x) \exp(ik_z z) \tag{2.20}$$

$$H_{2x} = -k_z e_2 \frac{1}{\omega\mu_0} \exp(\kappa_{2x} x) \exp(ik_z z) \tag{2.21}$$

At the boundary $(x = 0)$,

$E_{1y} = E_{2y} \implies e_1 = e_2$

$$H_{1z} = H_{2z} \implies i\kappa_{1x} e_1 = -i\kappa_{2x} e_2 \implies e_1(\kappa_{1x} + \kappa_{2x}) = 0 \tag{2.22}$$

The above condition is satisfied only when $e_1 = e_2 = 0$ or $\kappa_{1x} = -\kappa_{2x}$. The first condition is trivial. The second can not be met because for surface modes to exist, the real parts of both κ_{1x} and κ_{2x} must be greater than 0. Figure 2.5 shows the dispersion relation of SPPs at silver-dielectric and gold-dielectric interfaces, permittivity values are taken from [42]. The momentum mismatch between photons and SPPs prevents the excitation of SPPs by direct irradiation at the metal-dielectric interface. Schemes involving prisms in various configurations [43], [44], waveguides [45], and gratings [46] have been proposed to excite SPPs by wave vector matching. In comparison to the excitation of LSP in nanoparticles, the relatively simpler coupling of a dielectric mode with PSPP through waveguide substrates favors their use in integrated optics [47].

Silver and gold are two of the most commonly used plasmonic materials due to their relatively lower levels of losses in the visible and near-infrared (NIR) regions [48]. The wavelength of the propagating SPP is given as $2\pi/\text{Real}(k_z)$ and the propagation length is $1/\text{Imag}(2k_z)$. By substituting the value of k_z, we obtain the following relationship between their tangential and normal components.

$$E_{1x} = i\sqrt{\frac{-\epsilon_2(\omega)}{\epsilon_1}}E_z \tag{2.23}$$

$$E_{2x} = -i\sqrt{\frac{-\epsilon_1}{\epsilon_2(\omega)}}E_z \tag{2.24}$$

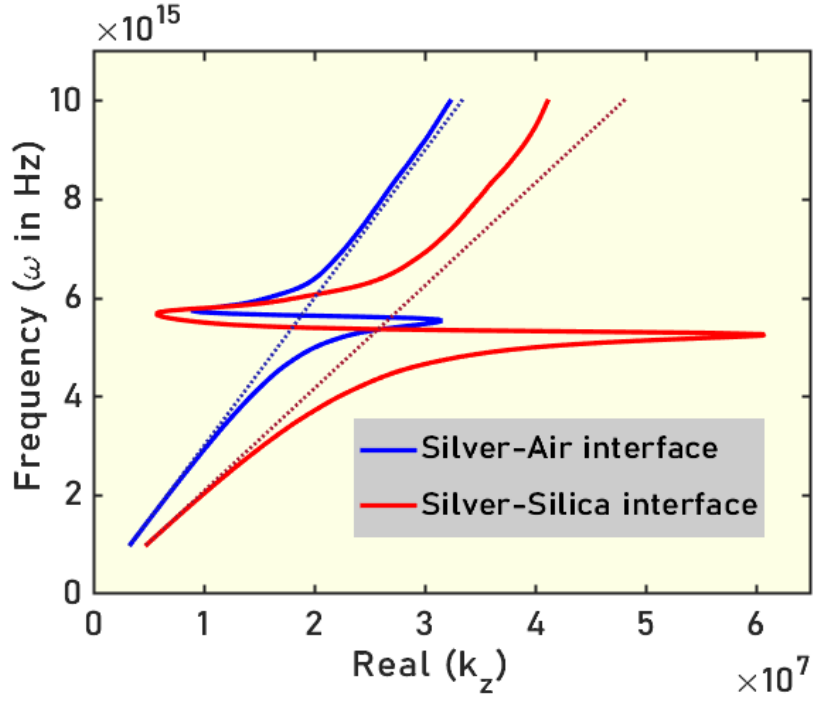

(A)

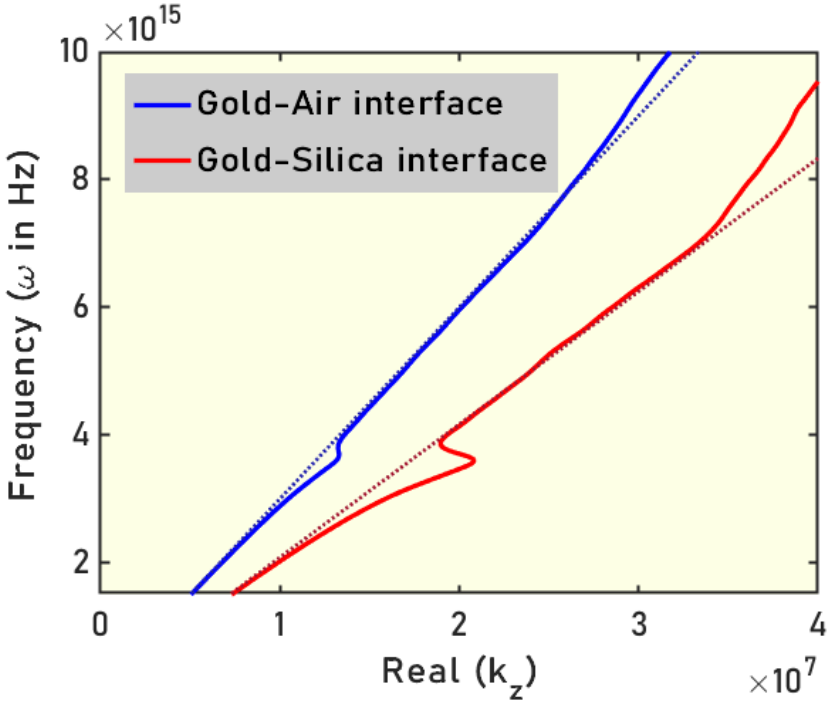

(B)

FIGURE 2.5: (A) Dispersion relation of a silver-air (solid blue line) and silver-silica (red line) interface and (B) Dispersion relation of a gold-air (solid blue line) and gold-silica (red line) interface. The dotted lines on both the figures represent the light line in the dielectric, blue for air and red for silica

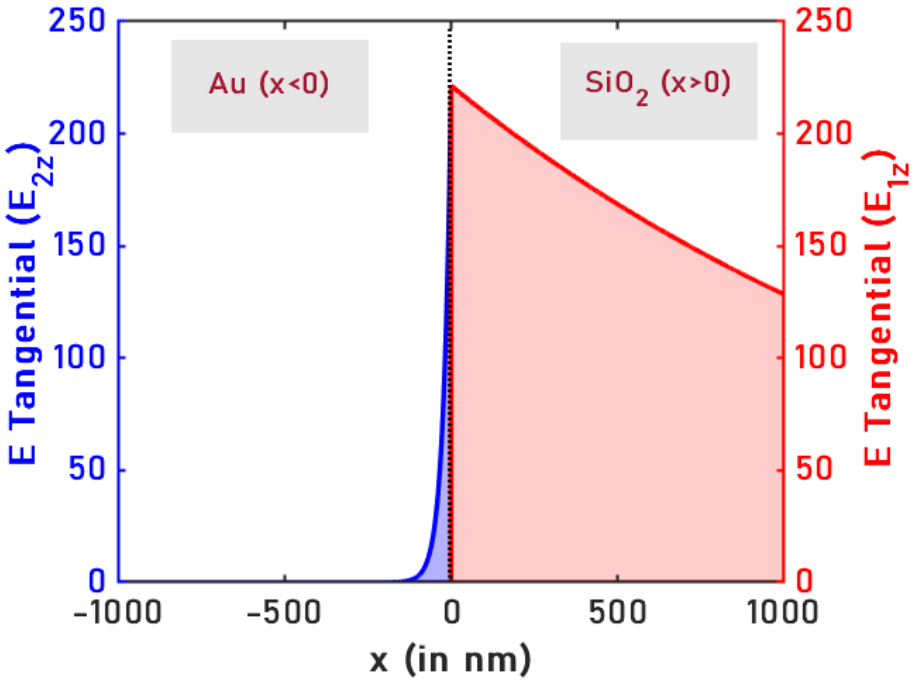

(A)

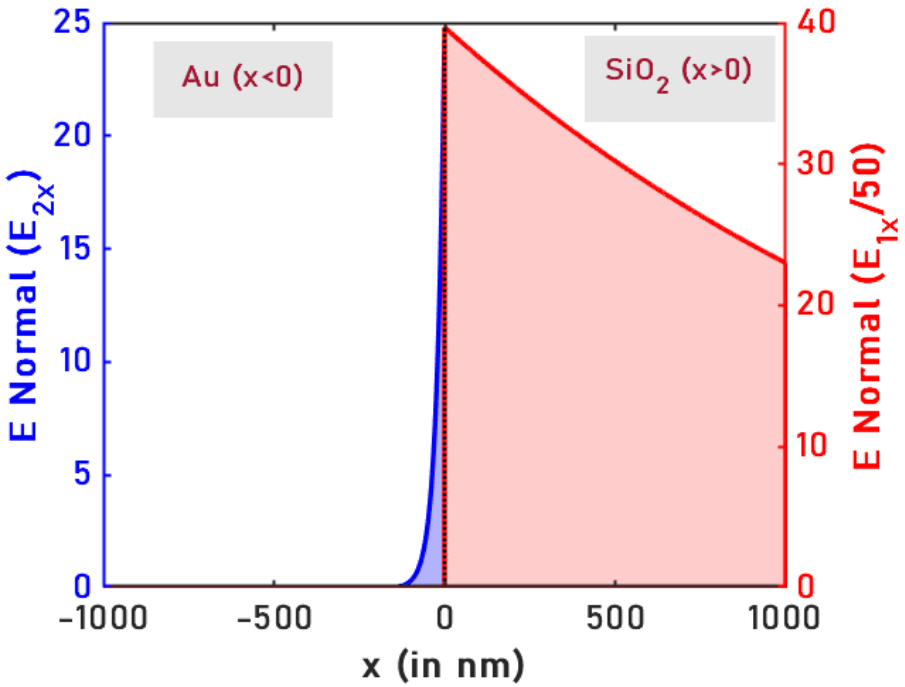

(B)

FIGURE 2.6: (A) Tangential and (B) normal components of electric fields in gold-silica interface using Eqs. 2.23, 2.24, 2.25. The vertical dotted line represents the interface ($x = 0$). The region ($x > 0$) is filled with silica and ($x < 0$) is gold

Here, $E_{1z} = E_{2z} = E_z$, since the tangential components of the electric field are continuous across a boundary, is expressed as:

$$E_z = i\frac{k_0}{\omega\epsilon_0}\sqrt{\frac{-1}{\epsilon_1 + \epsilon_2(\omega)}}\exp\left(ik_z.z\right) \tag{2.25}$$

In the visible and NIR regions, gold and silver have much larger magnitudes of permittivities compared to dielectric materials ($|\epsilon_2| \gg \epsilon_1$). Therefore, in metals, the tangential component of the electric field dominates over the normal components. Whereas, in the dielectric, the transverse components are significantly larger than the longitudinal component as shown in Figure 2.6.

2.3 Surface Plasmon Polaritons in Multilayered Systems

Structures with multiple metal-dielectric interfaces sustain SPPs at each interface. These modes can be coupled to each other when the distance between the interfaces is smaller than the decay length of the SPPs in the direction perpendicular to them. In this section, we focus on two structures: insulator-metal-insulator (IMI) where a metal layer is sandwiched between two insulators, and metal-insulator-metal (MIM) where an insulator is sandwiched between two metal layers. The coupled modes supported by these structures have been shown to be extremely confined resulting in a large field enhancement.

2.3.1 Insulator-Metal-Insulator Structure

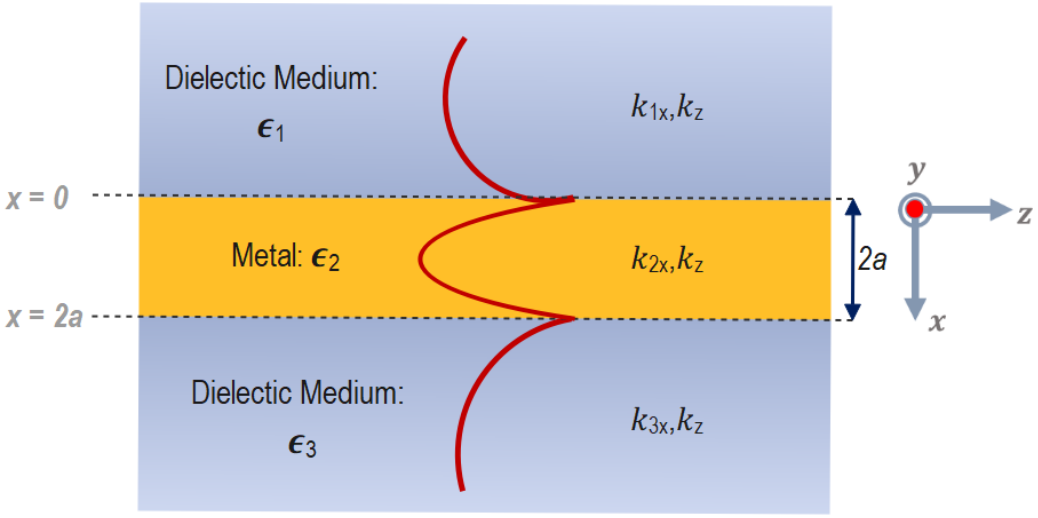

FIGURE 2.7: Schematics of an IMI structure. A metal film of thickness $2a$ and permittivity of ϵ_2 is surrounded by dielectric media of permittivity values ϵ_1 and ϵ_3.

In this geometry, a thin metal film is sandwiched between two insulator layers. The structure has two possible configurations: symmetric and asymmetric. Symmetric

geometry has the same dielectric surrounding the metal layer whereas, in asymmetric geometry, the metal is surrounded by two different dielectric media at the two interfaces.

Figure 2.7 shows the schematics of the IMI geometry under consideration. A metal film of thickness $2a$ (extending from 0 to $2a$) and permittivity ϵ_1 is sandwiched between two semi-infinite dielectric media of permittivity ϵ_1 and ϵ_3. The three layers are infinite in the y and z directions. The free-space wave vector is represented by k_0 and the propagation constant of the mode is k_z. The normal components of the wave vectors in the three media are given as:

$$k_{1x} = \sqrt{k_z^2 - \epsilon_1 {k_0}^2}$$
$$k_{2x} = \sqrt{k_z^2 - \epsilon_2 {k_0}^2}$$
$$k_{3x} = \sqrt{k_z^2 - \epsilon_3 {k_0}^2}$$

The transverse electric and magnetic (E_x and H_y) and tangential electric (E_z) fields are formulated as follows [49]:

In the first dielectric medium ($x \leq 0$):

$$H_{1y} = \frac{iCk_0\epsilon_1}{k_{1x}} \exp\left(k_{1x}x\right) \tag{2.26}$$

$$E_{1x} = \frac{k_z}{\omega\epsilon_1} H_{1y} \tag{2.27}$$

$$E_{1z} = C \exp\left(k_{1x}x\right) \tag{2.28}$$

In the metal layer ($0 \leq x \leq 2a$):

$$H_{2y} = \frac{-iCk_0\epsilon_2}{k_{2x}} \left[\sinh\left(k_{2x}x\right) + \frac{k_{2x}\epsilon_1}{k_{1x}\epsilon_2} \cosh\left(k_{2x}x\right)\right] \tag{2.29}$$

$$E_{2x} = \frac{k_z}{\omega\epsilon_2} H_{2y} \tag{2.30}$$

$$E_{2z} = C\left[\cosh\left(k_{2x}x\right) + \frac{k_{2x}\epsilon_1}{k_{1x}\epsilon_2}\sinh\left(k_{2x}x\right)\right] \tag{2.31}$$

In the second dielectric medium $(x \geq 2a)$:

$$H_{3y} = \frac{iCk_0\epsilon_3}{k_{2x}}\left[\cosh\left(2k_{2x}a\right) + \frac{k_{2x}\epsilon_1}{k_{1x}\epsilon_2}\sinh\left(2k_{2x}a\right)\right]\exp[-k_{2x}(x-a)] \tag{2.32}$$

$$E_{3x} = \frac{k_z}{\omega\epsilon_2}H_{2y} \tag{2.33}$$

$$E_{3z} = C\left[\cosh\left(2k_{2x}a\right) + \frac{k_{2x}\epsilon_1}{k_{1x}\epsilon_2}\sinh\left(2k_{2x}a\right)\right]\exp[-k_{2x}(x-a)] \tag{2.34}$$

C is the normalization constant and ω is the angular frequency.

Dispersion Relation of IMI Structure by Transfer Matrix Method

The dispersion relation of the coupled SPP in the metal layer can be calculated by the continuity of fields across the two interfaces. A simpler alternative is provided by an approach called the Transfer Matrix Method (TMM) [31]. It is used to calculate the propagation properties in a uniform 2D multilayered system. The total propagation through a structure is calculated by considering the reflection and transmission at each interface and the propagation through each medium. Assuming, E_{i} is the downward propagating electric field and E_{r} is the upward propagating electric field in the dielectric medium I. E_{t} is the downward propagating electric field in region III. By TMM the relationship between the fields can be written as follows:

$$\begin{bmatrix} E_{\mathrm{i}} \\ E_{\mathrm{r}} \end{bmatrix} = \frac{1}{4}\begin{bmatrix} 1+\kappa_{12}\eta_{12} & 1-\kappa_{12}\eta_{12} \\ 1-\kappa_{12}\eta_{12} & 1+\kappa_{12}\eta_{12} \end{bmatrix}\begin{bmatrix} e^{-\phi} & 0 \\ 0 & e^{\phi} \end{bmatrix}\begin{bmatrix} 1+\kappa_{23}\eta_{23} & 1-\kappa_{23}\eta_{23} \\ 1-\kappa_{23}\eta_{23} & 1+\kappa_{23}\eta_{23} \end{bmatrix}\begin{bmatrix} E_{\mathrm{t}} \\ 0 \end{bmatrix} \tag{2.35}$$

In the RHS of Eq. 2.35, the first and the third matrices represent the transmission and reflection at the two interfaces. The second matrix accounts for the phase acquired during propagation in the metal film. The other variables in the equation are defined as follows:

$$\kappa_{12} = \frac{k_{2x}}{k_{1x}} \text{ and } \kappa_{23} = \frac{k_{3x}}{k_{2x}}$$

$$\eta_{12} = \frac{\epsilon_1}{\epsilon_2} \text{ and } \eta_{23} = \frac{\epsilon_2}{\epsilon_3}$$

where, $\phi = k_{2x} \times 2a$

Eq. 2.35 is solved to obtain the dispersion relation of the mode in the IMI structure by setting E_{i} as 0:

$$\tanh(2\kappa_{1x}a) = \frac{-\epsilon_2\kappa_{2x}(\kappa_{3x}\epsilon_1 + \kappa_{1x}\epsilon_3)}{\epsilon_1\epsilon_3\kappa_{2x}^2 + \epsilon_2^2\kappa_{1x}\kappa_{3x}} \tag{2.36}$$

For a symmetric IMI structure, we set $\epsilon_1 = \epsilon_3 = \epsilon_d$ and $\epsilon_2 = \epsilon_m$. This leads us to two implicit equations for the propagation constant of the SPP, given as:

$$\tanh\left[\sqrt{k_z^2 - \epsilon_m {k_0}^2}a\right] = \frac{-\epsilon_m\sqrt{k_z^2 - \epsilon_d {k_0}^2}}{\epsilon_d\sqrt{k_z^2 - \epsilon_m {k_0}^2}} \tag{2.37}$$

$$\tanh\left[\sqrt{k_z^2 - \epsilon_m {k_0}^2}a\right] = \frac{-\epsilon_d\sqrt{k_z^2 - \epsilon_m {k_0}^2}}{\epsilon_m\sqrt{k_z^2 - \epsilon_d {k_0}^2}} \tag{2.38}$$

Eq. 2.37 represents the SPP mode for symmetric distributions of E_x and H_y and anti-symmetric distribution of E_z. The symmetric distribution of H_y is shown in Figure 2.8a. Similar to a single metal-dielectric interface, the tangential component of electric field (E_z) dominates in the metal film, whereas the normal component (E_x) dominates in the dielectric media. The propagation constant, as a result, is more dependent on the longitudinal component (E_z). For the symmetric

mode, since E_z has a zero-crossing in the metal film, it experiences much lower attenuation than the anti-symmetric mode resulting in significantly longer propagation lengths. These modes are also known as long-range surface plasmon polaritons (LRSPP).

Eq. 2.38 represents the anti-symmetric mode of SPPs in IMI structures. The distributions of E_x and H_y are anti-symmetric and the distribution of E_z is symmetric. The transverse electric and magnetic fields exhibit a zero in the metal region. The anti-symmetric distribution of H_y is shown in Figure 2.8b. The mode has a shorter propagation length than the symmetric mode and is also known as short-range surface plasmon polaritons (SRSPP).

Figure 2.9a shows the variation of the effective index and propagation length of the symmetric and asymmetric SPP modes with the metal thickness at a wavelength of 1550 nm. The red lines represent the propagation lengths and the blue lines represent the effective indices. The propagation constant or effective index of SRSPP, represented by the blue dashed line increases with decreasing metal thickness, approaching ∞ as $a \to 0$. Conversely, the propagation length shown by the red dashed line decreases and approaches 0 for infinitely thin films. In contrast, the effective index of LRSPP, shown by the blue solid line, increases with an increase in metal thickness. The propagation length of LRSPPs increases infinitely as the thickness $a \to 0$.

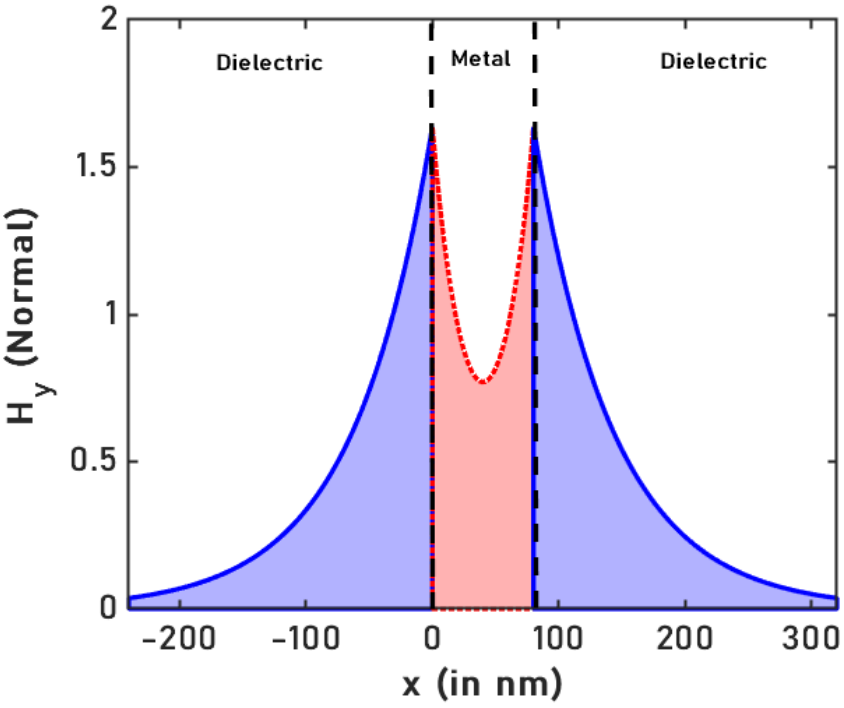

(A)

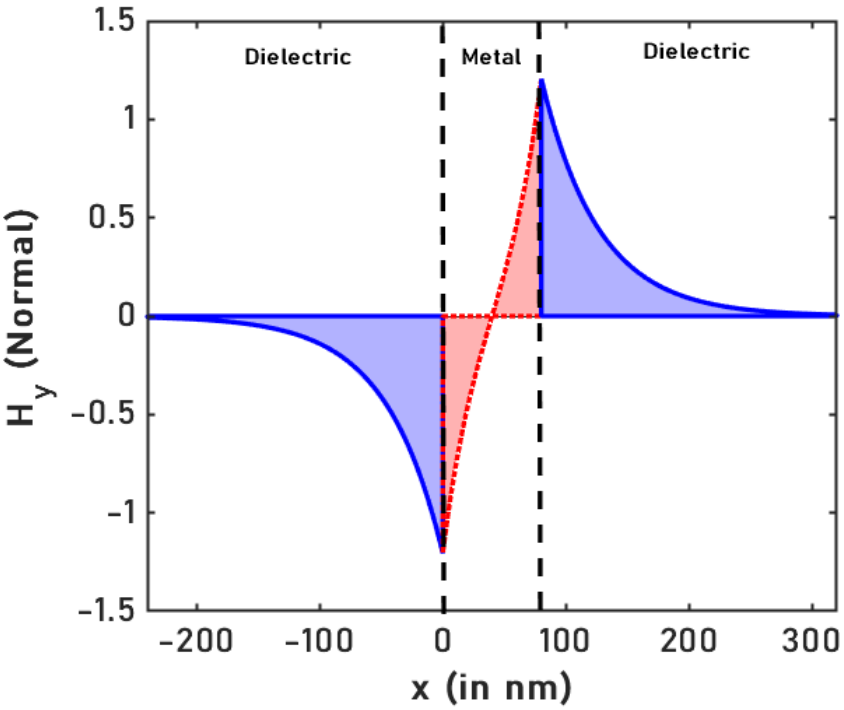

(B)

FIGURE 2.8: Transverse magnetic field (H_y) amplitude of (A) symmetric and (B) anti-symmetric modes in an IMI structure of metal thickness 80 nm, permittivity (ϵ_m) -4 and dielectric index of 1.44

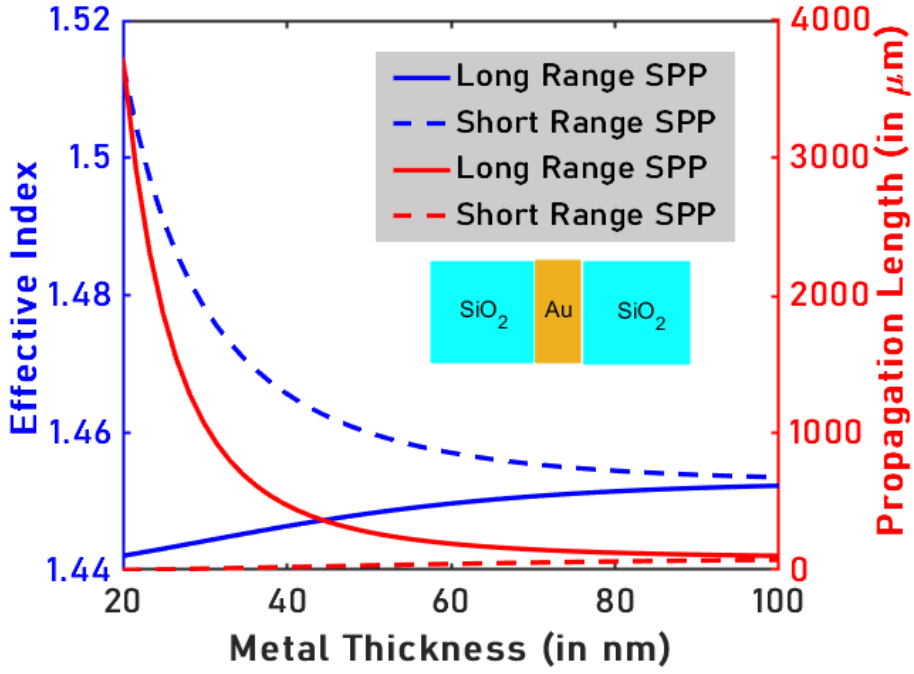

(A)

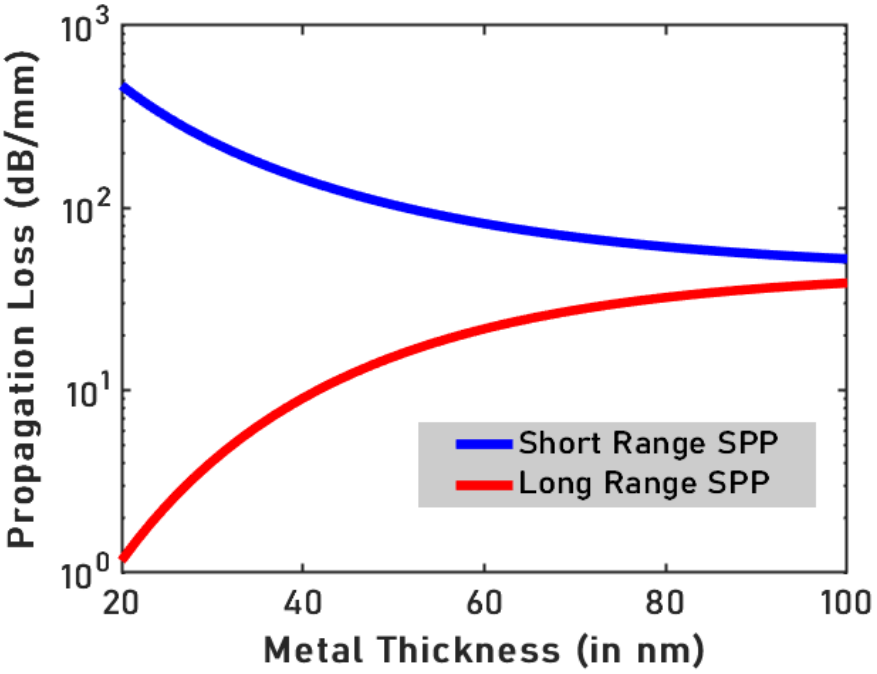

(B)

FIGURE 2.9: (A) Variation of the effective index (blue lines) and propagation length (red lines) for SRSPP (dashed lines) and LRSPP (solid lines) for silica-gold-silica structure of thickness 100 nm. (B) Variation of propagation losses (in dB/mm) of SRSPP and LRSPP modes.

For both symmetric and anti-symmetric field distributions when $a \gg$ skin depth, $\tanh\left[\sqrt{k_z^2 - \epsilon_m {k_0}^2} a\right] \rightarrow 1$. For very thick metal films, the IMI geometry consists of two decoupled SPPs with propagation constants equal to the propagation constant in a single metal-dielectric interface $= k_0 \sqrt{\frac{\epsilon_d \epsilon_m}{\epsilon_d + \epsilon_m}}$. Therefore their indices, represented by blue solid and dashed lines can be seen approaching the same value for increasing metal thickness in Figure 2.9a.

The propagation losses (in dB/mm) associated with SRSPP and LRSPP modes are shown in Figure 2.9b. The propagation losses of the SRSPP increase with narrowing metal thickness and approach ∞ as $a \rightarrow 0$. Conversely, the propagation losses of LRSPP approach 0 for infinitely thin metal films. This characteristic feature of the LRSPP encourages the application of IMI geometries in integrated optics [50].

2.3.2 Metal-Insulator-Metal Structure

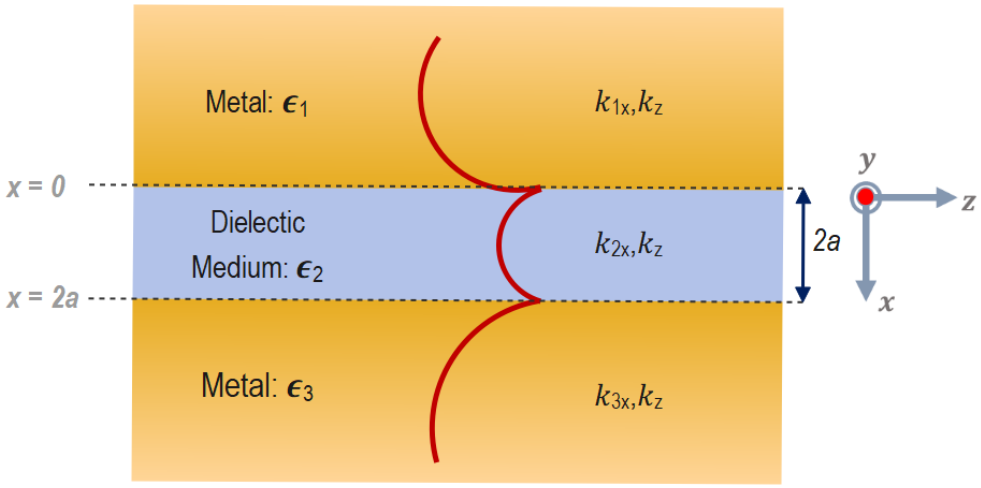

FIGURE 2.10: Schematics of a MIM structure. Dielectric medium of thickness $2a$ and permittivity of ϵ_2 is surrounded by metal films of permittivity values ϵ_1 and ϵ_3.

A MIM structure is formed by sandwiching a dielectric medium between two metallic films. MIM geometries have been explored by several studies due to their ability to confine light into extremely small dimensions over a wide range of frequencies. The majority portion of power resides in the dielectric core, which makes them highly desirable for waveguiding applications. Although higher confinement in the structure is linked to reduced propagation lengths, it is relatively cheaper to mitigate the losses compared to other geometries [51]. The constructive interference of the SPP modes often regarded as the gap plasmon modes generates large field enhancements at resonance, which favors their implementation in diverse applications.

The schematic of the MIM geometry is shown in Figure 2.10. A dielectric medium of permittivity ϵ_1 and width $2a$ is surrounded by two metals films extending infinitely in the y- and z- directions and semi-infinitely in the x-direction. The metal permittivities are represented by ϵ_1 and ϵ_3. The electric and magnetic fields remain the same as the equations derived for the IMI structure in Eqs. 2.26 through 2.34.

The dispersion relation of the structure also remains the same, only the permittivity of the dielectric is exchanged with the permittivity of the metal wherever relevant. For a symmetric MIM structure, the metal permittivity is represented by ϵ_m and the dielectric permittivity by ϵ_d. Similar to the case of the symmetric IMI geometry, we arrive at two implicit equations for the dispersion relation of the gap plasmon mode given as:

$$\tanh\left[\sqrt{k_z^2 - \epsilon_d {k_0}^2}a\right] = \frac{-\epsilon_d\sqrt{k_z^2 - \epsilon_m {k_0}^2}}{\epsilon_m\sqrt{k_z^2 - \epsilon_d {k_0}^2}} \tag{2.39}$$

$$\tanh\left[\sqrt{k_z^2 - \epsilon_d {k_0}^2}a\right] = \frac{-\epsilon_m\sqrt{k_z^2 - \epsilon_d {k_0}^2}}{\epsilon_d\sqrt{k_z^2 - \epsilon_m {k_0}^2}} \tag{2.40}$$

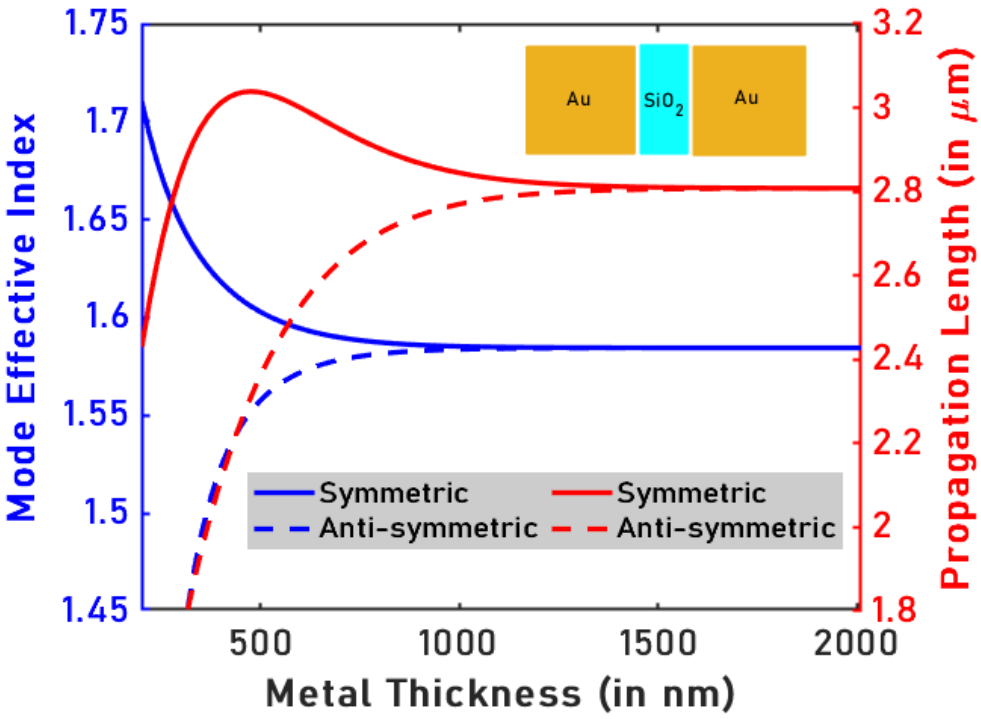

FIGURE 2.11: Variation of mode effective index (blue lines) and propagation length (red lines) of symmetric (solid lines) and anti-symmetric mode (dashed lines) of an MIM structure (gold-silica-gold). The figure shows the cut-off of the anti-symmetric mode.

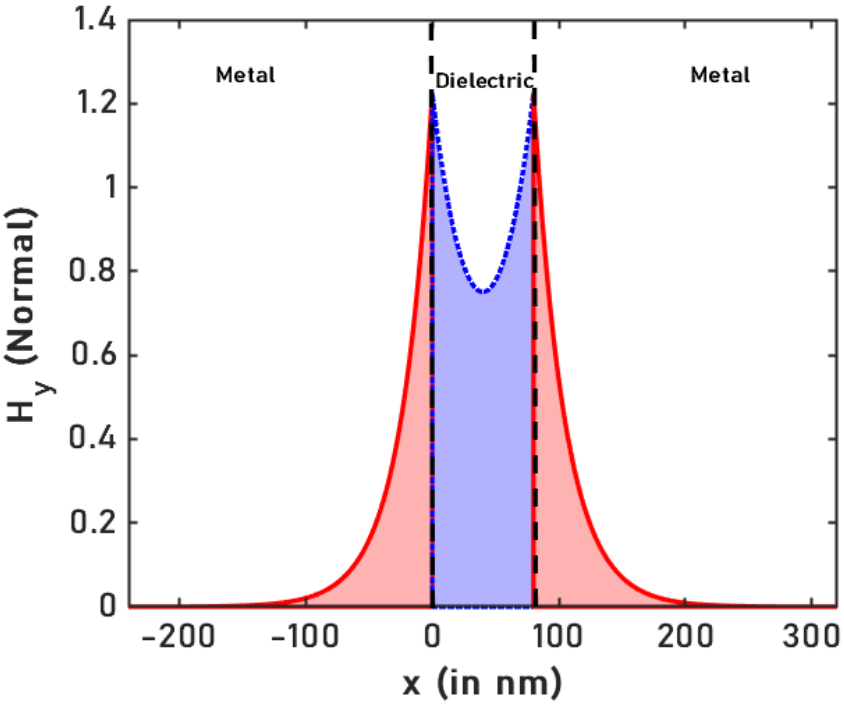

(A)

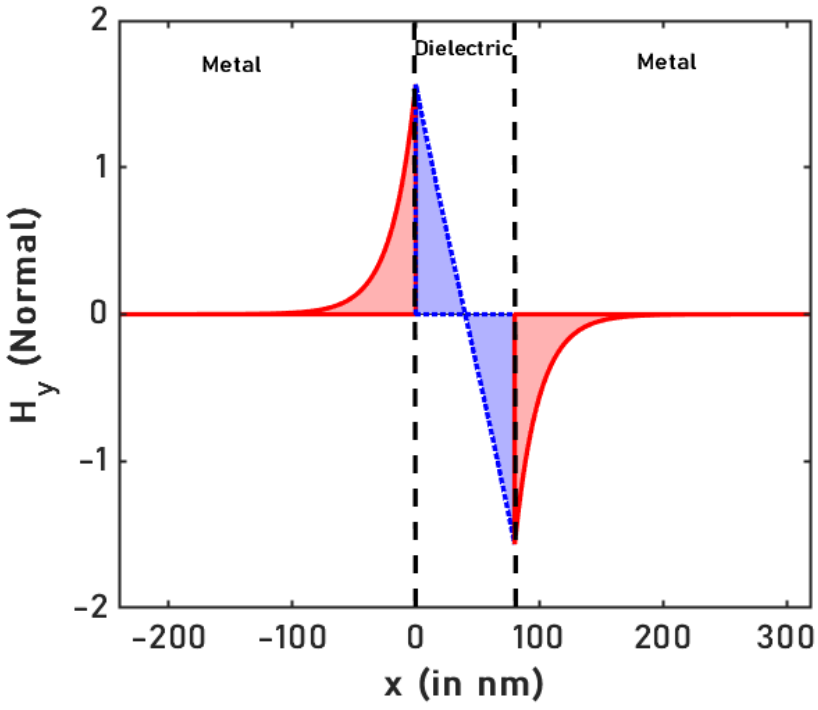

(B)

FIGURE 2.12: Transverse magnetic field (H_y) amplitude of (A) symmetric and (B) anti-symmetric modes in a MIM structure of metal thickness 80 nm, permittivity (ϵ_m) -4 and dielectric index of 1.44

Eq. 2.39 is the dispersion relation of the symmetric mode where the transverse electric fields have symmetric distribution (E_x and H_y) and the longitudinal electric field (E_z) has an anti-symmetric distribution. The anti-symmetric mode dispersion relation is given by Eq. 2.40. The transverse fields have anti-symmetric distribution and the tangential electric filed has a symmetric distribution. The transverse magnetic field (H_y) distribution of the symmetric and anti-symmetric modes are shown in Figures 2.12a and 2.12b.

In contrast to an IMI structure, the anti-symmetric mode in a MIM structure has a cut-off as shown in Figure 2.11. Below a certain metal thickness, the anti-symmetric mode becomes a radiative mode. In the subsequent sections of the dissertation, we refer to only the symmetric mode while considering the MIM geometry. The symmetric mode does not have a cut-off for any combination of source or geometric parameters. The mode index increases with the narrowing of the gap in MIM as an increasing amount of electric fields enter the higher refractive index metals. The propagation lengths vary in opposite fashion and get shorter with narrowing gaps.

2.3.3 Main Applications of PSPP

Surface Plasmon Resonance Sensing

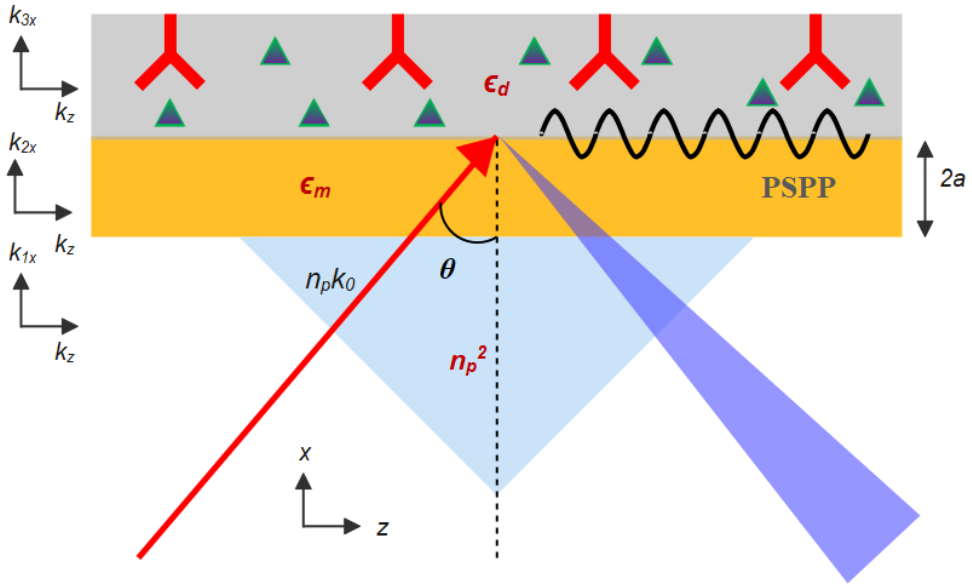

FIGURE 2.13: SPR sensor based on the excitation of propagating surface plasmons polaritons, momentum matching is achieved by Kretschmann configuration. The dip in reflected signal is tracked for sensing applications.

Similar to localized SPs, propagating SPPs are also highly sensitive to refractive index changes in the vicinity of the metal. Since the 1980s, they have been extensively used in real-time, rapid, label-free, and *in situ* sensing applications [52]. When TM-polarized monochromatic (or polychromatic based on requirements) light is incident on a metal-dielectric interface under certain conditions, it excites the SPs at the interface, this condition is also known as surface plasmon resonance (SPR). This observation was first reported by Wood in a grating configuration and since then several methods have been employed to excite the SPs and enhance their sensitivity to changes in their surroundings [53].

The prism-based Kretschmann configuration has become a standard technique in SPR sensing. The basic schematic of the configuration is shown in Figure 2.13 [44].

The medium to be analyzed is placed in contact with a metal layer. Light passing through a prism of index higher than the sensing medium undergoes attenuated total internal reflection (ATR) and the reflected light is received by a detector. When the tangential component of the incoming wave vector matches the propagation constant of the SPs, the energy of the incoming light is transferred to them resulting in a sudden dip in the amount of reflected light received by the detector.

The incidence angle at which the SPs are excited is also known as the SPR angle. Changes in the permittivity of the sensing medium can be mapped to changes in the SPR angle. Therefore, by tracking the SPR angle in real-time dynamic information about the permittivity of the sensing medium is gathered. The SPR angle can be determined quantitatively from the following equation:

$$n_p k_0 \sin\theta = k_0 \sqrt{\frac{\epsilon_d \epsilon_m}{\epsilon_d + \epsilon_m}} \tag{2.41}$$

n_p is the refractive index of the prism, θ is the angle of incidence, k_0 is the free-space wave-vector. ϵ_d is the permittivity of the sensing medium and ϵ_m is the permittivity of the metal layer. The reflected light received by the detector can be calculated by the TMM, shown in section 2.3.1 (all the variables are defined the in the same way). Using this approach, the reflectivity obtained for a simple three-layered SPR sensor is given as:

$$r = \left| \frac{(1-\kappa_{12}\eta_{12})(1+\kappa_{23}\eta_{23})e^{-ik_{2x}2a} + (1+\kappa_{12}\eta_{12})(1-\kappa_{23}\eta_{23})e^{ik_{2x}2a}}{(1+\kappa_{12}\eta_{12})(1+\kappa_{23}\eta_{23})e^{-ik_{2x}2a} + (1-\kappa_{12}\eta_{12})(1-\kappa_{23}\eta_{23})e^{ik_{2x}2a}} \right| \tag{2.42}$$

The shift in the SPR angle with changes in the permittivity of the sample is shown in Figure 2.14.

The SPR sensors have seen several advances over the last four decades, in an effort to detect analytes with extremely low molecular weight (<8 kDa) in very low

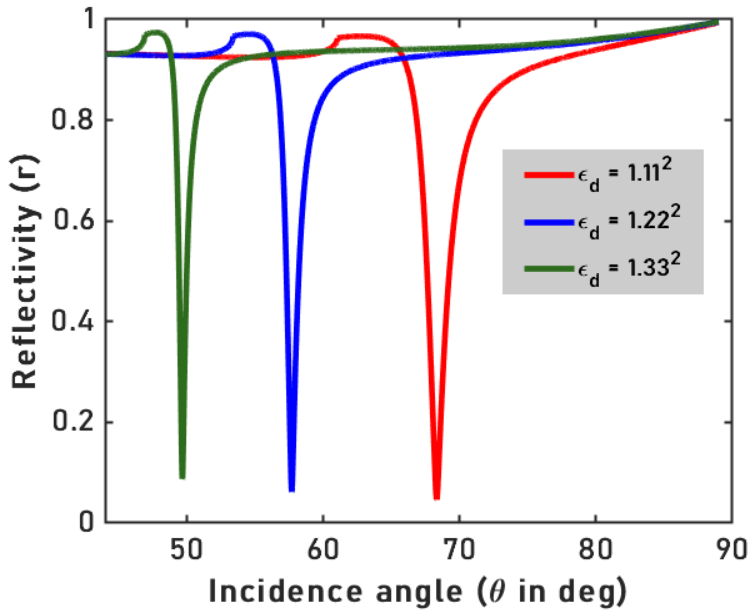

FIGURE 2.14: Shift in the dips in reflected signal due to excitation of SPs in an SPR sensor with changes in the permittivity of the surrounding to be sensed.

concentrations. For example, hybrid structures consisting of multiple metal layers or nearly guided wave configurations have been employed to enhance sensitivity [54]. Multilayered structures can also be used to excite LRSPPs that have higher sensitivity and lower attenuation than SPPs [55]. Several emerging materials have also been explored to serve as the SPR sensing layers, which is a key factor governing the selectivity and resolution of the sensors [56]. Some of these materials include novel nanostructures, polymeric materials, and biomaterials [57]. In addition, external labels composed of high-index materials such as gold nanoparticles have been used to amplify the SPR response [58]. Parallel to these experimental techniques, a more detailed study of plasmonic geometries using analytical models can quantify the light-matter interactions offering better insights. This will not only improve the current generation of sensors but may also point to alternate candidates demonstrating better sensing capabilities.

Optical Trapping

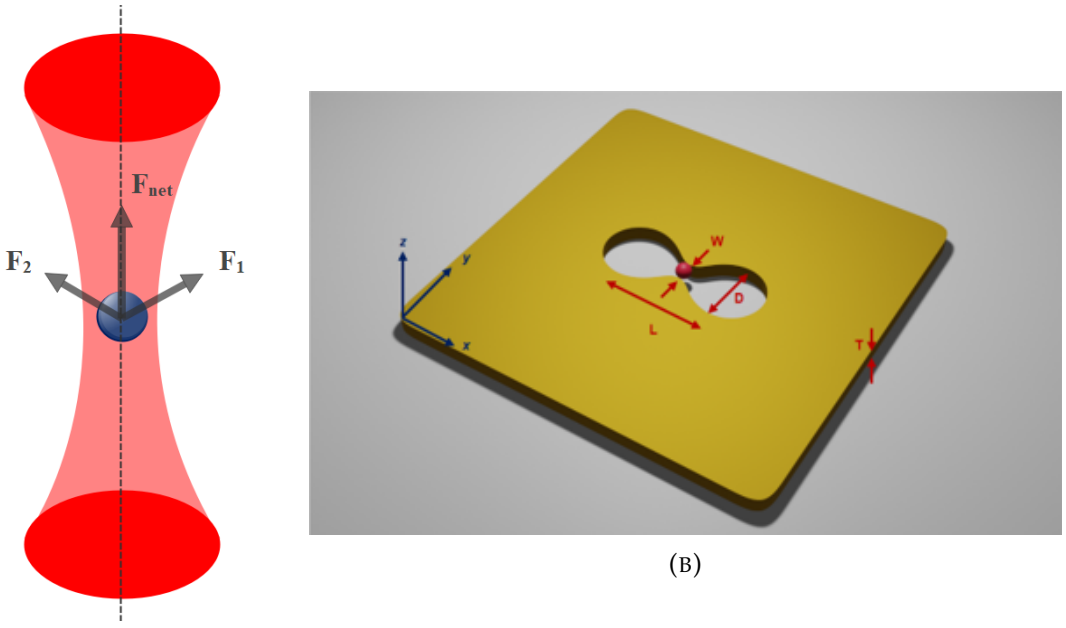

(A) (B)

FIGURE 2.15: (A) The gradient forces acting on a particle at the center of a focused laser beam (B) A schematic of a double nanohole aperture used to enhance light-matter interactions in an optical trap.

In 1970 Arthur Ashkin and his colleagues demonstrated that a focused laser beam can be used to hold onto microscopic particles in three dimensions [59]. Optical traps since then have been used to trap, manipulate, and observe the dynamics of several nanoscale objects, which guaranteed the discovery of a Nobel Prize in Physics in 2018. When a laser beam is focused into a tight spot, the gradient forces form a potential well capable of capturing particles in the vicinity of the focus. However, the diffraction limit restricts the confinement to be in the order of the wavelength of light, limiting the size of the particles that can be trapped and the precision of the trapping [60].

Nanostructures in metals sustain surface plasmons, which are not restrained by the classical diffraction limit [1]. A series of metal-dielectric structures in different configurations have been used to generate highly confined electromagnetic

fields enabling the stable trapping of particles significantly smaller than the wavelength of light [61]–[63]. Optical tweezers based on nanoapertures also exhibit a mechanism called self-induced back action (SIBA), where the particle to be trapped creates favorable conditions for its own trapping by strongly perturbing the local electromagnetic fields [64]. Consequently, nanoaperture-assisted optical trapping has been highly successful in the trapping and characterization of a wide range of nanoscale objects like single proteins, DNA, and viruses [65]–[67].

Some of these apertures like the double nanohole (DNH) shown in Figure 2.15b have been theoretically studied by our group [68]. Analytical theories similar to the models presented in this thesis can be extended to other nanoapertures geometries to gain a deeper understanding of the modes supported by them, their propagation, transmission, and their cut-off characteristics. This will allow the design of plasmonic geometries tailored to trap and characterize the interactions of nano-sized particles by more careful consideration of experimental conditions specific to the particle itself.

Information Processing

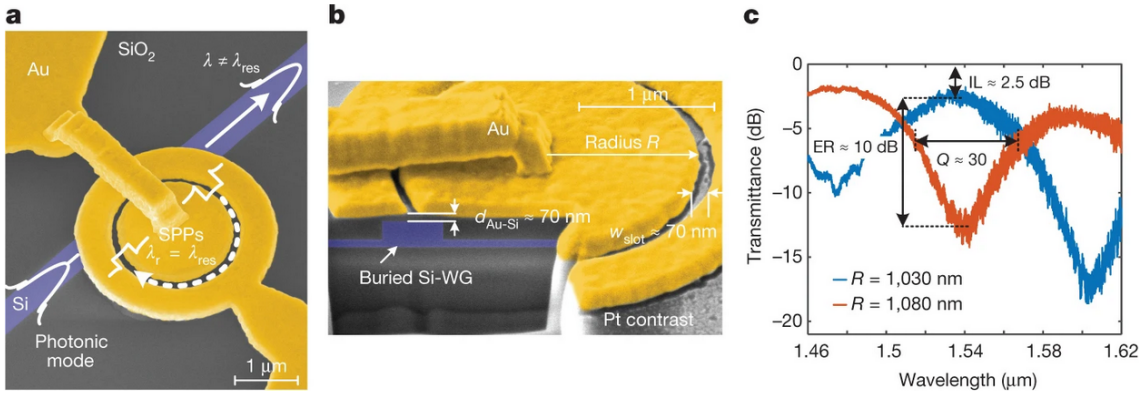

FIGURE 2.16: (A) The top view and (B) the cross-section view of a MIM-based ring-resonator coupled to Si waveguide in an electro-optic modulator. (C) The transmission characteristics of two MIM ring resonators. Adapted from Haffner, C. *et. al* with permission [69].

The information processing field is constantly challenged by the need for miniaturization and the ever-growing demand for higher bandwidth. Plasmonics offers the platform to address both as it combines the subwavelength operation of electronics with the high-speed operation of photonics [22]. Plasmonic components have been implemented in wide-ranging information processing applications including emitters, detectors, electro-optic modulation, rf-to-fiber conversion, multiplexers, switches, encoders etc.

In 2015, C. Haffner *et al.* engineered an all-plasmonic Mach–Zehnder modulator two orders of magnitude smaller than state-of-the-art photonic modulators available at that time. It demonstrated an extremely low energy consumption of 25 fJ/bit even at the highest speed of operation [3]. In 2017, M. Ayata *et al.* developed an all-plasmonic ultra-compact electro-optic modulator with speeds up to 116 Gbits/s in a single metal layer [70]. In 2020, U. Koch *et al.* demonstrated a transmitter with data rates beyond 100 GBd in a plasmonic platform co-integrating CMOS electronics and Si-photonics [5].

Despite the several record-breaking achievements of plasmonics in this field, their practical implementation still poses challenges. They suffer from losses that increase with increased confinement of the electromagnetic fields, implying that the higher spatial localization of modes results in shorter propagation lengths. Therefore, optimizing the plasmonic geometry becomes essential to mitigate this challenge. Analytical models provide means to study the properties of these geometries in greater detail by offering insights into the physics of mode interactions. In addition, they are considerably faster than numerical methods and can be employed for rapid design optimization. Over the next chapters, analytical models for subwavelength slits in metals and plasmonic slot waveguides are presented and discussed in detail.

Chapter 3

Analysis of a Subwavelength Slit in Metal

In this chapter, we discuss the contributions of the author on the analysis of a slit in a real metal [28]. It covers a purely analytical model for transmission and reflection in metallic slits based on single-mode matching to continuum and the Fabry-Pérot model. Existing theoretical concepts that were key in deriving the equations for the slit are discussed first. A brief overview of the approximations used in the theory is given, slit equations are derived, and the results obtained from the theory are presented and discussed.

3.1 Introduction to Slits in Metals

Slits in a metal provide extreme subwavelength confinement of light [71]–[77]. It has found them many applications including spectroscopy [78]–[80], nonlinear optics [81]–[83], optical tweezers [64], [65], [84], and sensors [85]–[89]. In addition, the metal layers also serve as contacts that can be used in optoelectronic applications like modulators [3], [4], [69], [70].

One of the major challenges in the implementation of plasmonic geometries is the trade-off between field confinement and propagation length. In slits, with

narrowing gaps the confinement of the mode and the field enhancement increase exponentially. With higher confinement, however, the penetration of the electric field into the metal increases leading to higher amounts of absorption and shorter propagation length of the mode.

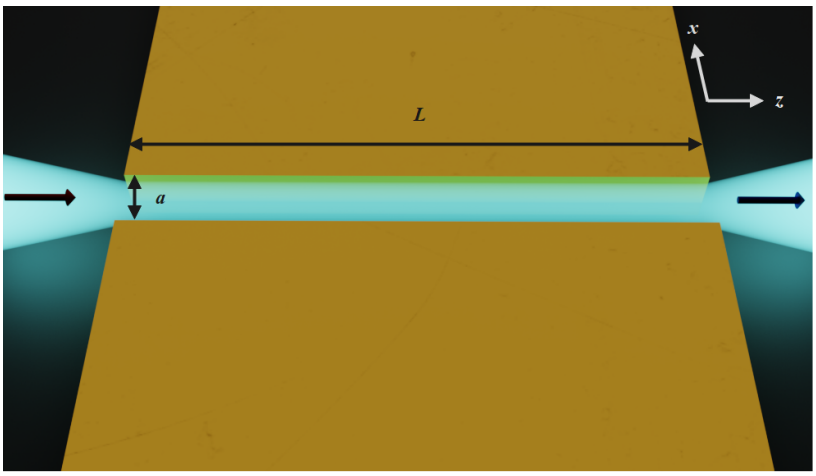

FIGURE 3.1: Schematic of an Au slit of permittivity ϵ_m filled with a dielectric medium of permittivity ϵ_{d1} and surrounded by a dielectric of permittivity ϵ_{d2}. The width of the slit is a and the length or metal thickness is L, the metal extends semi-infinitely in the x-direction and infinitely in the y-direction.

Power through the slit can be considered as a metric to balance the field enhancement and absorption. In recent years, others have explored the maximum power transfer theorem for plasmonic nanostructures, but the analysis was focused on nanoantennas [90]. With numerous prospective applications of slits in sight and a growing focus on miniaturization across many of them, there is a need for optimization of slit geometry based on requirements.

Numerical simulations are the most commonly used approach in plasmonic design, which is akin to doing experiments on a computer. The simulations are expected to run for a long time for high-quality resonances. Typical time-domain runs last several hours in our experience. In addition, a new simulation is required for any change in source or structural parameters. While 2D simulations typically

take less time than 3D simulations, narrow slits can be challenging for time-domain approaches because the grid size needs to be small to accurately capture the rapid field decay as well as the time step to satisfy Courant stability with small grids.

An analytical model is therefore important for simplifying the design process and gaining insights into the physics underlying the observed behavior of light in slits. In the presented framework, we derived a purely analytical equation for the reflection coefficient at the slit's interface with surrounding dielectrics. The derived equation removed the need for any numerical methods including numerical integration. The Fabry-Pérot formalism was then used to obtain expressions for field enhancement, power through the slit, and scattering and absorption cross-sections, which are key metrics for quantifying light-matter interactions. The theory also allowed us to establish a condition for maximum power transfer through the slit.

The schematic of the slit geometry is shown in Figure 3.1. Two semi-infinite metal films of thickness l and permittivity values ϵ_m, taken from existing literature [42] are separated by a distance a in the x-direction. The slit is filled with a dielectric of permittivity ϵ_{d1} and surrounded by another dielectric of permittivity ϵ_{d2}. In the subwavelength regime ($a \ll \lambda$), it is a good approximation to assume that only one mode can be localized in the x-direction. x-polarized plane waves are incident on the slit. As has been stated before, the majority of the power resides in the gap and is contributed by the transverse electric (E_x) field, therefore the TM mode in a MIM structure is considered to be a quasi-TEM mode.

3.2 Reflection Coefficient in a Metallic Slit

Reflection is a crucial component of propagation in any plasmonic geometry. The simplicity of slit geometry has attracted several theoretical studies over the last two decades, both numerical and analytic. With this work, we aimed to provide

researchers with a way to calculate the reflection without requiring any numerical tools. In order to achieve this, we used two approximations that are the basis of our model: constant field approximation and dielectric loading.

3.2.1 Constant Field Approximation and Dielectric Loading

Under the constant field approximation also known as the PEC approximation, it is assumed that the field inside the slit is constant. Additionally, there is no field penetration into the metal. The approximation is validated by two observations. First, at the long wavelengths where plasmonic nanostructures are typically employed, metals have very high permittivity *i. e.* $|\epsilon_m| \gg \epsilon_{d1/2}$. The continuity of the normal electric displacement fields across the two $y-z$ planes allows for the ratio of the normal electric fields (E_x) in the slit and metal to be expressed as ϵ_m/ϵ_{d2}. Therefore, the field in the metal is significantly lower than the field in the gap and can be altogether neglected. Secondly, in the limit, $a \ll \lambda$, the cosine hyperbolic dependence of E_x on x becomes almost constant. The field in the overall geometry is represented by a rectangle function with unit amplitude for $x \leq |a|/2$ and 0 otherwise, as shown in Figure 3.2.

Dielectric loading was introduced to our framework as a means of accommodating the finite conductivity of real metal and the associated absorption. In this method, the gap in the slit is replaced by a material of complex refractive index (n_{MIM}). n_{MIM} is the effective index of a mode in MIM geometry given as k_z/k_0. k_z is the propagation constant of the MIM geometry, which was derived in the previous section. For a slit of gap width a, it can be rewritten as:

$$\tanh\left[\sqrt{k_z^2-\epsilon_d {k_0}^2}\frac{a}{2}\right] = \frac{-\epsilon_d\sqrt{k_z^2-\epsilon_m {k_0}^2}}{\epsilon_m\sqrt{k_z^2-\epsilon_d {k_0}^2}} \tag{3.1}$$

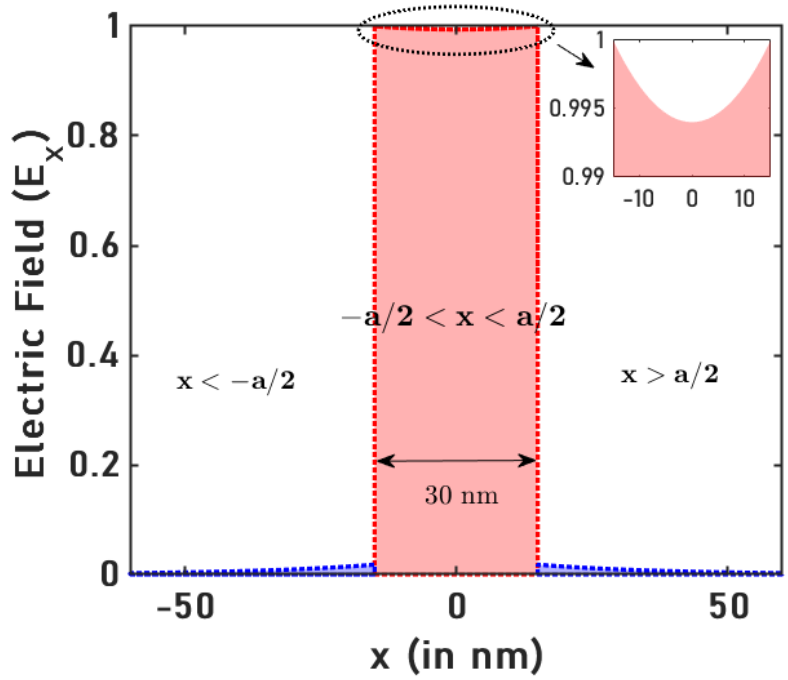

(A)

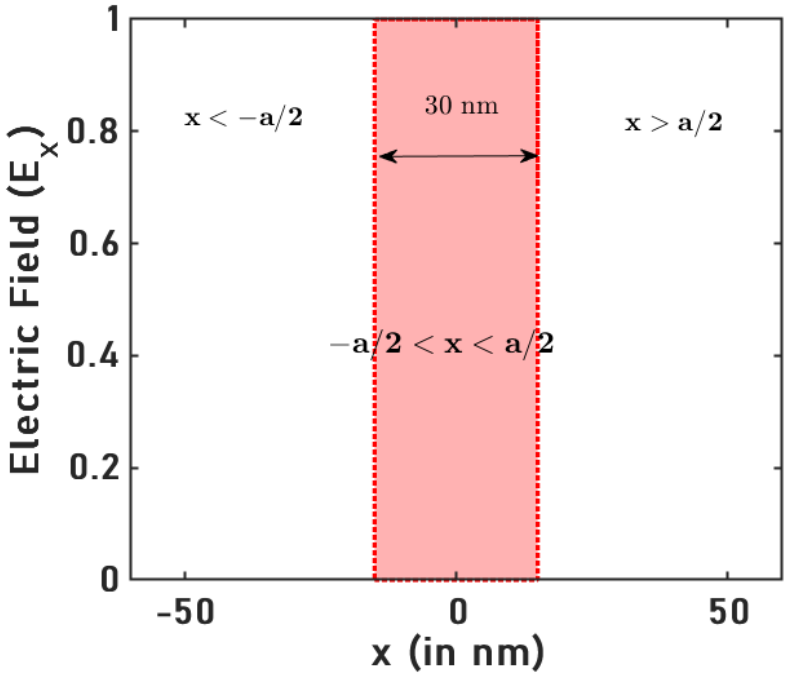

(B)

FIGURE 3.2: (A) The exact values of E_x (normalized to its maximum value) inside and outside a slit (MIM geometry) of width 30 nm at a wavelength of 1550 nm (B) E_x approximated by a rectangle function of amplitude 1 for the analysis presented here. Adapted from Pati, A. *et. al* with permission [27].

3.2.2 Single-Mode Matching to Continuum

Mode-matching is a rigorous and versatile modal analysis technique, typically used to characterize discontinuities in waveguides such as a transition from one medium to another. In single-mode matching to continuum (SMM), the transverse electric and magnetic fields of the single mode inside the slit are matched with the transverse fields of the continuum of modes outside the slit. The modes outside the slit account for all possible evanescent modes existing at the metal-dielectric interface. The overlap integrals resulting from the matched fields are solved by using the orthogonality of modes. It has been previously shown by our group that conjugated orthogonality of modes returns non-zero values. Therefore, unconjugated orthogonality is used to obtain accurate values of reflection.

The reflection and transmission coefficients in the slit are shown in Figure 3.3. The reflection coefficient ($r_{21} = r$) for a slit completely surrounded by air ($\epsilon_{d1} = \epsilon_{d2} = 1$) at the interface $z = 0$ is calculated by SMM. The transverse electric field inside the slit s given as:

$$E_x(z = 0^-) = (1 + r)\ \text{rect}\left(\frac{x}{a}\right) \tag{3.2}$$

$\text{rect}\left(\frac{x}{a}\right)$ is the rectangle function described in Section 3.2.1. E_x just outside the slit is given as:

$$E_x(z = 0^+) = \int_{-\infty}^{\infty} t(k_x) \exp\left(ik_x.x\right)\, dk_x \tag{3.3}$$

$t(k_x)$ is the transmission coefficient at the interface. The integral sums up all possible evanescent modes in the free space. Similarly, the magnetic fields in the slit and outside it are given as:

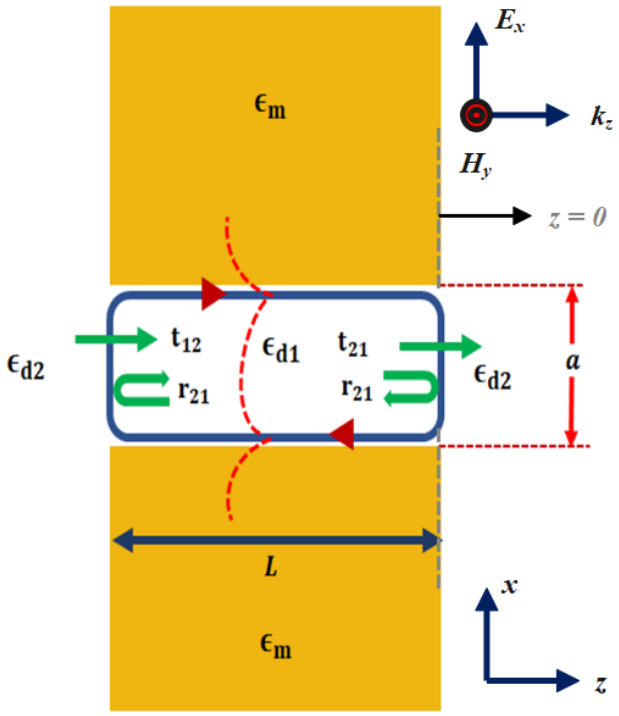

FIGURE 3.3: x-z view of the Au slit of permittivity ϵ_m, filled with dielectric of permittivity ϵ_{d1} and surrounded by a different dielectric of permittivity, ϵ_{d2}. Electric field (E_x) is along the x-direction and magnetic field (H_y) along the y-direction.

$$H_y(z = 0^-) = (1 - r)\frac{\omega}{k_0}\text{rect}\left(\frac{x}{a}\right) \tag{3.4}$$

$$H_y(z = 0^+) = \frac{\omega}{\sqrt{k_0^2 - k_x^2}}\int_{-\infty}^{\infty} t(k_x)\exp\left(ik_x.x\right)dk_x \tag{3.5}$$

The orthogonality of modes condition for the freespace modes and slot mode is used to solve the overlap integrals resulting from the matched fields. By multiplying $\exp\left(ik'_x.x\right)$ to Eqs. 3.2 and 3.3 and integrating over x from $-\infty$ to ∞, the relationship between $t(k_x)$ and r is obtained as follows:

$$t(u) = \frac{1}{2\pi} \frac{(1+r)\lambda \sin\left(\frac{\pi a u}{\lambda}\right)}{\pi u} \tag{3.6}$$

$u = k_x/k_0$. For the second orthogonality condition, rect $\left(\frac{x}{a}\right)$ is multiplied to Eqs. 3.4 and 3.5 and integrated over x from $-\infty$ to ∞ to obtain r as:

$$\mathbf{r} = \frac{1-I}{1+I} \tag{3.7}$$

where I is given as:

$$I = \int_{-\infty}^{\infty} \frac{\sin^2(\pi w u)}{w\pi^2 u^2 \sqrt{1-u^2}} \tag{3.8}$$

Where, $w = a/\lambda$. Based on integrals performed in existing works [14], an analytic equation is obtained for Eq. 3.8 as follows:

$$I = \pi w + \mathrm{i}2w \left[\log(2\pi w) - \frac{3}{2}\right] \tag{3.9}$$

Dielectric loading is introduced at this stage to transition from a PEC to a real metal by replacing λ with the effective wavelength ($\lambda_{\text{eff}} = \lambda/n_{\text{MIM}}$) in the metallic slit. The new equation for I now becomes:

$$I = \frac{\pi a}{\lambda_{\text{eff}}} + \frac{2a\mathrm{i}}{\lambda_{\text{eff}}} \left[\log\left(\frac{2\pi a}{\lambda_{\text{eff}}}\right) - \frac{3}{2}\right] \tag{3.10}$$

Figure 3.4a shows the reflection amplitude of a slit in gold, completely surrounded by air for different gap widths. The reflection amplitude increases with narrowing slit widths due to increased penetration of the electric field into the metal. Figure 3.4b shows the variation of the reflection phase with the wavelength for the same slit configurations. The reflection phase decreases with narrowing gaps of the slit and increasing wavelength. It is validated against our existing work

that calculates the coefficients by taking the actual electric and magnetic fields inside and outside a real metallic slit into consideration [91].

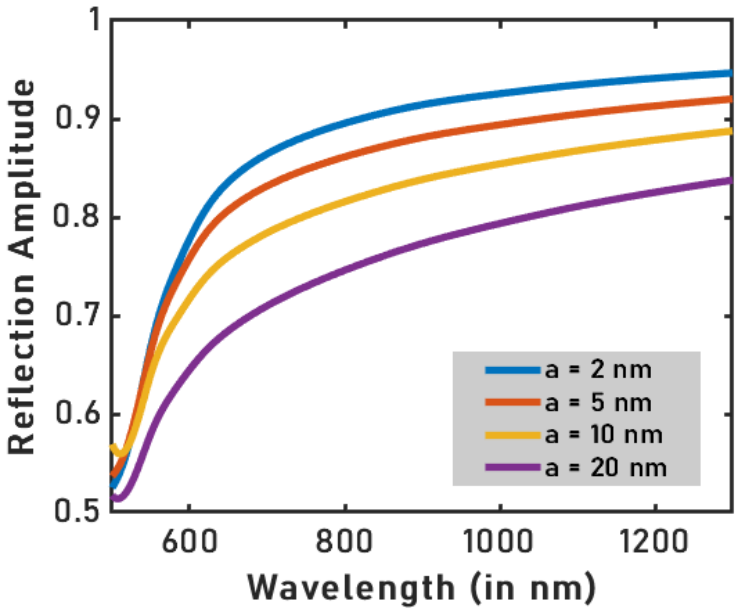

(A)

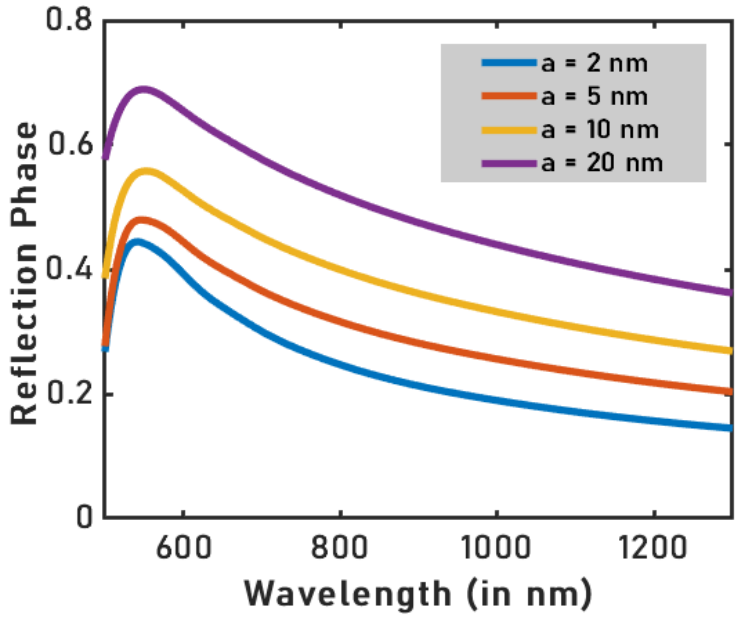

(B)

FIGURE 3.4: (A) Reflection amplitude and (B) Reflection phase in a gold slit of widths 2 nm, 5 nm, 10 nm, and 20 nm, completely surrounded by air *i. e.* $\epsilon_{d1} = \epsilon_{d2} = 1$ [28]

Compared to that past work, the need for numerical calculation of the index has been removed by invoking the effective index approximation. The varying refractive indices of different layers inside the slit are replaced by a constant effective index (n_{MIM}). This approximation is most accurate when the field is almost constant and confined to the slit region, which is applicable for many practical cases (particularly in the infrared). Comparison with our past work demonstrates good agreement for wavelengths between 700 nm to 1300 nm, to within 0.06 rad for 5 nm and 0.15 rad for 20 nm. A minima-like feature observed at the lower end of the wavelength range is the result of absorption in gold. As mentioned in Chapter 2, the absorption peak of gold lies in the visible blue light region, and the increased material absorption reduces the reflection amplitude at shorter wavelengths.

For shorter wavelengths, the theoretical values are not as well matched with the numerical simulation results due to the penetration of the electric field into the metal when the frequency of electromagnetic radiation approaches the plasma frequency. In this regime, the metal no longer acts as a perfect electric conductor, which undermines our assumption of a constant field in the slit region. The resonant wavelength of the slit is highly dependent on this variation of the reflection phase which will become apparent in the subsequent sections.

3.2.3 Optical Cross-sections: Scattering and Absorption

When a nanoparticle is exposed to an external electric field, the field polarizes the particle causing oscillation of charges. The accelerated charges re-radiate electromagnetic fields in a process known as scattering [33]. A subwavelength scatterer is therefore considered to be a Hertzian dipole in the far field and can be approximated by a small current source in the near field. A portion of the electromagnetic energy received by the particle is converted into thermal energy, which is known

as absorption [33]. Scattering and absorption cross-sections are key parameters for characterizing the effective coupling of electromagnetic waves with a nanoparticle. The scattering cross-section is the effective area of a scatterer. The total power scattered by a particle is directly proportional to the product of the scattering cross-section (σ_s) and the intensity of the incident radiation. Similarly, absorption cross-section (σ_a) gives the measure of the amount of incident radiation absorbed by the particle.

3.2.4 The Single Channel Limit

The fundamental limit on the maximum absolute scattering cross-section of a single subwavelength scatterer in a homogeneous medium is known as the single channel limit [92]. It has been rigorously proven that the single channel limit of a 2D scatterer in a medium of refractive index n is $2\lambda/n\pi$ [93]–[95] and $3\lambda^2/2n\pi$ for a 3D scatterer [96]–[98]. In this work, we used the **Fabry-Pérot model** to determine the scattering and absorption cross-section of 2D slits and establish how the relationship between the two influences the power through the subwavelength slit [28]. The Fabry-Pérot model is explained in more detail in the next section.

There have been growing efforts towards enhancing the scattering cross-section of nanoparticles to overcome the single channel limit. Different types of approaches adopted to achieve this include overlapping the peaks of scattering from multiple channels often referred to as superscattering [21], [94], [95]. A second category involves the use of epsilon-near-zero (ENZ) materials to reduce the value of n [99], [100]. More recently, the addition of gain media to 2D resonators has demonstrated a several-fold increase in the scattering cross-section over the single channel limit [101].

3.2.5 Fabry-Pérot Transmission Model

Takakura theoretically investigated a single subwavelength slit in PEC and found that the transmission through the slit resembles Fabry-Pérot modes [11]. It was attributed to the constructive interference of propagating surface plasmons between the two ends of the slit. The theoretical predictions were experimentally confirmed by Yang and Sambles in the microwave regime where the metal behaves like a PEC [71]. Since then the Fabry-Pérot interpretation of slits has been used to explain the extraordinary transmission and absorption in metallic nanoapertures among several other analyses [13], [14], [102]–[104].

A Fabry-Pérot interferometer typically consists of an optical cavity with two highly reflecting mirrors at the ends. The mirrors reflect most of the electromagnetic energy back into the cavity. The multiply reflected modes constructively interfere with each other to generate transmission peaks resulting in several orders of magnitude enhancement of the original incident field. The circulation of the reflected fields inside the slit is shown by the blue loop in Figure 3.3. The total transmitted field in the Fabry-Pérot model is expressed as follows:

$$E_t = t_1 t_2 \exp(ik_z l)[1 + r_1 r_2 \exp(i2k_z l) + (r_1 r_2 \exp(i2k_z l))^2 + (r_1 r_2 \exp(i2k_z l))^4 + ...]E_i \tag{3.11}$$

E_i is the incident field, E_t is the transmitted field, r_1 and r_2 reflection coefficients at the two ends of the cavity, t_1 and t_2 are the transmission coefficients. Eq. 3.11 is the sum of an infinite geometric series and can be further simplified as:

$$E_t = \frac{t_1 t_2 \exp(ik_z l)}{1 - r_1 r_2 \exp(i2k_z l)} E_i \tag{3.12}$$

For our case of 2D metallic slits, the reflection and transmission coefficients are defined as follows:

1. $\mathbf{r_1} = \mathbf{r_2} = \mathbf{r_{21}} = \mathbf{r} = |\mathbf{r}| \exp i\phi$: The reflection coefficient for reflection from the slit back into the slit, calculated using Eq. 3.10.

2. $\mathbf{t_1} = \mathbf{t_{12}} = \sqrt{\mathbf{1} - |\mathbf{r}|^{\mathbf{2}}}$: The transmission coefficient for transmission from free space into the slit.

3. $\mathbf{t_2} = \mathbf{t_{21}} = \mathbf{1} + \mathbf{r}$: The transmission coefficient for transmission from inside the slit into free space.

The transmittance in the slit is therefore written as:

$$T = \frac{|t_{12}|^2 |t_{21}|^2 \exp\left(-\phi_L\right)}{1 + |r_{21}|^4 \exp\left(-2\phi_L\right) - 2|r_{21}|^2 \cos(\delta) \exp\left(-\phi_L\right)} \tag{3.13}$$

where, $\delta = 2k_z^{'}L + 2\phi$, $\phi_L = 2k_z^{''}L$, and ϕ is the reflection phase. The transmittance is multiplied by the width of the slit to obtain the transmission cross-section, which attains its peak for $\delta = 2\pi$. The symmetry of the slit about the x-axis results in equal amounts of forward and backward scattering, so the scattering cross-section (the sum of both) is twice the transmission cross-section. The absorption cross-section is calculated from the scattering matrix, the scattering parameters are used to determine the absorbed power and field intensity and the ratio of both gives us the following equation [105], [106]:

$$\sigma_a = \sigma_t \frac{(1 - \exp(-\phi_L))(1 + |r_{21}|^2 \exp(-\phi_L))}{1 + |r_{21}|^4 \exp(-2\phi_L) - 2|r_{21}|^2 \cos(\delta) \exp(-\phi_L)} \tag{3.14}$$

The constant field approximation allowed us to calculate the power in the slit directly from the field intensity, and the variation of both with the gap width will be shown. For a PEC slit where there is no absorption, the scattering cross-section

reaches the single channel limit at resonance. As suggested before, the single channel limit for 2D scatterers is $2\lambda/\pi$ in air and the scattering coefficient is bounded by $2\lambda/\pi a$.

Figure 3.5b shows the scattering cross-section of a PEC slit plotted against its length for three different slit widths, at a fixed wavelength of 1550 nm. This is obtained by setting the imaginary part of the propagation constant to zero ($k_z'' = 0$). The values of the reflection coefficient used in this analysis are calculated from Equation 3.13. At resonance, it approaches the single channel limit, which is calculated to be 0.987 μm. Although all three configurations scatter light at the single channel limit, the narrower slits are seen exhibiting sharper resonance peaks. The transmission through the slit at resonance is $\lambda/(\pi a)$, which implies that in the absence of absorption, the narrowest slit before the onset of tunneling allows the maximum amount of transmission. But this changes significantly when losses are considered. Figure 3.5a shows the result for 890 nm, with 4 nm, 10 nm, and 20 nm slit widths, to be comparable with later optimal resonance conditions. We observe multiple resonances for the three configurations, each approaching the single channel limit (0.567 μm).

The subsequent analysis focused on the real metal slit. Here, we use a 100 nm long slit with widths ranging from 1 nm to 20 nm and the wavelength of the incident radiation varies between 500 nm and 1650 nm. The values of reflection coefficients were obtained from Eq. 3.9.

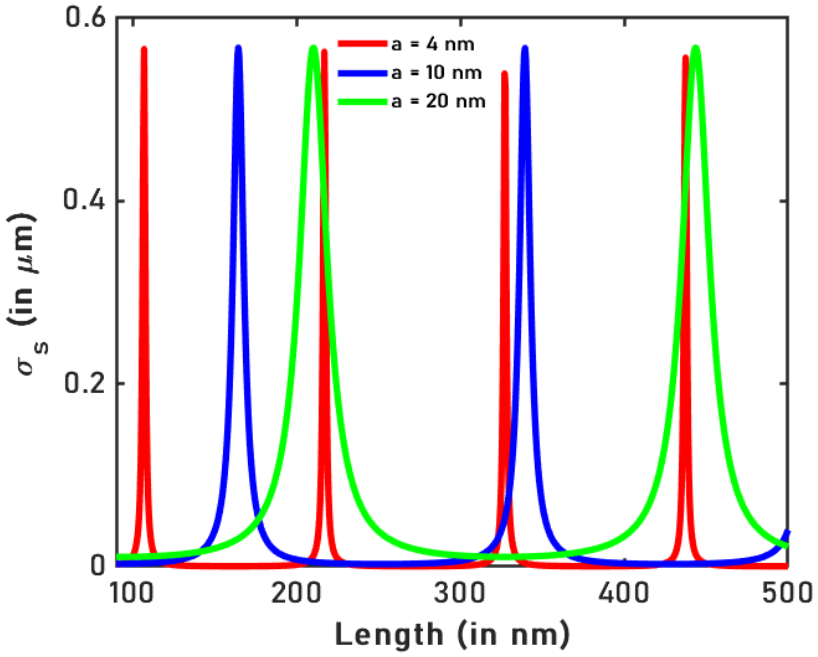

(A)

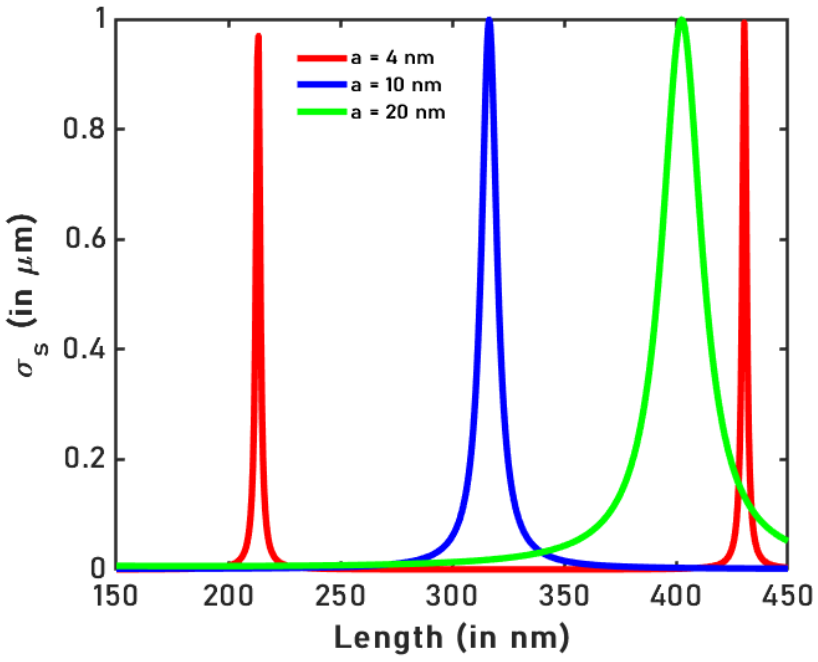

(B)

FIGURE 3.5: (A) Scattering cross-section (σ_s) of PEC slits of widths 4 nm, 10 nm, and 20 nm for wavelength of 1550 nm, (B) σ_s for widths of 4 nm, 10 nm, and 20 nm for wavelength of 892 nm calculated from Eq. 3.13 after setting the absorption to zero ($k_z'' = 0$). σ_s approaches the single channel limit ($2\lambda/\pi$) at the resonance condition for each configuratio. [28]

.

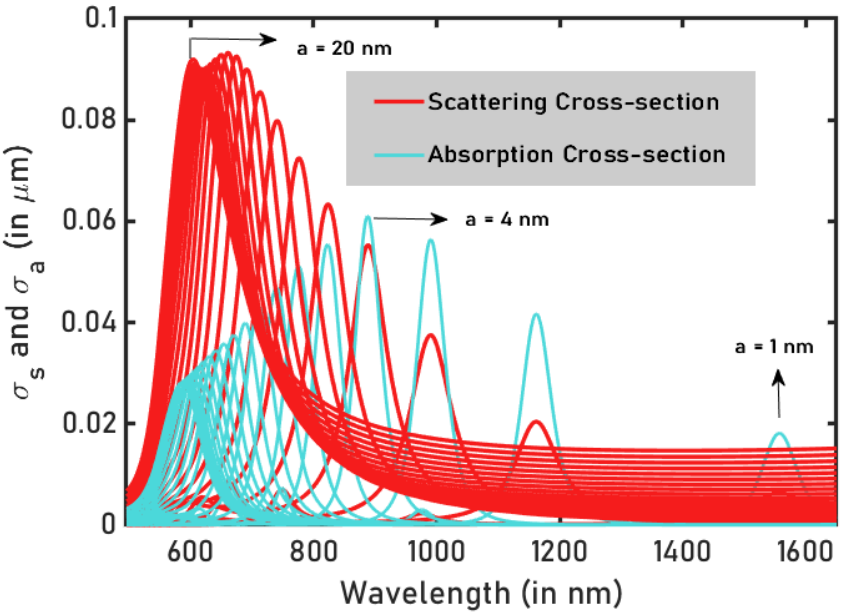

(A)

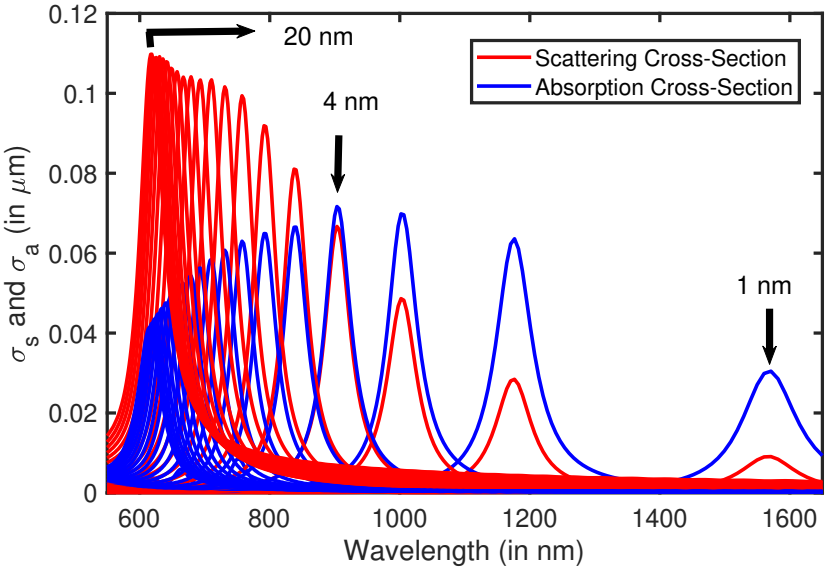

(B)

FIGURE 3.6: (A) Scattering cross-section (σ_s) (B) absorption cross-section (σ_a) for gap widths ranging from 1 nm to 20 nm, calculated analytically using Eqs. 3.13 and 3.14. Red lines represent σ_s and blue lines represent σ_a. (B) σ_s and σ_a obtained from Lumerical FDTD simulations. Adapted from Pati, A. *et. al* with permission [28].

The losses are a result of the absorption of electromagnetic waves into the metal

as they propagate back and forth inside the slit. They are taken into account by considering the non-zero imaginary part of the propagation constant (k_z'') in the Fabry-Pérot formalism. The propagation lengths range from 9 nm for a 1 nm wide slit at 1650 nm to 778 nm for a 20 nm wide slit at 550 nm and the corresponding absorption cross-sections are calculated from Eq. 3.14.

Figure 3.6a shows variation of scattering and absorption cross-sections, calculated from Eqs. 3.13 and 3.14. The resonant peaks are red-shifted when the slit width is reduced due to an increase in the effective index of the TM mode inside the slit. The higher values of the effective index are a result of larger penetration of the EM-fields into the metal, which also causes increased Ohmic losses [107]. The scattering cross section at long wavelengths rises slightly. This is because the phase of propagation is getting smaller, as is the phase of reflection, so it is closer to a zeroth order resonance condition. The absorption cross-section is maximized at the resonance of a 4 nm gap, where it becomes comparable to the scattering cross-section.

3.2.6 Numerical Simulations: Finite-Difference Time-Domain

Finite-difference time-domain (FDTD) is a rigorous, numerical technique to solve Maxwell's equations. It was first proposed by Kane Yee in 1966 [108]. The method approximates the spatial and temporal derivatives in Maxwell's equations by finite differences. The discretization of space and time is performed to arrive at iterative finite-difference equations for the electromagnetic fields. The electric and magnetic fields in any given time step are determined in terms of field values in the previous step and the sequence is repeated for the desired length of time.

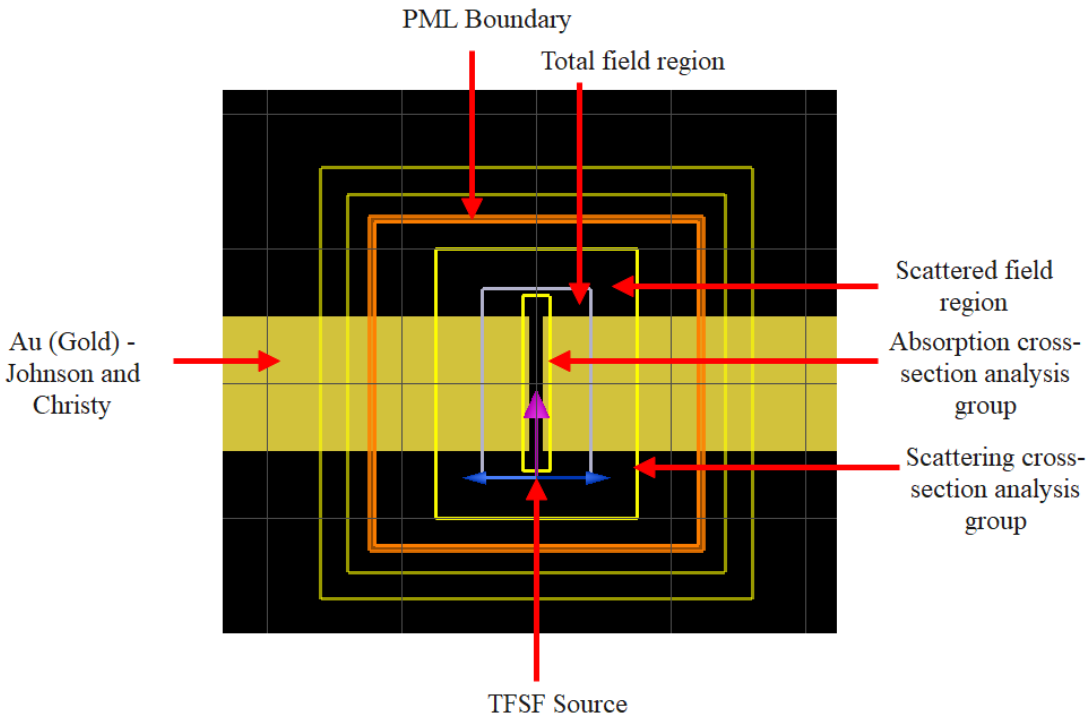

FIGURE 3.7: Schematic of the simulation region containing the gold slit in the PML boundary, TFSF source, and the two monitors (in the analysis groups) for capturing the scattering and the absorption cross-sections.

As the slit geometry has translational symmetry along the y-axis, the relevant parameters can be extracted by running 2D simulations considering only the x-z propagation plane. This has the additional benefit of significantly shortening the runtimes compared to 3D simulations. We performed the 2D simulations in ANSYS Lumerical FDTD v2020 R2.3 within a perfectly matched layer (PML) boundary. The PML boundary is used to terminate the FDTD grids. It is a lossy layer that should ideally absorb all fields, however, reflections may exist in discrete implementation. A mesh size of 0.2 nm was used in both x- and z-directions based on an existing work that analyzed a similar structure [83]. The accuracy of the simulations based on the choice of grid size was later verified by a convergence study. The time step was automatically selected by the FDTD software such that the Courant stability condition is satisfied. The stability condition in 2D can be written as:

$$v_x \frac{\Delta t}{\Delta x} + v_z \frac{\Delta t}{\Delta z} \leq C \tag{3.15}$$

v_x and v_z are the velocity of the EM wave in the x- and z-directions respectively. Δx and Δz are the grid size, Δt is the time-step, and C is the Courant number, which depends upon the type of simulation. When finer spatial meshing is used, the time-step is reduced such that Eq. 3.15 is satisfied. This ensures that for any parameter calculation in two consecutive time steps, the wave also reaches the next grid in space so that the algorithm can form an accurate solution.

A total field scattered field (TFSF) source was used to illuminate the slit. In TFSF, the total simulation region is divided into two regions, the first region contains the incident field and the scattered field *i. e.* the total field whereas the second contains the scattered field only. A frequency-domain power monitor was used to visualize the fields in the region. Two cross-section analysis objects, one in the total field region and the other one in the scattered field were added to measure the absorption and scattering cross-sections. Au (Gold) - Johnson and Christy was picked from the Material Database to form the gold films and a user-defined index of 1.00 was used for air inside and outside the slit. A schematic of the simulation region in Lumerical FDTD software is shown in Figure 3.7. The purple arrow of the TFSF source indicates the direction of propagation and the blue arrows represent the electric field polarization.

Figure 3.6b shows the scattering and absorption cross-sections obtained from our Lumerical FDTD simulations. They match closely with the analytical results, however, the values in the simulations are slightly higher than the theoretical values which are explained in part by the presence of higher-order modes in the simulations and by the finite penetration into the metal (shown in Appendix B).

3.3 Maximum Power Transfer in a Subwavelength Slit

Figure 3.8a shows the peak values of the optical cross-sections. The vertical line indicates that the scattering and the absorption cross-sections become approximately equal at a width of 4 nm. We extended this study to 80 nm and 120 nm long slits which gave us the same results. Additionally, it was observed that longer slits produce equal scattering and absorption cross-sections for wider gaps.

Figure 3.8b shows the variation of the field enhancement and power with the gap width. The electric field varies inversely with the width as narrow slits lead to tighter confinement and greater local density of optical states (LDOS). The power, on the other hand, attains its peak at 4 nm and starts declining if the gap widths are further reduced, which is a manifestation of the maximum power transfer theorem. For the 80 nm and 120 nm long slits, the power inside the slit peak at 3 nm and 5 nm respectively, for equal values of scattering and absorption cross-sections. Numerical simulations were performed for the 100 nm long slit and they matched well with our analytical work (shown in Appendix B).

A lot of research in plasmonics has been directed towards understanding the nonlocal and quantum tunneling effects observable at extremely small length scales as they are seen as the fundamental limits bounding the performance of plasmonic devices [109]–[112]. For instance, in metallic slits, the narrowest gap before the onset of tunneling is considered to be the defining factor of the maximum possible plasmonic enhancement [113]. However, the fact that metallic absorption also tends to increase with narrowing gaps is often overlooked. Losses are paramount for practical devices and here we have shown that the optimal gap width is much larger than the limit set by tunneling or nonlocal effects, which has been noted previously [114].

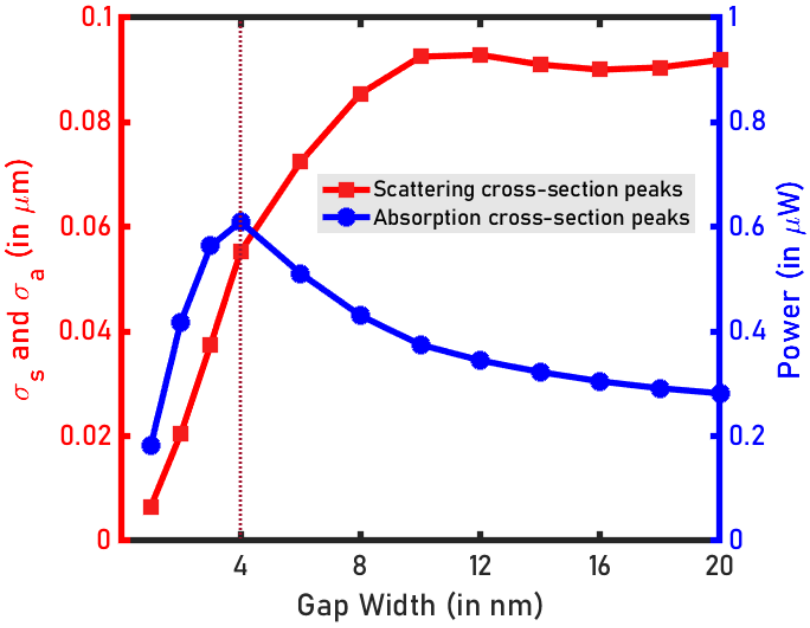

(A)

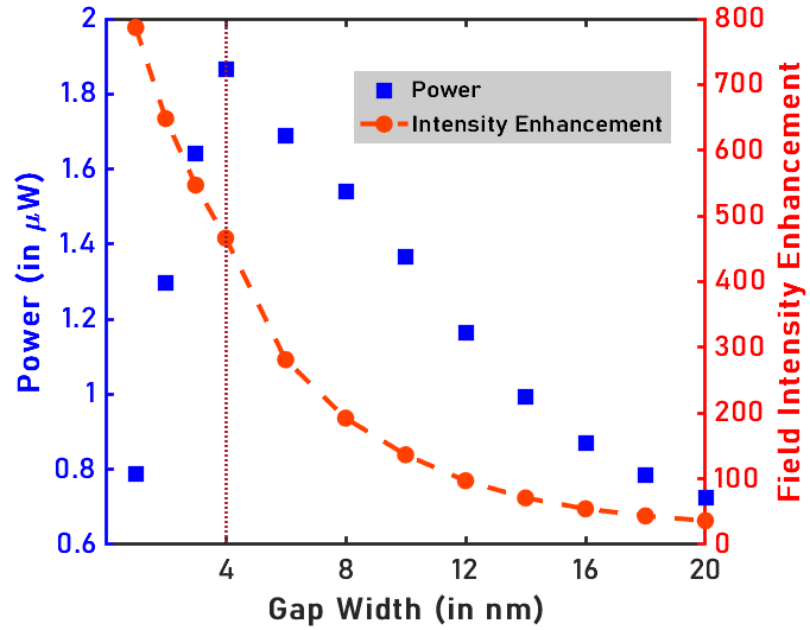

(B)

FIGURE 3.8: (A) The peak values of σ_s (red squares) and σ_a (blue circles) at the resonance condition, are taken from Figure 3.6a. σ_s and σ_a are equal at a gap of around 4 nm. The vertical dashed line indicates the 4 nm mark. (B) Field enhancement (red circles) and power (blue squares) inside a metallic slit, computed analytically using the Fabry-Pérot formalism. The field varies inversely with gap width, power saturates at 4 nm for equal values of σ_s and σ_a at resonance, marked by the vertical dashed line [28].

Chapter 4

Modal Properties in Plasmonic Slot Waveguides

This chapter focuses on the author's contributions towards the analysis of plasmonic slot waveguides [27]. It includes an analytical framework for determining the properties of modes found in plasmonic slot waveguides. First, an equation for the reflection of the gap plasmon mode at the slot's interface was derived. The desired properties were evaluated by using a geometric optics approach. The results of the theory and their comparison with numerical simulation results are presented and discussed.

4.1 Introduction to Plasmonic Slot Waveguides

Plasmonic slot waveguides support extremely localized electromagnetic modes over a wide range of frequencies [16], [17], [115]. They have been applied in high-speed information processing applications [3], [21], [69], [116]–[122], optical tweezers [123], [124], extreme confinement for light-matter interactions, and sensing [125], [126]. As mentioned before, the waveguides sustain modes with long propagation lengths in the optical communication regime [16], [18], allow sharp bending at lower scattering losses compared to dielectric waveguides [19], and are

easy to fabricate. They allow electrical bias fields and optical modes in the same region, which favors integration with existing electronics [20]. The two metal layers provide electrical contacts down to the nanometer scale [127], [128], while their high thermal conductivity facilitates heat removal from the circuitry [114], [122], [129].

Past works used numerical methods to study these geometries and the modes supported by them [16]–[19], [115], [130]. Although accurate, numerical simulations do not provide physical insight and are resource intensive. Analytical models provide physical parameters like reflection phase, which can be used in the accurate design and have been applied to other plasmonic geometries [11], [13], [71], [103], [104], [131]–[143]. An analytic expression of the reflection coefficient at the slot-dielectric interface was derived by combining single-mode matching to a continuum with an approximate mode shape. The reflection phase values obtained from this equation were used in the transverse resonance waveguiding condition in the geometric optics framework to calculate the mode effective index and propagation length. The results were shown to be accurate by numerical simulations performed with commercially available numerical software.

4.2 Reflection in the Plasmonic Slot Waveguide

Figure 4.1a shows a schematic of the slot waveguide geometry under consideration. Two gold films of thickness l and permittivity ϵ_m (values taken from a past work [42]) are separated by a distance of a. They are surrounded by dielectric media of permittivity ϵ_{d1} at the top ($z = l/2$), ϵ_{d2} at the bottom ($z = -l/2$), and ϵ_d inside the slot. The gap plasmon mode in the slot is quasi-TEM (transverse electromagnetic). The transverse electric field along the x-direction is represented by E_x. Propagation takes place in the y-z plane, making an angle θ with the z-axis.

The magnetic field (H), being perpendicular to the propagation direction is also directed in the y (H_y) and z (H_z) directions as shown in Figure 4.1c. When θ exceeds the critical angle (θ_c), the gap plasmon mode propagates by total internal reflection at the slot-dielectric interfaces. The two reflection coefficients r_1 and r_2 are shown in Figure 4.1b. All subsequent calculations were performed at a wavelength (λ) of 1550 nm.

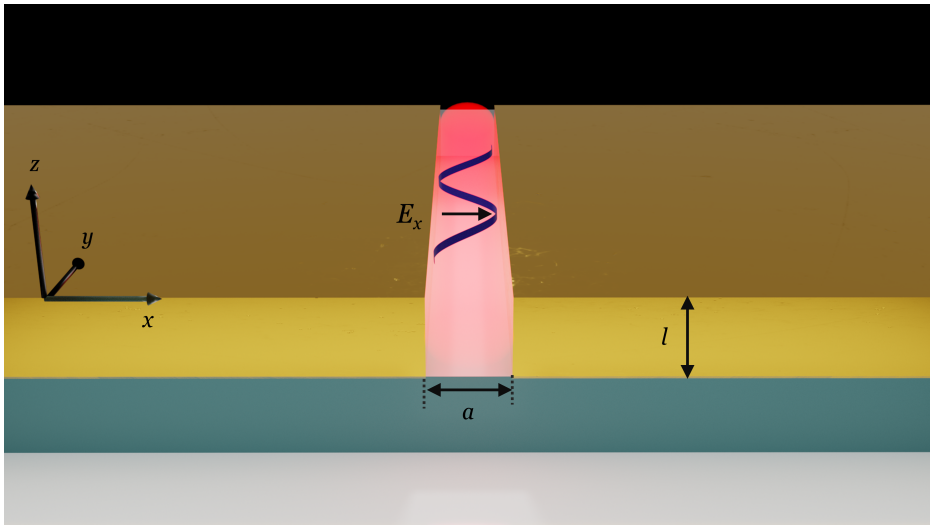

(A)

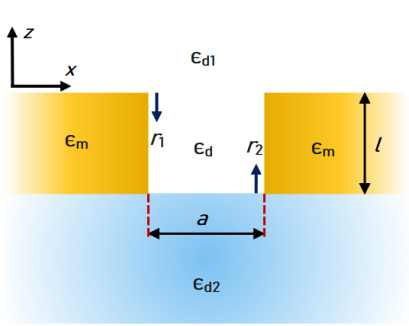

(B)

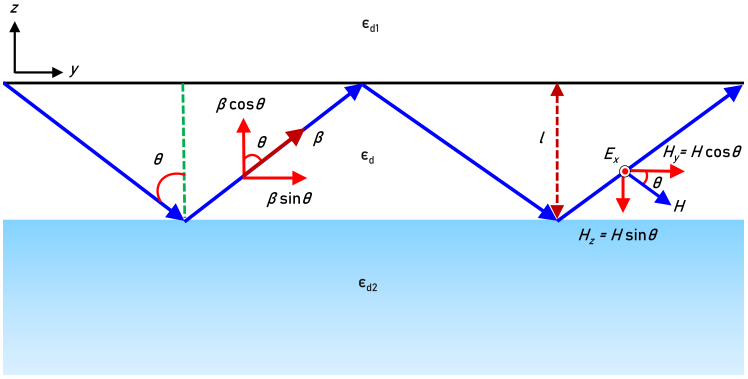

(C)

FIGURE 4.1: (A) Schematics of the 3D plasmonic slot waveguide of width a and metal thickness l surrounded by different dielectric media. (B) x-z view of the waveguide showing the reflection coefficients r_1 and r_2. (C) y-z view of the waveguide, showing the total internal reflection of the gap plasmon mode. Adapted from Pati, A. *et. al* with permission [27].

Similar to our work on slits, the analysis presented here is also based on a combination of PEC approximation and dielectric loading. As mentioned in the previous chapter, metals have high values of permittivities at long wavelengths, leading to very limited penetration of the electric field, which can be ignored with respect to the much higher values of the field in the slot. Secondly, the electric field becomes almost constant in the limit $a \ll \lambda$. Therefore, the total field in the region was approximated by a rectangle function as defined in Chapter 3.

Dielectric loading was introduced as a means of including the finite conductivity and absorption of real metal. The slot was replaced by a material of complex refractive index n_{MIM}, which is the effective index of a gap plasmon mode given by β/k_0. k_0 is the free-space wave vector and β is the propagation constant in a metal-insulator-metal (MIM) structure calculated by solving the dispersion relation given in Eq. 3.1.

4.2.1 Single Mode-Matching to Continuum in a Plasmonic Slot

The single-mode matching to continuum method was used to derive an analytic expression for reflection coefficients, r_1 and r_2. In the subwavelength regime ($a \ll \lambda$), it is a good approximation to assume that only a single mode can be localized in the x-direction inside the slot. The transverse electric and magnetic fields of this mode were matched with the corresponding fields of the continuum of modes outside the slot under PEC approximation.

Considering the interface at the top, the electric field in the slot is given by:

$$E_x(z = 0^-) = (1 + r_1)\mathrm{rect}\left(\frac{x}{a}\right)\exp\left(ik_y.y\right) \tag{4.1}$$

Here, rect(x/a) is the rectangle function whose value is 1 for $-a/2 < x < a/2$ and 0 everywhere else. The electric field just above the slot interface is given as:

$$E_x(z = 0^+) = \int_{-\infty}^{\infty} t(k_x) \exp\left(ik_y.y + ik_x.x\right) dk_x \tag{4.2}$$

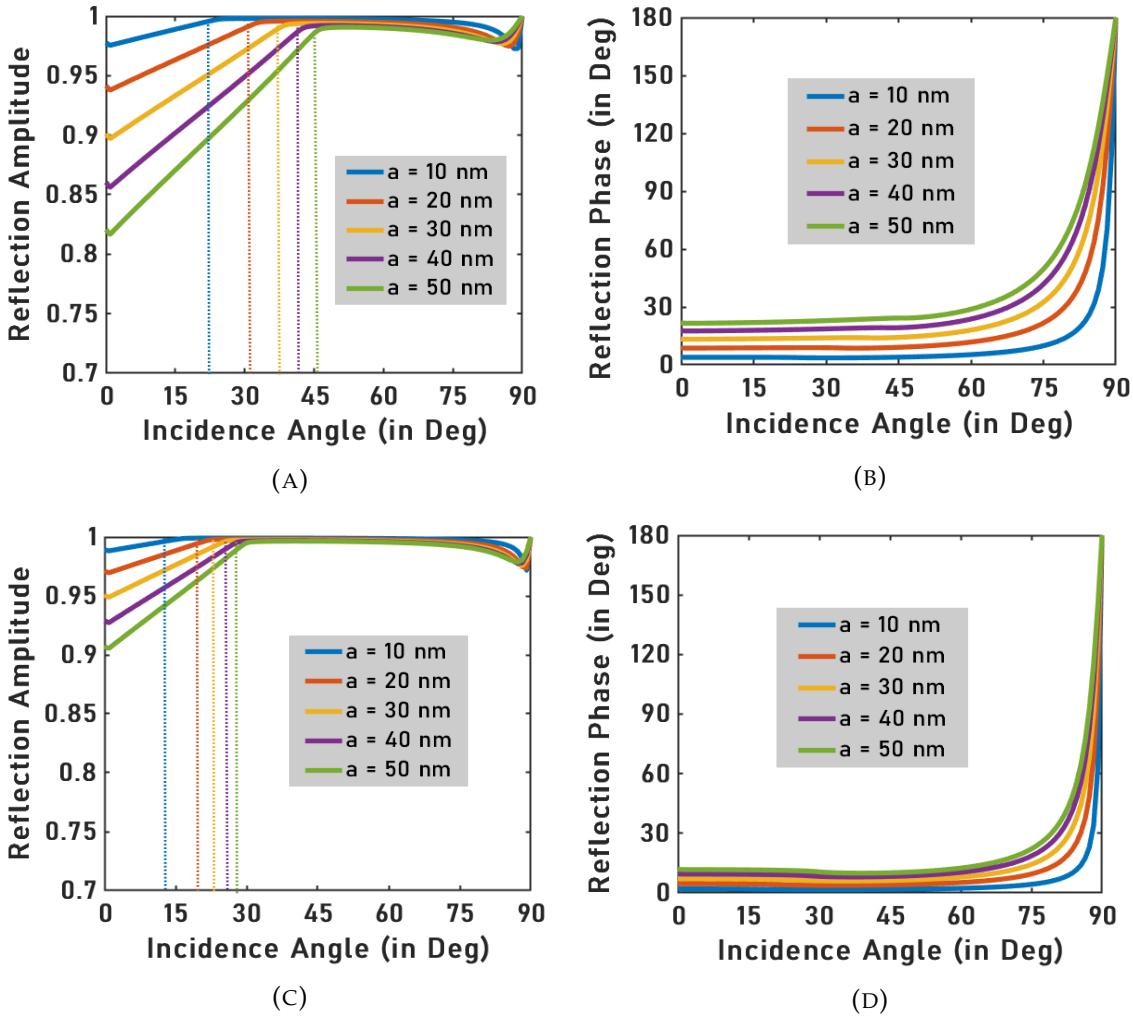

FIGURE 4.2: (A) Reflection amplitude and (B) reflection phase of the gap-plasmon mode in a plasmonic slot waveguide completely surrounded by silica (SiO_2) of refractive index 1.44, $\epsilon_d = \epsilon_{d1} = 2.0736$. (C) Reflection amplitude and (D) phase for SiO_2 inside the slot and air outside it for widths of 10 nm to 50 nm at a wavelength of 1550 nm. Vertical dotted lines indicate the critical angles. Adapted from Pati, A. *et. al* with permission [27].

By matching these fields at the boundary ($z = 0$) and using the orthogonality of modes, we obtained the relationship between r_1 and the transmission coefficient $t(u)$ as follows:

$$t(u) = \lambda \frac{(1 + r_1)}{\pi u} \sin\left(\frac{\pi a u}{\lambda}\right) \tag{4.3}$$

where, $u = k_x/k_0$. Similarly, the transverse component of the magnetic field (H_y) inside the slot is given as:

$$H_y(z = 0^-) = \frac{\omega\sqrt{\epsilon}_d}{k_0}(1 - r_1)\text{rect}\left(\frac{x}{a}\right)\exp\left(ik_y.y\right)\cos\theta \tag{4.4}$$

and just above the slot is given as:

$$H_y(z = 0^+) = \omega\epsilon_{d1}\int_{-\infty}^{\infty} t(k_x)\frac{\sqrt{\epsilon_{d1}k_0^2 - \epsilon_d k_0^2\sin^2\theta - k_x^2}}{\epsilon_{d1}k_0^2 - k_x^2}\exp(ik_x.x + ik_y.y)\, dk_x \tag{4.5}$$

On replacing k_x by uk_0, substituting the value of $t(u)$ obtained from Eq. 4.3, and applying orthogonality condition to the matched transverse magnetic fields, we obtained r_1 as:

$$r_1 = \frac{\sqrt{\frac{\epsilon_d}{\epsilon_{d1}}}\cos\theta - I_1}{\sqrt{\frac{\epsilon_d}{\epsilon_{d1}}}\cos\theta + I_1} \tag{4.6}$$

where, I_1 is:

$$I_1 = \int_{-\infty}^{\infty} \frac{\sqrt{1 - \frac{\epsilon_d}{\epsilon_{d1}}\sin^2\theta - \frac{u^2}{\epsilon_{d1}}}}{1 - \frac{u^2}{\epsilon_{d1}}}\frac{\sin^2(\pi u w)}{\pi^2 u^2 w}\, du \tag{4.7}$$

and $w = \dfrac{a}{\lambda}$. The same steps were used to derive an expression for the reflection coefficient at the bottom of the slot (r_2), the only difference in the resulting equation was that ϵ_{d1} was replaced by ϵ_{d2}.

For the case of a real metal, ϵ_d was replaced by n_{MIM}^2 resulting in new values of r_1 and I_1 as:

$$r_1 = \frac{\sqrt{\frac{n_{\mathrm{MIM}}^2}{\epsilon_{d1}}}\cos\theta - I_1}{\sqrt{\frac{n_{\mathrm{MIM}}^2}{\epsilon_{d1}}}\cos\theta + I_1} \tag{4.8}$$

and:

$$I_1 = \int_{-\infty}^{\infty} \frac{\sqrt{1 - \frac{n_{\mathrm{MIM}}^2}{\epsilon_{d1}}\sin^2\theta - \frac{u^2}{\epsilon_{d1}}}}{1 - \frac{u^2}{\epsilon_{d1}}} \frac{\sin^2(\pi u w)}{\pi^2 u^2 w}\, du \tag{4.9}$$

Figure 4.2a shows the variation of reflection amplitude with the propagation angle for different slot widths. The material above and below the interface is (SiO_2) of refractive index 1.44 ($\epsilon_d = \epsilon_{d1}$). The reflection amplitudes are higher for narrower slots due to increased penetration of the electric fields into the metal. When the angle exceeds the critical angle, given by $\sin^{-1}\left[\sqrt{\epsilon_{d1}}/n_{\mathrm{MIM}}\right]$ and indicated by the vertical dotted lines, total internal reflection takes place but the reflection amplitude is slightly less than 1 due to metal absorption. Narrower gaps have lower critical angles due to a higher difference between refractive indices inside and outside the slot. The reflection phase shown in Figure 4.2b increases with θ and the slot width but reaches π for $\theta = \pi/2$ regardless of the gap widths.

Figure 4.2c shows the reflection amplitude for a slot interface with SiO_2 inside and air outside ($\epsilon_d \neq \epsilon_{d1}$). The values of reflection amplitude for corresponding widths are slightly greater compared to those in Figure 4.2a. This is due to the increased contrast between the index of the gap plasmon inside the slot and that of air outside as opposed to SiO_2, which also results in lower values of critical angles. The reflection phases in Figure 4.2d are similar in their overall trend to Figure 4.2b but they appear more squeezed together due to their lower values resulting from the higher contrast.

4.3 Geometric Optics Approach

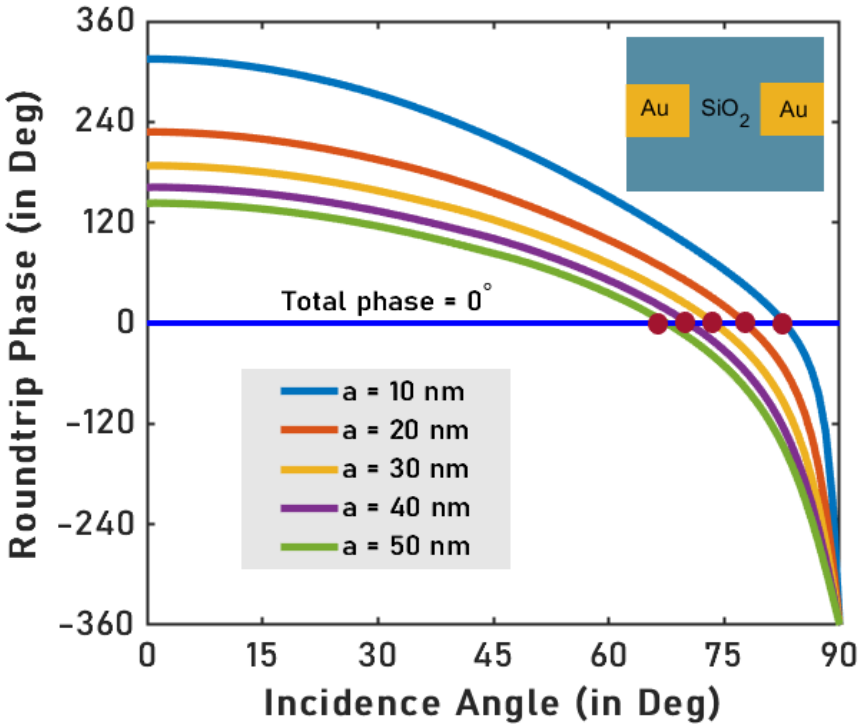

FIGURE 4.3: Total roundtrip phase of the EM waves in the symmetric waveguide completely surrounded by SiO_2 for slot widths of 10 nm to 50 nm and metal thickness of 200 nm. Horizontal blue line represents a total phase of 0 and the red circles are fundamental mode solutions. Adapted from Pati, A. *et. al* with permission [27].

The solutions for propagation angles of the plasmonic slot waveguide were calculated from the transverse resonance condition also known as the self-consistency condition. This approach has been previously used to determine the properties of plasmonic stripe waveguide [137]. For a waveguide to sustain a bound mode, the total phase acquired in a roundtrip must be integral multiples of 2π, written as:

$$2 \times \Re(\beta) \times l \cos\theta_m - \phi_1 - \phi_2 = 2m\pi \tag{4.10}$$

m is an integer and ϕ_1 and ϕ_2 are the reflection phases at the top and bottom interfaces of the slot. $\Re(\beta)$ is the real part of the complex propagation constant in the MIM. The values of θ_m that satisfied Eq. 4.10 for different values of m were used in the following equation to calculate the mode effective indices ($n_{m,\text{mode}}$) for the fundamental and higher order modes:

$$n_{m,\text{mode}} = n_{\text{MIM}} \sin\theta_m \tag{4.11}$$

For all our subsequent calculations we used two configurations of plasmonic slot waveguides: symmetric and asymmetric. For the symmetric case, the two gold films were completely surrounded by SiO_2 ($\epsilon_{d1} = \epsilon_d = \epsilon_{d2}$) and therefore $r_1 = r_2$. The asymmetric waveguide had air above the top interface and SiO_2 inside the slot and as the substrate ($\epsilon_{d1} \neq \epsilon_d = \epsilon_{d2}$) implying $r_1 \neq r_2$.

4.3.1 Symmetric Waveguide

Figure 4.3 shows the total roundtrip phase of the gap plasmon mode in the symmetric configuration for slot widths ranging from 10 nm to 50 nm and film thickness of 200 nm. This was calculated from the left-hand side of Eq. 4.10 by using $\phi_1 = \phi_2$. The horizontal blue solid line corresponds to a phase of 0. Its intersection with the total phase curves, denoted by the red circles is the fundamental mode solution of the symmetric waveguide.

Figure 4.4a shows the variation of the fundamental mode effective index and propagation length with the slot width of the symmetric waveguide. The effective index increases with a decrease in the slot width similar to a 2D slit due to the increasing amount of electric field entering the metal. As $a \to 0$, the effective index approaches n_{MIM}, since the fundamental order solution $\theta \to 90^\circ$. These observations were also verified using numerical simulations shown by red squares. They

were performed by solving the mode source in ANSYS Lumerical FDTD v2020 R2.3 within perfectly matched layer boundaries.

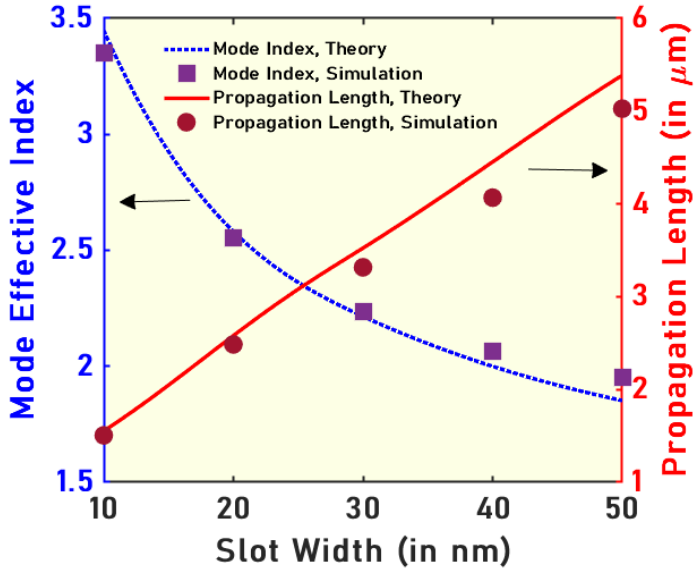

(A)

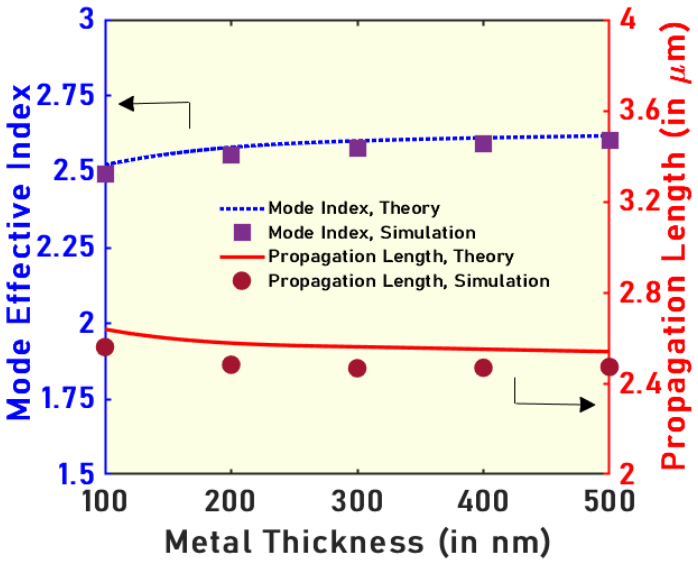

(B)

FIGURE 4.4: Variation of the fundamental mode effective index (blue dotted line shows theoretical results and squares indicate simulation results) and propagation length (red solid line shows theoretical results and circles indicate simulation results) of the symmetric waveguide (A) with slot width for a metal thickness of 200 nm and (B) with metal thickness for a slot width of 20 nm. Adapted from Pati, A. *et. al* with permission [27].

A uniform mesh size of 0.1 nm was used inside the slot and 1 nm was used for the rest of the simulation region. Au (Gold) - Johnson and Christy was chosen from the Material Database to form the gold layers and a user-defined index of 1.44 was used for silica. The red solid line in Figure 4.4a shows the theoretical values of propagation length calculated by the expression $1/2[\mathrm{Imag}(n_{\mathrm{mode}}k_0) + \alpha]$. Here, α accounts for the absorption taking place during reflection computed from the following equation:

$$\exp\left(-2\alpha \times l \times \tan\theta\right) = |r_1 r_2| \tag{4.12}$$

$2 \times l \times \tan\theta$ is the path covered in a single roundtrip along the mode propagation direction (y-direction). The red circles in Figure 4.4a show the propagation length values gathered from the simulations. Figure 4.4b shows the variation of the effective index with metal thickness for a slot width of 20 nm. The index values increase with increasing metal thickness and approach n_{MIM} asymptotically as $l \to \infty$. Conversely, the propagation length of the mode becomes shorter.

4.3.2 Asymmetric Waveguide

Figure 4.5 shows the total phase for an asymmetric waveguide. The slot dimensions are the same as those presented in Figure 4.3. The blue solid line represents a total phase of 0 and the red circles represent the modal solutions for the different slot widths.

Figure 4.6a shows the influence of slot width on the fundamental mode index and propagation length of the asymmetric waveguide. Their values are close to the symmetric waveguide results shown in Figure 4.4a as the material inside the slot in both the cases remains same and only the material outside one of the interfaces is changed from a refractive index 1.44 to 1.00. Larger differences in the effective index of the slot mode were observed when the material inside the slot was changed.

This was plotted in Figure 4.7 for a 10% and 50% increase in the refractive index of material inside the slot (silica).

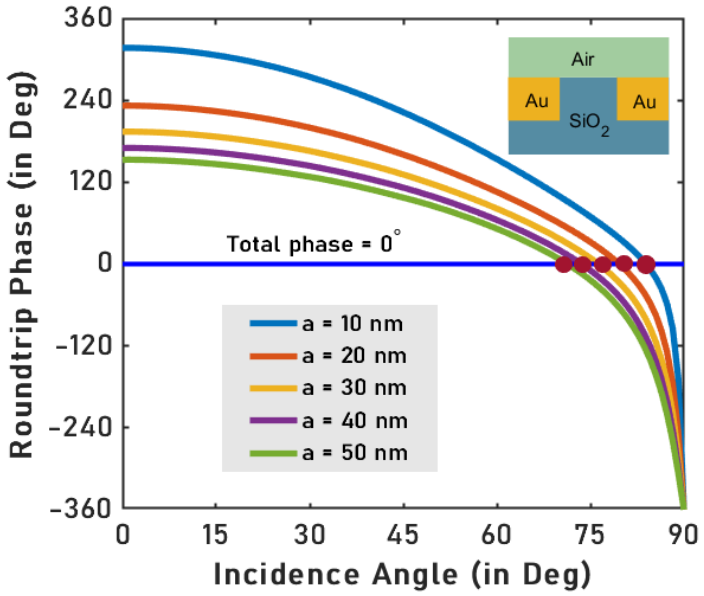

FIGURE 4.5: Total roundtrip phase of the EM waves in the asymmetric waveguide with SiO_2 inside and below it and air above for widths of 10 nm to 50 nm and metal thickness of 200 nm. Horizontal blue line represents a total phase of 0 and red circles are fundamental mode solutions. Adapted from Pati, A. *et. al* with permission [27].

It is important to note that the theory is most accurate in the fundamental mode calculation when the slot's aspect ratio (ratio of metal thickness to slot width) is greater than 1. Previous work has shown that the gap plasmon mode no longer remains the fundamental mode for lower aspect ratio slots as the quasi-TEM condition does not hold [23]. The gap plasmon approximation of the plasmonic slot waveguide should therefore be used for $l > a$.

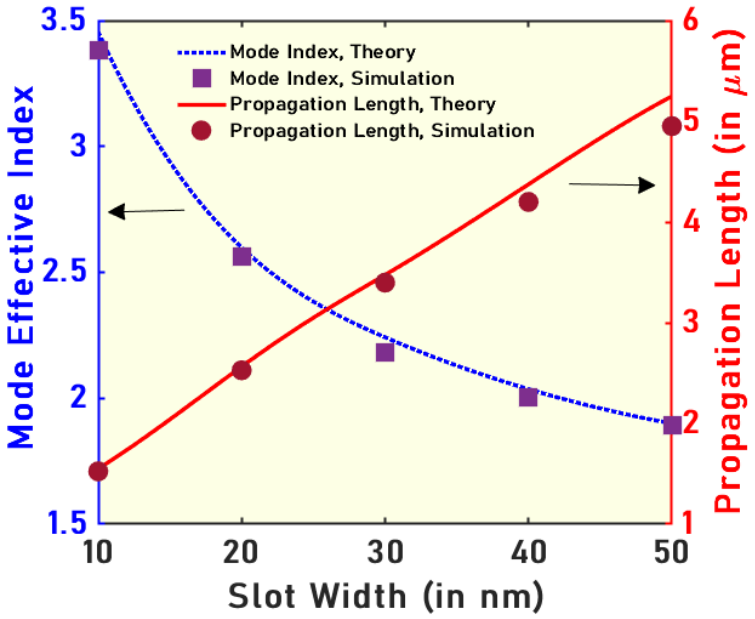

(A)

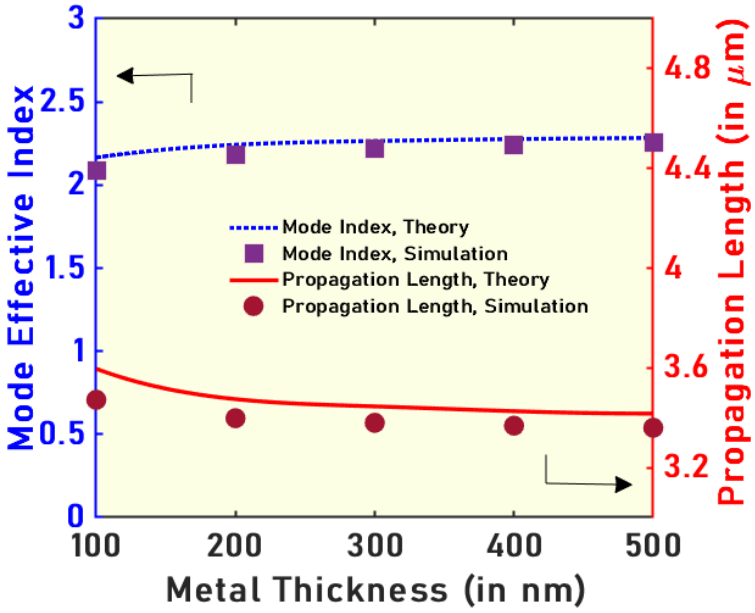

(B)

FIGURE 4.6: Variation of the fundamental mode effective index (blue dotted line shows theoretical results and squares indicate simulation results) and propagation length (red solid line shows theoretical results and circles indicate simulation results) of the asymmetric waveguide (A) with slot width for a metal thickness of 200 nm and (B) with metal thickness for a slot width of 30 nm. Adapted from Pati, A. *et. al* with permission [27].

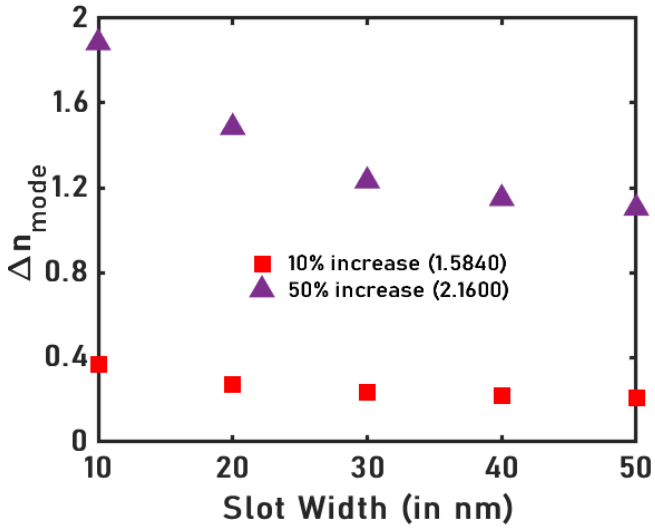

FIGURE 4.7: Absolute change in the mode effective index of the fundamental order mode in a symmetric plasmonic slot waveguide of metal height 200 nm, surrounded by SiO_2, when the refractive index inside the slot is increased by 10% and 50%. Adapted from Pati, A. *et. al* with permission [27].

4.3.3 Higher Order Modes

Although the single-mode operation is desired for most applications of plasmonic slot waveguides, we believe it was useful to validate our analysis for higher-order modes as well. We used an asymmetric waveguide with the same configuration as in Section 4.3.3 for a slot width of 20 nm and an increased thickness of 750 nm. As shown in Figure 4.8a we obtained zeroth order mode at an angle of 84.8°, 1^{st} order mode at 65.61°, and 2^{nd} order mode at 37.311° marked by the red circles. The corresponding effective indices were calculated from Eq. 4.11 as 2.6308, 2.4060, and 1.6012 shown in Figure 4.8b along with the numerical values for the same configuration.

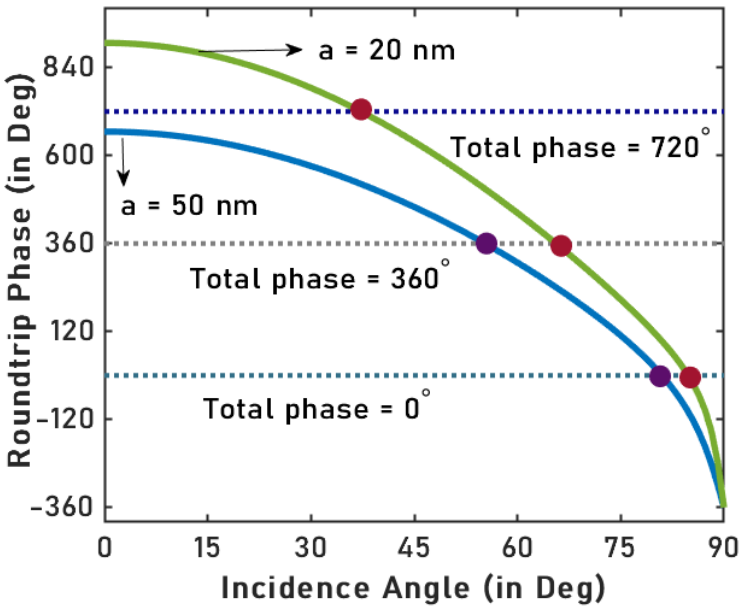

(A)

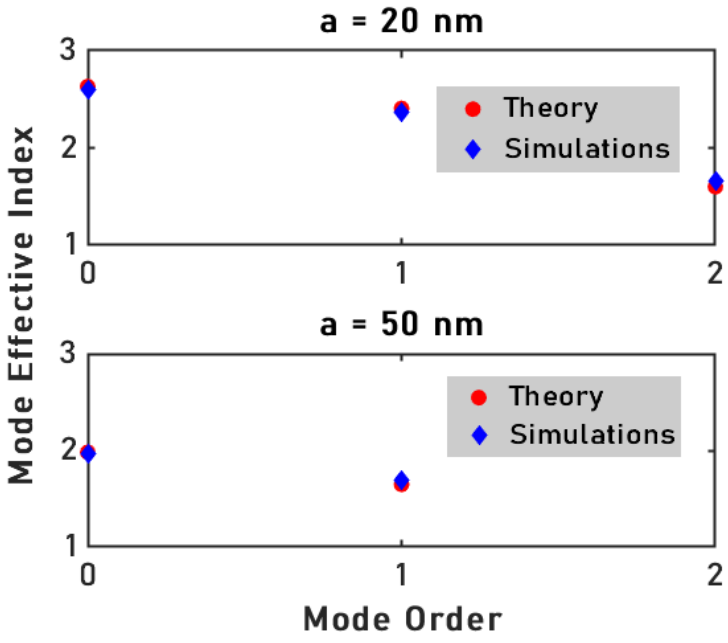

(B)

FIGURE 4.8: (A) Fundamental and higher order modal solutions for an asymmetric waveguide of thickness 750 nm and widths 20 nm and 50 nm. Horizontal dotted lines indicate a phase of 0°, 360°, and 720°. (B) Mode effective indices of the above orders from theoretical calculations and numerical simulations. Adapted from Pati, A. *et. al* with permission [27].

We observed that the presence of higher-order modes (in the z-direction) depends not just on the film thickness but also on the slot width. When the width of the slot was changed from 20 nm to 50 nm, keeping the thickness constant at 750 nm, the number of modes reduced from three to two as indicated in Figure 4.8a. Their effective indices obtained from theory and numerical calculations are shown in Figure 4.8b. The number of modes in the slot (localized in the z-direction) and their corresponding index values increase with the increase in the aspect ratio of the slot.

4.3.4 Possible Existence of Edge Plasmons in a Slot

In the previous section, we mentioned that the theory is most accurate when the aspect ratio of the slot is greater than 1. In an effort to understand the deviation for lower aspect ratio slots, we plotted the extension of the mode effective variation shown in Figure 4.6b (for a slot width of 30 nm) for film thickness below 100 nm. We observed that below 50 nm, the theoretical values of the mode index keep decreasing similar to the results shown in another work [18], whereas the numerical values increase. As has been pointed out in previous work, with decreasing l, the electric fields at the two Au-Air interfaces at $z = l$ and the two Au-SiO_2 interfaces at $z = 0$ increase [16]. A significantly larger portion of the power resides in the metal resulting in an increase in the mode index. In other words, for extremely thin metallic films, the characteristics of the fundamental mode are closer to weakly coupled edge plasmons than gap plasmons. The increase in mode index is therefore not reflected by our theory, which has the gap plasmon assumption at its heart.

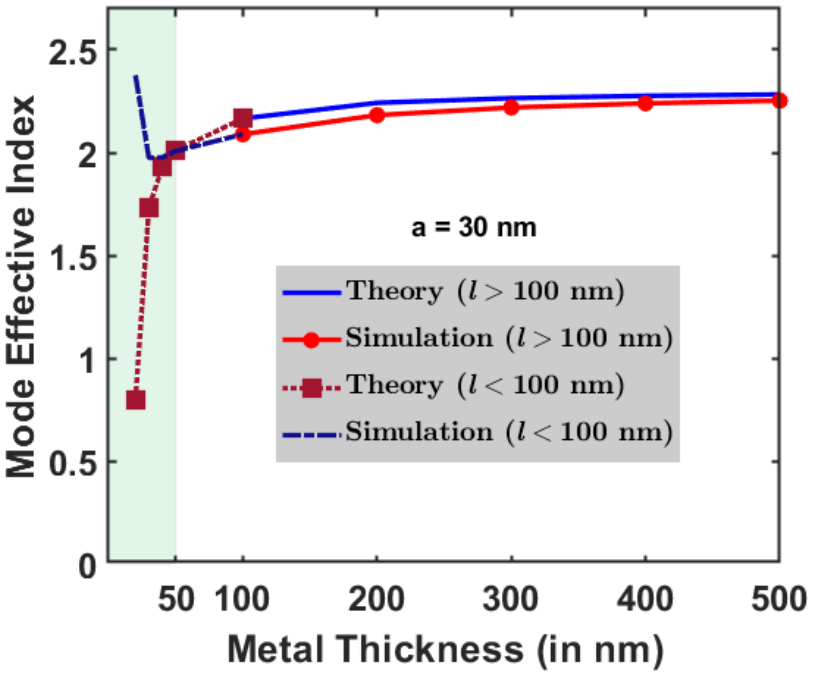

(A)

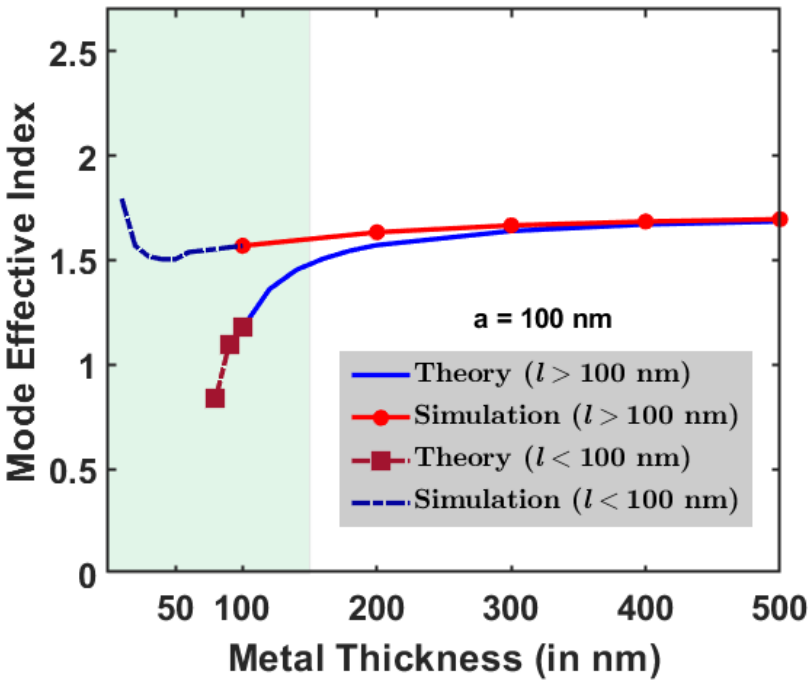

(B)

FIGURE 4.9: Mode effective index vs film thickness of an asymmetric waveguide of (A) width 30 nm and (B) 100 nm obtained from theory and numerical calculations. The shaded green region shows the region where the theory deviates from numerical calculations.

To further investigate this behavior, we increased the slot width to 100 nm, further lowering the aspect ratio, as shown in Figure 4.9b. We observed that the theoretical results start deviating from numerical values for a film thickness of 150 nm, which is significantly higher than the 50 nm shown in the previous case. Some works in the past have suggested that the fundamental mode is a gap plasmon mode at the optical communication wavelength (1550 nm), showing edge plasmon-like behavior only for extremely thin metallic films due to fringing effects [16]. Another work has suggested that the fundamental mode in a slot is only composed of edge plasmon [115], which doesn't align with simulations that demonstrate electric field distribution, characteristic of gap plasmon modes.

For both symmetric and asymmetric waveguides, our theoretical results have been shown to be accurate for high aspect ratio slots. The discrepancy arises only when the aspect ratio falls below 1. One implication of this observation is that the fundamental mode inside the slot is strongly influenced by the aspect ratio of the waveguide, showing gap plasmon behavior for high aspect ratio slots and edge plasmon-like behavior for lower aspect ratios. This has also been shown by numerical simulations in an existing review on plasmonic waveguiding [23]. Therefore, just like the existence of higher-order modes, the gap plasmon characteristics of the slot are not just dependent on any one of the structural parameters (a or l) but on the combination of both. This is also a key consideration for the design optimization of the plasmonic slot geometry as its coupling with the photonic modes relies on the features of the mode in the slot.

The theoretical analysis of plasmonic slot waveguides has been done by several works using two main approaches: numerical analysis [16]–[19], [115], [130] and effective index method [144]. Though accurate, numerical simulations lack insights and are resource-intensive. In contrast, the proposed analytical method determines mode properties in terms of other physical parameters. We used the

standard numerical integration of Eq. 4.9; however, approximate solutions to this equation may be attempted [104] (although we have not found them in this work).

The effective index method is a simpler and analytic alternative to numerical simulations. But it does not account for the mode-shape mismatch at slot interfaces, and therefore provides a less accurate picture of the reflection. In this work, the error between the analytical and numerical results was calculated to be under 3% with the highest deviations observed for narrow slots as higher penetration of fields reduces the accuracy of PEC approximation. The accuracy of the model can be improved by considering the exact electric field expressions at the cost of the simplicity of Eq. 4.9 and relatively shorter run times.

Chapter 5

Conclusion

In this thesis, we have presented analytical frameworks to understand and quantify the reflection and propagation of electromagnetic waves in i). subwavelength slits in metal and ii). plasmonic slot waveguides. Before introducing the models, we reviewed the fundamentals of surface plasmon polaritons in Chapter 2. We briefly discussed localized surface plasmon polaritons and their applications in different areas. In the next section, we moved to propagating surface plasmon polaritons, the main focus of this dissertation. We derived and plotted the field equations and dispersion relations relevant to a single metal-dielectric interface, an IMI, and a MIM structure. In the end, we discussed some of the major applications of propagating surface plasmons.

In Chapter 3, we presented a purely analytic model for subwavelength metallic slits. The theory consists of two main stages, in the first, we derived an equation for reflection at the slit interface with a dielectric medium using a combination of perfect electric conductor approximation, single-mode matching to continuum, and dielectric loading. The resulting values of reflection phase and amplitude were used in the Fabry-Pérot model to obtain expressions for field enhancement, power, scattering, and absorption cross-sections. We demonstrated that the power through the slit peaks for configurations having equal scattering and absorption cross-sections at the resonance condition. This observation has crucial implications

in plasmonic design, where the narrowest slit before the onset of tunneling is often considered to be the best geometry due to the high confinement it offers. In practical implementation, where losses (increase with confinement) become paramount, the use of power as a figure of merit, as opposed to field enhancement will provide a better way to optimize the slit geometry for various applications.

In Chapter 4, we introduced the analytical framework for mode propagation in plasmonic slot waveguides. Here we also used the PEC approximation in conjunction with single-mode matching to continuum and dielectric loading to obtain expressions for reflection coefficients at the slot's interface with its surrounding dielectric media. Therefore, the theory shed light on the reflection of the gap plasmon and its variation with the propagation angles. The reflection phase values above the critical angles were used in the transverse resonance condition in geometric optics to obtain values of propagation angles that supported fundamental and/or higher-order modes. The angular solutions were then used to compute modal properties such as effective index and propagation length for different waveguide parameters. The theoretical results demonstrated close agreement with numerical simulation results within 3% and were two orders of magnitude faster than numerical simulations.

5.1 Scope

The combination of an approximate mode shape with dielectric loading has provided a way for the efficient analysis of metallic slits and plasmonic slot waveguides. In the future, this combination can be extended to other plasmonic structures like cylindrical nanoapertures in metallic screens. The theory can also incorporate the spectrum or gain of the dielectric medium in the gap for optimization in applications like lasing [145] and gas sensing [146].

We have also seen that the model provides information about the critical propagation angles in a plasmonic slot waveguide. The reflectivity and critical angles are dependent on the refractive index of the dielectric in the slot. The changes in the critical angle can be mapped to changes in the refractive index of the slot, which has been shown to be useful in sensing applications using dielectrics [147]. The strong dependence of the reflection phase on the propagation angles, shown in Figures 4.4b and 4.6b and the presence of leaky modes in asymmetric slot waveguide can be combinedly applied to improve the sensitivity of surface plasmon resonance sensors by adding slots to the metal films.

In summary, the theory may be used to explore other nanostructure geometries where field distributions can be approximated by constant functions similar to the rectangle function shown here. The insights gained on the physical properties and their interdependence may be used to go beyond the current applications of these geometries. Finally, the model can be used in the rapid design and optimization of metallic slits and plasmonic slot waveguides for different applications by mitigating the challenges inherent to plasmon-based components.

Bibliography

[1] D. K. Gramotnev and S. I. Bozhevolnyi, "Plasmonics beyond the diffraction limit," *Nature photonics*, vol. 4, no. 2, pp. 83–91, 2010.

[2] M. I. Stockman, "Nanoplasmonics: Past, present, and glimpse into future," *Optics express*, vol. 19, no. 22, pp. 22 029–22 106, 2011.

[3] C. Haffner, W. Heni, Y. Fedoryshyn, *et al.*, "All-plasmonic mach-zehnder modulator enabling optical high-speed communication at the microscale," *Nature Photon*, vol. 9, no. 8, pp. 525–528, 2015.

[4] W. Heni, Y. Fedoryshyn, B. Baeuerle, *et al.*, "Plasmonic iq modulators with attojoule per bit electrical energy consumption," *Nature communications*, vol. 10, no. 1, p. 1694, 2019.

[5] U. Koch, C. Uhl, H. Hettrich, *et al.*, "A monolithic bipolar cmos electronic–plasmonic high-speed transmitter," *Nature Electronics*, vol. 3, no. 6, pp. 338–345, 2020.

[6] L. Brus, "Noble metal nanocrystals: Plasmon electron transfer photochemistry and single-molecule raman spectroscopy," *Accounts of chemical research*, vol. 41, no. 12, pp. 1742–1749, 2008.

[7] N. Maccaferri, G. Barbillon, A. N. Koya, G. Lu, G. P. Acuna, and D. Garoli, "Recent advances in plasmonic nanocavities for single-molecule spectroscopy," *Nanoscale Advances*, vol. 3, no. 3, pp. 633–642, 2021.

[8] M. Seo, H. Park, S. Koo, *et al.*, "Terahertz field enhancement by a metallic nano slit operating beyond the skin-depth limit," *Nature Photonics*, vol. 3, no. 3, pp. 152–156, 2009.

[9] A. Novitsky, A. M. Ivinskaya, M. Zalkovskij, R. Malureanu, P. Uhd Jepsen, and A. V. Lavrinenko, "Non-resonant terahertz field enhancement in periodically arranged nanoslits," *Journal of Applied Physics*, vol. 112, no. 7, p. 074 318, 2012.

[10] T. Xu, Y. Zhao, D. Gan, C. Wang, C. Du, and X. Luo, "Directional excitation of surface plasmons with subwavelength slits," *Applied Physics Letters*, vol. 92, no. 10, p. 101 501, 2008.

[11] Y Takakura, "Optical resonance in a narrow slit in a thick metallic screen," *Phys. Rev. Lett.*, vol. 86, no. 24, p. 5601, 2001.

[12] F. García-Vidal, H. Lezec, T. Ebbesen, and L Martín-Moreno, "Multiple paths to enhance optical transmission through a single subwavelength slit," *physical review letters*, vol. 90, no. 21, p. 213 901, 2003.

[13] R. Gordon, "Light in a subwavelength slit in a metal: Propagation and reflection," *Phys.Rev. B*, vol. 73, no. 15, p. 153 405, 2006.

[14] R. Gordon, "Near-field interference in a subwavelength double slit in a perfect conductor," *J. Opt. A: Pure Appl. Opt.*, vol. 8, pp. L1–L3, 2006.

[15] Y Pang, C Genet, and T. Ebbesen, "Optical transmission through subwavelength slit apertures in metallic films," *Optics Communications*, vol. 280, no. 1, pp. 10–15, 2007.

[16] G. Veronis and S. Fan, "Modes of subwavelength plasmonic slot waveguides," *Journal of Lightwave Technology*, vol. 25, no. 9, pp. 2511–2521, 2007.

[17] G. Veronis and S. Fan, "Guided subwavelength plasmonic mode supported by a slot in a thin metal film," *Opt. Lett.*, vol. 30, no. 24, pp. 3359–3361, 2005.

[18] N.-N. Feng, M. L. Brongersma, and L. Dal Negro, "Metal–dielectric slot-waveguide structures for the propagation of surface plasmon polaritons at 1.55μm," *IEEE Journal of Quantum Electronics*, vol. 43, no. 6, pp. 479–485, 2007.

[19] L. Liu, Z. Han, and S. He, "Novel surface plasmon waveguide for high integration," *Opt. Express*, vol. 13, no. 17, pp. 6645–6650, 2005.

[20] Y. Fang and M. Sun, "Nanoplasmonic waveguides: Towards applications in integrated nanophotonic circuits," *Light Sci Appl*, vol. 4, no. 6, e294–e294, 2015.

[21] L. Chen, J. Shakya, and M. Lipson, "Subwavelength confinement in an integrated metal slot waveguide on silicon," *Opt. Lett.*, vol. 31, no. 14, pp. 2133–2135, 2006.

[22] E. Ozbay, "Plasmonics: Merging photonics and electronics at nanoscale dimensions," *Science*, vol. 311, no. 5758, pp. 189–193, 2006.

[23] Z. Han and S. I. Bozhevolnyi, "Radiation guiding with surface plasmon polaritons," *Reports on Progress in Physics*, vol. 76, no. 1, p. 016 402, 2012.

[24] Y. Salamin, B. Baeuerle, W. Heni, *et al.*, "Microwave plasmonic mixer in a transparent fibre–wireless link," *Nature Photon*, vol. 12, no. 12, pp. 749–753, 2018.

[25] S. Ummethala, T. Harter, K. Koehnle, *et al.*, "Thz-to-optical conversion in wireless communications using an ultra-broadband plasmonic modulator," *Nat. Photonics*, vol. 13, no. 8, pp. 519–524, 2019.

[26] R. Oulton, G Bartal, D. Pile, and X. Zhang, "Confinement and propagation characteristics of subwavelength plasmonic modes," *New Journal of Physics*, vol. 10, no. 10, p. 105 018, 2008.

[27] A. Pati and R. Gordon, "Plasmonic slot waveguide propagation analysis [PREPRINT]," *Plasmonics*, 2022.

[28] A. Pati and R. Gordon, "Maximum power transfer in a real metal slit: An analytic approach," *Opt. Express*, vol. 29, no. 23, pp. 38 129–38 139, 2021.

[29] M. E. Stewart, C. R. Anderton, L. B. Thompson, *et al.*, "Nanostructured plasmonic sensors," *Chemical reviews*, vol. 108, no. 2, pp. 494–521, 2008.

[30] F. Hong and R. Blaikie, "Plasmonic lithography: Recent progress," *Advanced Optical Materials*, vol. 7, no. 14, p. 1 801 653, 2019.

[31] U. Hohenester, *Nano and Quantum Optics*. Springer, 2020.

[32] P. K. Jain and M. A. El-Sayed, "Surface plasmon resonance sensitivity of metal nanostructures: Physical basis and universal scaling in metal nanoshells," *The Journal of Physical Chemistry C*, vol. 111, no. 47, pp. 17 451–17 454, 2007.

[33] C. Bohren and D. Huffman, *Absorption and Scattering of Light by Small Particles*. John Wiley & Sons, Ltd, 1998.

[34] A. J. Haes and R. P. Van Duyne, "A nanoscale optical biosensor: Sensitivity and selectivity of an approach based on the localized surface plasmon resonance spectroscopy of triangular silver nanoparticles," *Journal of the American Chemical Society*, vol. 124, no. 35, pp. 10 596–10 604, 2002.

[35] N. L. Rosi and C. A. Mirkin, "Nanostructures in biodiagnostics," *Chemical reviews*, vol. 105, no. 4, pp. 1547–1562, 2005.

[36] K. Sokolov, M. Follen, J. Aaron, *et al.*, "Real-time vital optical imaging of precancer using anti-epidermal growth factor receptor antibodies conjugated to gold nanoparticles," *Cancer research*, vol. 63, no. 9, pp. 1999–2004, 2003.

[37] I. H. El-Sayed, X. Huang, and M. A. El-Sayed, "Surface plasmon resonance scattering and absorption of anti-egfr antibody conjugated gold nanoparticles in cancer diagnostics: Applications in oral cancer," *Nano letters*, vol. 5, no. 5, pp. 829–834, 2005.

[38] K. Fuku, R. Hayashi, S. Takakura, T. Kamegawa, K. Mori, and H. Yamashita, "The synthesis of size-and color-controlled silver nanoparticles by using microwave heating and their enhanced catalytic activity by localized surface plasmon resonance," *Angewandte Chemie*, vol. 125, no. 29, pp. 7594–7598, 2013.

[39] F. Beck, A Polman, and K. Catchpole, "Tunable light trapping for solar cells using localized surface plasmons," *Journal of Applied Physics*, vol. 105, no. 11, p. 114 310, 2009.

[40] X. Gu, T. Qiu, W. Zhang, and P. K. Chu, "Light-emitting diodes enhanced by localized surface plasmon resonance," *Nanoscale research letters*, vol. 6, no. 1, pp. 1–12, 2011.

[41] S. A. Maier *et al.*, *Plasmonics: fundamentals and applications*. Springer, 2007, vol. 1.

[42] P. B. Johnson and R. W. Christy, "Optical constants of the noble metals," *Phys. Rev. B*, vol. 6, pp. 4370–4379, 1972.

[43] A. Otto, "Excitation of nonradiative surface plasma waves in silver by the method of frustrated total reflection," *Zeitschrift für Physik A Hadrons and nuclei*, vol. 216, no. 4, pp. 398–410, 1968.

[44] E. Kretschmann and H. Raether, "Radiative decay of non radiative surface plasmons excited by light," *Zeitschrift für Naturforschung A*, vol. 23, no. 12, pp. 2135–2136, 1968.

[45] J. Homola, S. S. Yee, and G. Gauglitz, "Surface plasmon resonance sensors," *Sensors and actuators B: Chemical*, vol. 54, no. 1-2, pp. 3–15, 1999.

[46] Y.-Y. Teng and E. A. Stern, "Plasma radiation from metal grating surfaces," *Physical Review Letters*, vol. 19, no. 9, p. 511, 1967.

[47] S. A. Maier and H. A. Atwater, "Plasmonics: Localization and guiding of electromagnetic energy in metal/dielectric structures," *Journal of applied physics*, vol. 98, no. 1, p. 10, 2005.

[48] P. R. West, S. Ishii, G. V. Naik, N. K. Emani, V. M. Shalaev, and A. Boltasseva, "Searching for better plasmonic materials," *Laser & photonics reviews*, vol. 4, no. 6, pp. 795–808, 2010.

[49] B Prade, J. Vinet, and A Mysyrowicz, "Guided optical waves in planar heterostructures with negative dielectric constant," *Physical Review B*, vol. 44, no. 24, p. 13 556, 1991.

[50] H. S. Won, K. C. Kim, S. H. Song, *et al.*, "Vertical coupling of long-range surface plasmon polaritons," *Applied physics letters*, vol. 88, no. 1, p. 011 110, 2006.

[51] E. Verhagen, J. A. Dionne, L Kuipers, H. A. Atwater, and A. Polman, "Near-field visualization of strongly confined surface plasmon polaritons in metal-insulator- metal waveguides," *Nano letters*, vol. 8, no. 9, pp. 2925–2929, 2008.

[52] J. Homola and M. Piliarik, "Surface plasmon resonance (spr) sensors," in *Surface plasmon resonance based sensors*, Springer, 2006, pp. 45–67.

[53] R. W. Wood, "Xlii. on a remarkable case of uneven distribution of light in a diffraction grating spectrum," *The London, Edinburgh, and Dublin Philosophical Magazine and Journal of Science*, vol. 4, no. 21, pp. 396–402, 1902.

[54] J. Maurya, Y. Prajapati, V Singh, and J. Saini, "Sensitivity enhancement of surface plasmon resonance sensor based on graphene–mos2 hybrid structure with tio2–sio2 composite layer," *Applied Physics A*, vol. 121, no. 2, pp. 525–533, 2015.

[55] G. Nenninger, P Tobiška, J Homola, and S. Yee, "Long-range surface plasmons for high-resolution surface plasmon resonance sensors," *Sensors and Actuators B: Chemical*, vol. 74, no. 1-3, pp. 145–151, 2001.

[56] Y. Xu, Y. S. Ang, L. Wu, and L. K. Ang, "High sensitivity surface plasmon resonance sensor based on two-dimensional mxene and transition metal dichalcogenide: A theoretical study," *Nanomaterials*, vol. 9, no. 2, p. 165, 2019.

[57] Y. Saylan, S. Akgönüllü, H. Yavuz, S. Ünal, and A. Denizli, "Molecularly imprinted polymer based sensors for medical applications," *Sensors*, vol. 19, no. 6, p. 1279, 2019.

[58] K. Saha, S. S. Agasti, C. Kim, X. Li, and V. M. Rotello, "Gold nanoparticles in chemical and biological sensing," *Chemical reviews*, vol. 112, no. 5, pp. 2739–2779, 2012.

[59] A. Ashkin, "Acceleration and trapping of particles by radiation pressure," *Physical review letters*, vol. 24, no. 4, p. 156, 1970.

[60] Y. Zhang, C. Min, X. Dou, *et al.*, "Plasmonic tweezers: For nanoscale optical trapping and beyond," *Light: Science & Applications*, vol. 10, no. 1, pp. 1–41, 2021.

[61] K. Wang and K. B. Crozier, "Plasmonic trapping with a gold nanopillar," *ChemPhysChem*, vol. 13, no. 11, pp. 2639–2648, 2012.

[62] Y. Lu, G. Du, F. Chen, *et al.*, "Tunable potential well for plasmonic trapping of metallic particles by bowtie nano-apertures," *Scientific reports*, vol. 6, no. 1, pp. 1–8, 2016.

[63] G. Rui, Y. Ma, B. Gu, Q. Zhan, and Y. Cui, "Plasmonic trapping of nanoparticles by metaholograms," *Scientific Reports*, vol. 7, no. 1, pp. 1–7, 2017.

[64] M. L. Juan, R. Gordon, Y. Pang, F. Eftekhari, and R. Quidant, "Self-induced back-action optical trapping of dielectric nanoparticles," *Nature Phys*, vol. 5, no. 12, pp. 915–919, 2009.

[65] Y. Pang and R. Gordon, "Optical trapping of a single protein," *Nano Lett.*, vol. 12, no. 1, pp. 402–406, 2012.

[66] A. Kotnala and R. Gordon, "Double nanohole optical tweezers visualize protein p53 suppressing unzipping of single dna-hairpins," *Biomedical optics express*, vol. 5, no. 6, pp. 1886–1894, 2014.

[67] J. Burkhartsmeyer, Y. Wang, K. S. Wong, and R. Gordon, "Optical trapping, sizing, and probing acoustic modes of a small virus," *Applied Sciences*, vol. 10, no. 1, p. 394, 2020.

[68] Y. Chen, A. Kotnala, L. Yu, J. Zhang, and R. Gordon, "Wedge and gap plasmonic resonances in double nanoholes," *Optics express*, vol. 23, no. 23, pp. 30 227–30 236, 2015.

[69] C. Haffner, D. Chelladurai, Y. Fedoryshyn, *et al.*, "Low-loss plasmon-assisted electro-optic modulator," *Nature*, vol. 556, no. 7702, pp. 483–486, 2018.

[70] M. Ayata, Y. Fedoryshyn, W. Heni, *et al.*, "High-speed plasmonic modulator in a single metal layer," *Science*, vol. 358, no. 6363, pp. 630–632, 2017.

[71] F. Yang and J. R. Sambles, "Resonant transmission of microwaves through a narrow metallic slit," *Phys. Rev. Lett.*, vol. 89, no. 6, p. 063 901, 2002.

[72] H. J. Lezec, A Degiron, E Devaux, *et al.*, "Beaming light from a subwavelength aperture," *Science*, vol. 297, no. 5582, pp. 820–822, 2002.

[73] Y. Xie, A. R. Zakharian, J. V. Moloney, and M. Mansuripur, "Transmission of light through slit apertures in metallic films," *Opt. Express*, vol. 12, no. 25, pp. 6106–6121, 2004.

[74] H. T. Miyazaki and Y. Kurokawa, "Squeezing visible light waves into a 3-nm-thick and 55-nm-long plasmon cavity," *Phys. Rev. Lett.*, vol. 96, no. 9, p. 097 401, 2006.

[75] T. Søndergaard, S. I. Bozhevolnyi, J. Beermann, S. M. Novikov, E. Devaux, and T. W. Ebbesen, "Resonant plasmon nanofocusing by closed tapered gaps," *Nano Lett.*, vol. 10, no. 1, pp. 291–295, 2010.

[76] F. J. Garcia-Vidal, L. Martin-Moreno, T. Ebbesen, and L Kuipers, "Light passing through subwavelength apertures," *Rev. Mod. Phys.*, vol. 82, no. 1, p. 729, 2010.

[77] X. Chen, H.-R. Park, N. C. Lindquist, J. Shaver, M. Pelton, and S.-H. Oh, "Squeezing millimeter waves through a single, nanometer-wide, centimeter-long slit," *Sci Rep*, vol. 4, no. 1, p. 6722, 2014.

[78] A. G. Brolo, E. Arctander, R. Gordon, B. Leathem, and K. L. Kavanagh, "Nanohole-enhanced raman scattering," *Nano Lett.*, vol. 4, no. 10, pp. 2015–2018, 2004.

[79] Y. Kurokawa and H. T. Miyazaki, "Metal-insulator-metal plasmon nanocavities: Analysis of optical properties," *Phys. Rev. B*, vol. 75, no. 3, p. 035 411, 2007.

[80] D. R. Ward, N. K. Grady, C. S. Levin, *et al.*, "Electromigrated nanoscale gaps for surface-enhanced raman spectroscopy," *Nano Lett.*, vol. 7, no. 5, pp. 1396–1400, 2007.

[81] P. Schön, N. Bonod, E. Devaux, *et al.*, "Enhanced second-harmonic generation from individual metallic nanoapertures," *Opt. Lett.*, vol. 35, no. 23, pp. 4063–4065, 2010.

[82] J. B. Lassiter, X. Chen, X. Liu, *et al.*, "Third-harmonic generation enhancement by film-coupled plasmonic stripe resonators," *ACS Photonics*, vol. 1, no. 11, pp. 1212–1217, 2014.

[83] M. S. Nezami, D. Yoo, G. Hajisalem, S.-H. Oh, and R. Gordon, "Gap plasmon enhanced metasurface third-harmonic generation in transmission geometry," *ACS Photonics*, vol. 3, no. 8, pp. 1461–1467, 2016.

[84] M. L. Juan, M. Righini, and R. Quidant, "Plasmon nano-optical tweezers," *Nature Photon*, vol. 5, no. 6, pp. 349–356, 2011.

[85] A. G. Brolo, R. Gordon, B. Leathem, and K. L. Kavanagh, "Surface plasmon sensor based on the enhanced light transmission through arrays of nanoholes in gold films," *Langmuir*, vol. 20, no. 12, pp. 4813–4815, 2004.

[86] K. A. Tetz, L. Pang, and Y. Fainman, "High-resolution surface plasmon resonance sensor based on linewidth-optimized nanohole array transmittance," *Opt. Lett.*, vol. 31, no. 10, pp. 1528–1530, 2006.

[87] A. Lesuffleur, H. Im, N. C. Lindquist, and S.-H. Oh, "Periodic nanohole arrays with shape-enhanced plasmon resonance as real-time biosensors," *Appl. Phys. Lett.*, vol. 90, no. 24, p. 243 110, 2007.

[88] R. Gordon, D. Sinton, K. L. Kavanagh, and A. G. Brolo, "A new generation of sensors based on extraordinary optical transmission," *Acc. Chem. Res.*, vol. 41, no. 8, pp. 1049–1057, 2008.

[89] K.-L. Lee, J.-B. Huang, J.-W. Chang, S.-H. Wu, and P.-K. Wei, "Ultrasensitive biosensors using enhanced fano resonances in capped gold nanoslit arrays," *Sci Rep*, vol. 5, no. 1, p. 8547, 2015.

[90] T. J. Seok, A. Jamshidi, M. Kim, *et al.*, "Radiation engineering of optical antennas for maximum field enhancement," *Nano Lett.*, vol. 11, pp. 2606–2610, 2011.

[91] Z. Sharifi and R. Gordon, "Large plasmonic resonance shifts from metal loss in slits," *Plasmonics*, 2021.

[92] C. Qian, X. Lin, Y. Yang, *et al.*, "Experimental observation of superscattering," *Phys. Rev. Lett.*, vol. 122, no. 6, p. 063 901, 2019.

[93] J. Aizpurua, P. Hanarp, D. Sutherland, M. Käll, G. W. Bryant, and F. G. De Abajo, "Optical properties of gold nanorings," *Physical review letters*, vol. 90, no. 5, p. 057 401, 2003.

[94] Z. Ruan and S. Fan, "Superscattering of light from subwavelength nanostructures," *Phys. Rev. Lett.*, vol. 105, no. 1, p. 013 901, 2010.

[95] W. Liu, "Superscattering pattern shaping for radially anisotropic nanowires," *Physical Review A*, vol. 96, no. 2, p. 023 854, 2017.

[96] M. I. Tribelsky and B. S. Luk'yanchuk, "Anomalous light scattering by small particles," *Physical review letters*, vol. 97, no. 26, p. 263 902, 2006.

[97] Z. Ruan and S. Fan, "Design of subwavelength superscattering nanospheres," *Applied Physics Letters*, vol. 98, no. 4, p. 043 101, 2011.

[98] O. D. Miller, C. W. Hsu, M. H. Reid, *et al.*, "Fundamental limits to extinction by metallic nanoparticles," *Physical review letters*, vol. 112, no. 12, p. 123 903, 2014.

[99] M. Zhou, L. Shi, J. Zi, and Z. Yu, "Extraordinarily large optical cross section for localized single nanoresonator," *Physical review letters*, vol. 115, no. 2, p. 023 903, 2015.

[100] M. Zhou, L. Ying, L. Lu, L. Shi, J. Zi, and Z. Yu, "Electromagnetic scattering laws in weyl systems," *Nature communications*, vol. 8, no. 1, pp. 1–7, 2017.

[101] C. Qian, Y. Yang, Y. Hua, *et al.*, "Breaking the fundamental scattering limit with gain metasurfaces," *Nature communications*, vol. 13, no. 1, pp. 1–7, 2022.

[102] L. Martin-Moreno, F. Garcia-Vidal, H. Lezec, *et al.*, "Theory of extraordinary optical transmission through subwavelength hole arrays," *Phys. Rev. Lett.*, vol. 86, no. 6, p. 1114, 2001.

[103] J. S. White, G. Veronis, Z. Yu, *et al.*, "Extraordinary optical absorption through subwavelength slits," *Opt. Lett.*, vol. 34, no. 5, pp. 686–688, 2009.

[104] R Gordon, "Angle-dependent optical transmission through a narrow slit in a thick metal film," *Phys. Rev. B*, vol. 75, no. 19, p. 193 401, 2007.

[105] S. E. Kocabas, G. Veronis, D. A. Miller, and S. Fan, "Transmission line and equivalent circuit models for plasmonic waveguide components," *IEEE Journal of Selected Topics in Quantum Electronics*, vol. 14, no. 6, pp. 1462–1472, 2008.

[106] C. Min, L. Yang, and G. Veronis, "Microcavity enhanced optical absorption in subwavelength slits," *Opt. Express*, vol. 19, no. 27, pp. 26 850–26 858, 2011.

[107] T. H. Isaac, J. G. Rivas, J. R. Sambles, W. L. Barnes, and E. Hendry, "Surface plasmon mediated transmission of subwavelength slits at thz frequencies," *Phys. Rev. B*, vol. 77, no. 11, p. 113 411, 2008.

[108] K. Yee, "Numerical solution of initial boundary value problems involving maxwell's equations in isotropic media," *IEEE Transactions on antennas and propagation*, vol. 14, no. 3, pp. 302–307, 1966.

[109] F. J. Garcia de Abajo, "Nonlocal effects in the plasmons of strongly interacting nanoparticles, dimers, and waveguides," *J. Phys. Chem. C*, vol. 112, no. 46, pp. 17 983–17 987, 2008.

[110] C. Ciracì, R. Hill, J. Mock, *et al.*, "Probing the ultimate limits of plasmonic enhancement," *Science*, vol. 337, no. 6098, pp. 1072–1074, 2012.

[111] A. Moreau, C. Ciraci, and D. R. Smith, "Impact of nonlocal response on metallodielectric multilayers and optical patch antennas," *Phys. Rev. B*, vol. 87, no. 4, p. 045 401, 2013.

[112] G. Hajisalem, M. S. Nezami, and R. Gordon, "Probing the quantum tunneling limit of plasmonic enhancement by third harmonic generation," *Nano Lett.*, vol. 14, no. 11, pp. 6651–6654, 2014.

[113] W. Zhu and K. B. Crozier, "Quantum mechanical limit to plasmonic enhancement as observed by surface-enhanced raman scattering," *Nat Commun*, vol. 5, no. 5228, p. 5228, 2014.

[114] R. Gordon and M. Dobinson, "Plasmonics–mine the gap: Opinion," *Opt. Mater. Express*, vol. 11, no. 7, pp. 2192–2196, 2021.

[115] D. F. Pile, T. Ogawa, D. K. Gramotnev, *et al.*, "Two-dimensionally localized modes of a nanoscale gap plasmon waveguide," *Appl. Phys. Lett.*, vol. 87, no. 26, p. 261 114, 2005.

[116] P. Ginzburg, D. Arbel, and M. Orenstein, "Gap plasmon polariton structure for very efficient microscale-to-nanoscale interfacing," *Opt. Lett.*, vol. 31, no. 22, pp. 3288–3290, 2006.

[117] N.-N. Feng and L. Dal Negro, "Plasmon mode transformation in modulated-index metal-dielectric slot waveguides," *Opt. Lett.*, vol. 32, no. 21, pp. 3086–3088, 2007.

[118] J. Tian, S. Yu, W. Yan, and M. Qiu, "Broadband high-efficiency surface-plasmon-polariton coupler with silicon-metal interface," *Appl. Phys. Lett.*, vol. 95, no. 1, p. 013 504, 2009.

[119] M. Ono, H. Taniyama, H. Xu, *et al.*, "Deep-subwavelength plasmonic mode converter with large size reduction for Si-wire waveguide," *Optica*, vol. 3, no. 9, pp. 999–1005, 2016.

[120] Y. Salamin, W. Heni, C. Haffner, *et al.*, "Direct conversion of free space millimeter waves to optical domain by plasmonic modulator antenna," *Nano Lett.*, vol. 15, no. 12, pp. 8342–8346, 2015.

[121] A. Melikyan, L. Alloatti, A. Muslija, *et al.*, "High-speed plasmonic phase modulators," *Nature Photon*, vol. 8, no. 3, pp. 229–233, 2014.

[122] A. Messner, P. A. Jud, J. Winiger, *et al.*, "Broadband metallic fiber-to-chip couplers and a low-complexity integrated plasmonic platform," *Nano Lett.*, vol. 21, no. 11, pp. 4539–4545, 2021.

[123] S. Li, G. Zuo, N. Wu, *et al.*, "Hybrid plasmonic nanofocusing waveguide for on-chip sers tweezer," *Optics & Laser Technology*, vol. 143, p. 107 259, 2021.

[124] W.-Y. Tsai, J.-S. Huang, and C.-B. Huang, "Selective trapping or rotation of isotropic dielectric microparticles by optical near field in a plasmonic archimedes spiral," *Nano Lett.*, vol. 14, no. 2, pp. 547–552, 2014.

[125] H. Choo, M.-K. Kim, M. Staffaroni, *et al.*, "Nanofocusing in a metal–insulator–metal gap plasmon waveguide with a three-dimensional linear taper," *Nature Photon*, vol. 6, no. 12, pp. 838–844, 2012.

[126] M. Heydari, A. Habibzadeh-Sharif, and F. Jabbarzadeh, "Design of a compact refractive-index sensor based on surface plasmon polariton slot waveguide," *Photonics and Nanostructures - Fundamentals and Applications*, vol. 38, p. 100 755, 2020.

[127] P. Neutens, P. Van Dorpe, I. De Vlaminck, L. Lagae, and G. Borghs, "Electrical detection of confined gap plasmons in metal–insulator–metal waveguides," *Nature Photon*, vol. 3, no. 5, pp. 283–286, 2009.

[128] S. Zhu, G. Lo, and D. Kwong, "Theoretical investigation of silicide schottky barrier detector integrated in horizontal metal-insulator-silicon-insulator-metal nanoplasmonic slot waveguide," *Opt. Express*, vol. 19, no. 17, pp. 15 843–15 854, 2011.

[129] M Blauth, J Harms, M Prechtl, J. Finley, and M Kaniber, "Enhanced optical activity of atomically thin $MoSe_2$ proximal to nanoscale plasmonic slot-waveguides," *2D Mat.*, vol. 4, no. 2, p. 021 011, 2017.

[130] J. Dionne, L. Sweatlock, H. Atwater, and A. Polman, "Plasmon slot waveguides: Towards chip-scale propagation with subwavelength-scale localization," *Phys. Rev. B*, vol. 73, no. 3, p. 035 407, 2006.

[131] J Bravo-Abad, F. García-Vidal, and L Martín-Moreno, "Resonant transmission of light through finite chains of subwavelength holes in a metallic film," *Phys. Rev. Lett.*, vol. 93, no. 22, p. 227 401, 2004.

[132] H. Shin, M. F. Yanik, S. Fan, R. Zia, and M. L. Brongersma, "Omnidirectional resonance in a metal–dielectric–metal geometry," *Appl. Phys. Lett.*, vol. 84, no. 22, pp. 4421–4423, 2004.

[133] R. Zia, A. Chandran, and M. L. Brongersma, "Dielectric waveguide model for guided surface polaritons," *Opt. Lett.*, vol. 30, no. 12, pp. 1473–1475, 2005.

[134] F. Garcia-Vidal, E. Moreno, J. Porto, and L Martin-Moreno, "Transmission of light through a single rectangular hole," *Phys. Rev. Lett.*, vol. 95, no. 10, p. 103 901, 2005.

[135] F. G. De Abajo, R Gómez-Medina, and J. Sáenz, "Full transmission through perfect-conductor subwavelength hole arrays," *Phys. Rev. E*, vol. 72, no. 1, p. 016 608, 2005.

[136] F. García-Vidal, L. Martín-Moreno, E. Moreno, L. Kumar, and R Gordon, "Transmission of light through a single rectangular hole in a real metal," *Phys. Rev. B*, vol. 74, no. 15, p. 153 411, 2006.

[137] F Eftekhari and R Gordon, "Geometric optics method for surface plasmon integrated circuits," *Opt. Express*, vol. 15, no. 18, pp. 11 595–11 600, 2007.

[138] A Mary, S. G. Rodrigo, L Martin-Moreno, and F. Garcia-Vidal, "Theory of light transmission through an array of rectangular holes," *Phys. Rev. B*, vol. 76, no. 19, p. 195 414, 2007.

[139] J. Christensen, L. Martin-Moreno, and F. J. Garcia-Vidal, "Theory of resonant acoustic transmission through subwavelength apertures," *Phys. Rev. Lett.*, vol. 101, no. 1, p. 014 301, 2008.

[140] E. S. Barnard, J. S. White, A. Chandran, and M. L. Brongersma, "Spectral properties of plasmonic resonator antennas," *Opt. Express*, vol. 16, no. 21, pp. 16 529–16 537, 2008.

[141] R. Gordon, "Reflection of cylindrical surface waves," *Opt. Express*, vol. 17, no. 21, pp. 18 621–18 629, 2009.

[142] L. Verslegers, Z. Yu, P. B. Catrysse, and S. Fan, "Temporal coupled-mode theory for resonant apertures," *J. Opt. Soc. Am. B*, vol. 27, no. 10, pp. 1947–1956, 2010.

[143] P. E. Landreman, H. Chalabi, J. Park, and M. L. Brongersma, "Fabry-perot description for mie resonances of rectangular dielectric nanowire optical resonators," *Opt. Express*, vol. 24, no. 26, pp. 29 760–29 772, 2016.

[144] S. I. Bozhevolnyi, "Effective-index modeling of channel plasmon polaritons," *Opt. Express*, vol. 14, no. 20, pp. 9467–9476, 2006.

[145] J. S. Smalley, F. Vallini, Q. Gu, and Y. Fainman, "Amplification and lasing of plasmonic modes," *Proceedings of the IEEE*, vol. 104, no. 12, pp. 2323–2337, 2016.

[146] P. Saeidi, B. Jakoby, G. Pühringer, *et al.*, "Design, analysis, and optimization of a plasmonic slot waveguide for mid-infrared gas sensing," *Nanomaterials*, vol. 12, no. 10, p. 1732, 2022.

[147] G. Ma, R. Liang, Z. Wan, and S. Wang, "Critical angle reflection imaging for quantification of molecular interactions on glass surface," *Nat Commun*, vol. 12, no. 1, pp. 1–9, 2021.

Appendices

Appendix A

MATLAB code Subwavelength Slit Calculations

A.1 Propagation Constant in MIM Structure

```
close all; clear all
%% %Determination of propgation constant
a = [1*10^(-9):1*10^(-9):20*10^(-9)]; %Widths of the slit
filename = "Johnshon_and_Christy.xlsx"; %Johnson and Christy paper
data = xlsread(filename);
lambda = data(:,1);  %Wavelengths
epsilon_m = data(:,2) + 1i*data(:,3); %Permittivity values
epsilon_d = 1; %Permittivity of surrounding medium
k_0 = 2*pi./lambda;
%%
syms beta;
for i = 1:1:length(lambda)
      for j = 1:1:length(a)
                  kappa_m = sqrt(beta^2 - epsilon_m(i)*k_0(i)^2);
                  kappa_d = sqrt(beta^2 - epsilon_d*k_0(i)^2);
```

```
16                  f(i,j) = tanh(kappa_m*a(j)/2) + ...
                        ((epsilon_m(i)*kappa_d)/(epsilon_d*kappa_m));
17                  k_z(i,j) = eval(vpasolve(f(i,j),beta));
18      end
19  end
20  k_z = double(k_z);
21  %% %Saving the propagation constant data
22  filename = 'real_prop.xlsx';
23  writematrix(real(k_z),filename,'Sheet',1);
24  filename = 'imag_prop.xlsx';
25  writematrix(imag(k_z),filename,'Sheet',1);
```

A.2 Optical Cross-Sections, Field Enhancement, and Power

```
1  %%
2  close all; clear all;
3  %%
4  %For reflection coefficient in a slit completely surrounded by air
5  filename = 'real_prop.xlsx'; %Real part of the pre-determined ...
       propagation constant in the MIM structure
6  data1 = xlsread(filename);
7  filename = 'imag_prop.xlsx';%Imaginary part of the pre-determined ...
       propagation constant in the MIM structure
8  data2 = xlsread(filename);
9  lambda = data1(:,1);
10 k_z = data1(:,2:end) + 1i*data2(:,2:end);
11 l = 100*10^(-9); %Length of the slit
```

```
a = 1*10^(-9):1*10^(-9):20*10^(-9); %Widths of the slit
k_0 = 2*pi./lambda;
n_eff = k_z./k_0;
%%
for j = 1:1:20
    lambda_mod = lambda./n_eff;
    I = (a(j).*pi./lambda_mod) + ...
        ((1i*2*a(j).*(log(2*pi*a(j)./lambda_mod) - 1.5))./lambda_mod);
    r = (1 - I)./(1 + I); %Reflection Coefficient
    t = (2)./(1+I);%Transmission Coefficient
    phi = angle(r);%Reflection Phase
%%
    phi_l = 2*imag(k_z)*l;
    ∆ = 2*real(k_z)*l + 2*phi;
    term1 = (1 - (abs(r)).^2).*(abs(t)).^2.*exp(-phi_l);
    term2 = (1 + (abs(r)).^4.*exp(-2*phi_l) - ...
        2*(abs(r)).^2.*exp(-phi_l).*cos(∆));
    T = term1./term2; %Total transmission
    term3 = (1 - exp(-phi_l));
    term4 = 1 + abs(r).^2.*exp(-phi_l);
    term5 = (abs(t).^2 .*(1 + abs(r).^2.*exp(-phi_l) - ...
        2.*abs(r).*cos(∆/2).*exp(-phi_l/2)));
    term6 = 1 + exp(-phi_l) - 2.*cos(real(k_z)*l).*exp(-phi_l/2);
    term7 = abs(t).^2.*(1 + abs(r).^2 + 2.*abs(r).*cos(phi));
        sigma_t = T.*a(j); %transmission cross-section
        sigma_a = sigma_t.*term3.*term4./term2; %absorption ...
            cross-section
        eta = term5.*term6./term2; %Field
        power = abs(eta.^2)*a(j); %Power in the slit
    %% %Plotting the optical cross-sections
    figure(1)
    plot(lambda*10^(9),2*sigma_t*10^6,'LineWidth',2.5,'color','#f51c1c')
```

```
40      xlabel('Wavelength (in ...
            nm)','FontSize',18,'FontName','Bahnscrift')
41      ylabel('\sigma_s and \sigma_a (in ...
            \mum)','FontSize',18,'FontName','Bahnscrift')
42      set(gca, 'XTick', 600:200:1600,'YTick', ...
            0:0.02:0.20,'FontSize',18,'LineWidth',2.5)
43      grid on
44      xlim([wl*10^(9) 1650]);
45      ylim([0 0.1])
46      hold on
47      plot(lambda*10^(9),sigma_a*10^(6),'LineWidth',2,'color','#4bd8da')
48  end
```

Appendix B

Maximum Power Transfer in Slits

B.1 Maximum Power Transfer for a Slit of Length 100 nm

FDTD Simulation Results

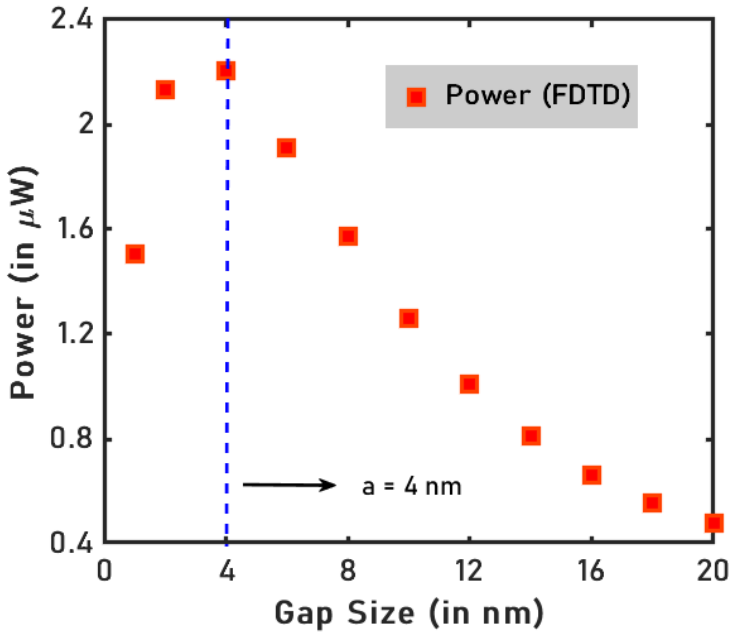

FIGURE B.1: Average power (red squares) inside the slit of length 100 nm and widths varying between 1 nm and 20 nm, obtained from numerical FDTD simulations. Power maximizes at a = 4 nm indicated by the vertical line. [28].

B.2 Maximum Power Transfer for a Slit of Length 80 nm

Theoretical Analysis Results

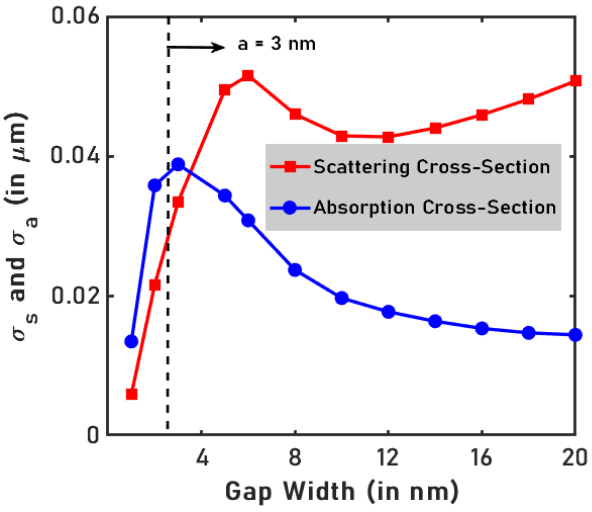

(A)

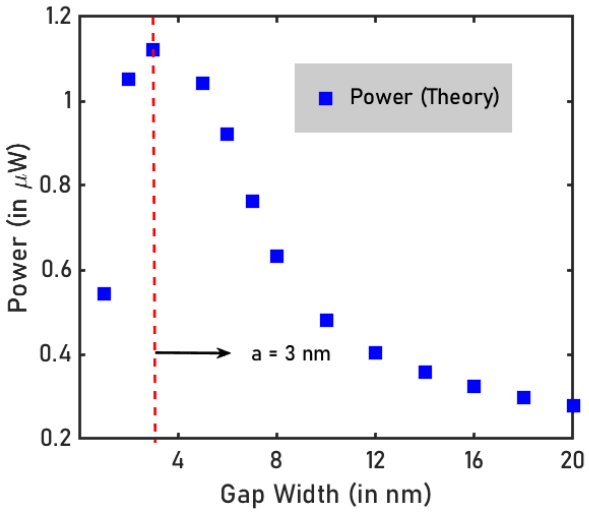

(B)

FIGURE B.2: A) The peak values of σ_s (red squares) and σ_a (blue circles) at the resonance condition of a 80 nm long slit of varying widths. σ_s and σ_a are equal at a gap of around 3 nm. The vertical dashed line indicates the 3 nm mark. B) Power (blue squares) inside a metallic slit computed analytically using the Fabry-Pérot formalism. Power saturates at 3 nm for equal values of σ_s and σ_a at resonance, marked by the vertical dashed line [28].

B.3 Maximum Power Transfer for a Slit of Length 120 nm

Theoretical Analysis Results

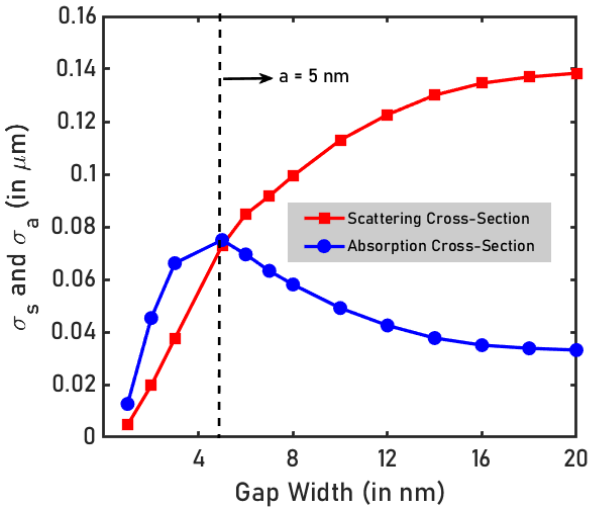

(A)

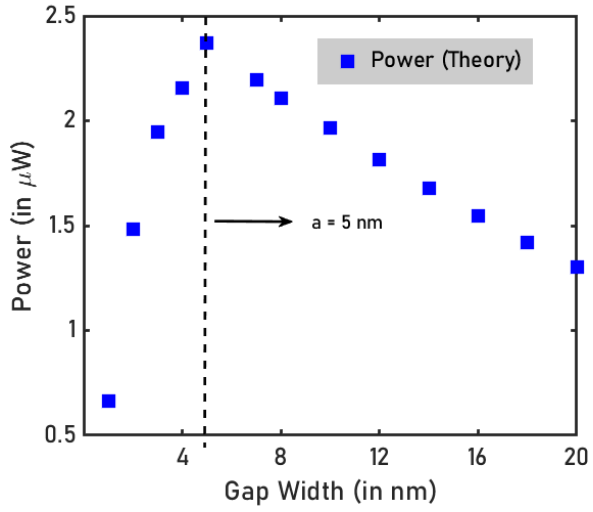

(B)

FIGURE B.3: A) The peak values of σ_s (red squares) and σ_a (blue circles) at the resonance condition of a 80 nm long slit of varying widths. σ_s and σ_a are equal at a gap of around 3 nm. The vertical dashed line indicates the 3 nm mark. B) Power (blue squares) inside a metallic slit computed analytically using the Fabry-Pérot formalism. Power saturates at 3 nm for equal values of σ_s and σ_a at resonance, marked by the vertical dashed line [28].

Appendix C

MATLAB code for reflection in plasmonic slot waveguide

C.1 Reflection Coefficient in Plasmonic Slot Waveguide

```
close all; clear all
%%
w = [30*10^(-9):30*10^(-9):210*10^(-9)];
epsilon_m = -115.13 + 1i*11.259;
syms beta;
lambda = 1550*10^(-9);
epsilon_d = 1.44^2;
epsilon_d2 = 1.44^2;
epsilon_d3 = 1.44^2;
k_0 = 2*pi/lambda;
a = w./lambda;
theta = 0*pi:0.01*pi:pi/2;
l = 200*10^(-9);
%%
%dSolving for the propagation constant
 for j = 1:1:length(a)
```

```
17              kappa_m = sqrt(beta^2 - epsilon_m*k_0^2);
18              kappa_d = sqrt(beta^2 - epsilon_d*k_0^2);
19              f(j) = tanh(kappa_d*w(j)/2) + ...
                    ((epsilon_d*kappa_m)/(epsilon_m*kappa_d));
20              k_z(j) = eval(vpasolve(f(j),beta, 1.5*k_0));
21              n_eff(j) = k_z(j)/k_0;
22   end
23   epsilon_d1 = n_eff.^2;
24
25   %%
26  syms u;
27   for i = 1:1:length(1)
28       for j = 1:1:length(theta)
29          f(i) = sqrt(1 - ...
                (epsilon_d1(i)/epsilon_d2)*(sin(theta(j)))^2 - ...
                (u^2/epsilon_d2));
30          g(i) = (1 - (u^2/epsilon_d2));
31          h(i) = (sin(pi*u*a(i)))^2/(pi^2*u^2*a(i));
32          func(i) = f(i)*h(i)/g(i);
33          I(i,j) = ...
                2*vpaintegral(func(i),u,0,Inf,'MaxFunctionCalls',Inf);
34          r(i,j) = (sqrt(epsilon_d1(i)/epsilon_d2)*cos(theta(j)) - ...
                I(i,j))/(sqrt(epsilon_d1(i)/epsilon_d2)*cos(theta(j)) ...
                + I(i,j));
35       end
36   end
37  %%
```